Modification of Surfaces with Carboxymethylthio and Piperazinyl Chelating Ligands for Heavy Metal Trapping Applications

Dissertation

zur Erlangung des akademischen Grades

doctor rerum naturalium

(Dr. rer. nat.)
im Fach Chemie
eingereicht an der
Mathematisch-Naturwissenschaftlichen Fakultät
der Humboldt-Universität zu Berlin
von

John Onyango Adongo, MSc.

Präsidentin der Humboldt-Universität zu Berlin
Prof. Dr.-Ing. Dr. Sabine Kunst

Dekan der Mathematisch-Naturwissenschaftlichen Fakultät
Prof. Dr. Elmar Kulke

Gutachter: 1. Prof. Dr. Klaus Rademann
2. PD Dr. Karsten Hinrichs
3. Prof. Dr. Nicola Pinna

Tag der mündlichen Prüfung: 13th December 2018.

ABSTRACT

The two heavy-metal-ion (HMI) chelating groups, carboxymethylthio- (CMT), and piperazinyl- (PPz), were successfully electrografted on Si(111)-H and Au substrate surfaces via the direct cathodic electroreduction of their aryl diazonium salt derivatives: the 4-(carboxymethylthio)benzenediazonium salt $[4\text{-CMTBD}]^+BF_4^-$, and the 4-(piperazinyl)benzenediazonium salt $[4\text{-PPzBD}]^+BF_4^-$. The electrografting was performed using cyclic voltammetric (CV) and chronoamperometric (CA) techniques. The loss of the diazonium group $[N\Xi N\text{-}]^+$ upon the cathodic electroreduction of both the $[4\text{-CMTBD}]^+$ and $[4\text{-PPzBD}]^+$ was investigated by Infrared Spectroscopic Ellipsometry (IRSE). The IRSE spectra confirmed the successful surface functionalization by the CMT and PPz chelating groups by their characteristic absorption bands on the electrografted Si(111) and Au substrates. Furthermore, after the surface electrografting reaction, the phenyl (Ph) group absorption bands shifted to higher wavenumbers by $\sim$ 30 cm^{-1} (in the case of the reduction of 4-CMTBD) and $\sim$ 20 cm^{-1} (in the case of 4-PPzBD reduction). This characterized, in part, the attachment of the Ph- substrate-linker groups on both the Si(111) and Au surfaces.

The analysis of the chronoamperometric electroreduction of the two diazonium cations $[4\text{-CMTBD}]^+$ and $[4\text{-PPzBD}]^+$, on both Si(111)-H and Au surfaces, revealed that the rate of decay in currents correlates with the second-order kinetic rate law during the early stages of the electrografting reactions. The analysis of the frequency changes via the electrochemical quartz crystal microbalance (EQCM) electrodeposition experiments on Au surface revealed faradaic efficiencies of about 0.19 and 0.17 upon the electroreduction of 4-CMTBD and 4-PPzBD respectively.

The treatment of the functionalized surfaces, Si-(4-CMTB) with the Cu and Pb ions, and Si-(4-PPzB) with Cu ions under low pressure hydrothermal conditions led to the formation of organometallic chelate complexes on the surfaces. The subsequent Raman-backscattering spectroscopic investigations revealed the characteristic vibrational bands related to Cu-S, Cu-O, Pb-S and Pb-O bonds as evidence of Cu and Pb chelation on the Si-(4-CMTB) surface. The Cu-N related Raman bands on the Cu ion treated Si-(4-PPzB) surface also confirmed the binding of Cu. In addition, the chelation of Cu on the Si-(4-CMTB) surface was characterized by a red shift of about 10 cm^{-1} within the C-O region, while the binding of Cu on the Si-(4-PPzB) surface gave a red shift of $\sim$ 50 cm^{-1} within the C-N region. However, the binding of Pb as detected by the Pb-S and Pb-O Raman signals on the Si-(4-CMTB) surface showed no appreciable bathochromic shift in the C-O region. The X-ray photoelectron spectroscopy (XPS) Si2p signal attenuation experiments ascertained the formation of the electrografted nanoscale organic thin overlayers with thicknesses of about 3.0 nm and 1.9 nm for the Si-(4-CMTB) and Si-(4-PPzB) surfaces, respectively. The uptake of Cu ions on both the Si-(4-CMTB) and Si-(4-PPzB) surfaces was also elucidated by XPS measurements. In addition, the binding of Cu by the PPz ligands on the Si-(4-PPzB) surface was characterized by a broadening of the N1s XPS signal.

The HMI chelating nanocomposite surfaces successfully fabricated and characterized in this work constitute novel functional materials that may be of potential engineering interests.

Keywords: Aryl diazonium cations; Electroreduction; Heavy metal chelating ligands; Organometallic complexes; Silicon surface; Infrared, X-ray, Raman spectroscopy.

ZUSAMMENFASSUNG

Die zwei Chelatbildner für Schwermetallionen, Carboxymethylthio- (CMT) und Piperazinyl- (PPz), wurden erfolgreich über die direkte kathodische Elektroreduktion ihres Aryl diazoniumsalzes auf Wasserstoff–terminiertes Silizium (Si-H)- und auf Gold (Au)-Substratoberflächen aus den Derivaten: 4-(Carboxymethylthio)benzenediazoniumsalz $[4\text{-CMTBD}]^+BF_4^-$ und 4-(Piperazinyl)benzenediazoniumsalz $[4\text{-PPzBD}]^+BF_4^-$ abgeschieden. Die elektrochemische Anbindung wurde unter Verwendung von zyklischer Voltammetrie (CV) und chronoamperometrie (CA) Techniken durchgeführt. Der Verlust der Diazoniumgruppe $[N\Xi N-]^+$ nach kathodischer Elektroreduktion von $[4\text{-CMTBD}]^+$ und $[4\text{-PPzBD}]^+$ wurde mittels Infrarotspektroskopie-Ellipsometrie (IRSE) untersucht. Die IRSE-Spektren bestätigten die Anwesenheit der organischen CMT- und PPz-Komplexbildnergruppen durch ihre charakteristischen Absorptionsbanden auf den elektrotransplantierten Si(111) - und Au-Substraten, was eine erfolgreiche Oberflächenfunktionalisierung anzeigt. Darüber hinaus verschoben sich die mit der Phenyl (Ph) -Gruppe verwandten Absorptionsbanden zu höheren Wellenzahlen um ~ 30 cm^{-1} (im Fall der 4-CMTBD-Reduktion) und ~ 20 cm^{-1} (im Fall der 4-PPzBD-Reduktion) nach der Oberfläche Elektropfropfreaktionen. Dies charakterisiert zum Teil die Anheftung der Ph-Substrat-Linker-Gruppen sowohl an die Si (111) - als auch an die Au-Oberfläche.

Die Analyse, der bei der chronoamperometrischen Elektroreduktion gemessenen Ströme, der beiden Diazoniumkationen $[4\text{-CMTBD}]^+$ und $[4\text{-PPzBD}]^+$ sowohl auf Si (111)-H- als auch auf Au-Oberfläche, zeigt eine Korrelation mit der kinetischen Reaktionsgleichung zweiter Ordnung während der frühen Stufen der jeweiligen elektrochemischen Deposition. Die Messungen der Frequenzänderung bei der elektrochemischen Deposition mittels elektrochemischer Quarzkristall-Mikrobalance (EQCM) ergab für die Au-Oberfläche eine Faraday-Effizienz von etwa 0.19 bzw. 0.17 für die Elektroreduktion von 4-CMTBD bzw. 4-PPzBD.

Die Behandlung der funktionalisierten Oberflächen, Si(4-CMTB) mit Cu- und Pb-Ionen, und Si(4-PPzB) mit Cu-Ionen unter niedrigen hydrothermalen Druckbedingungen führte zur Bildung von organometallischen Chelatkomplexen auf den Oberflächen. Die anschließenden Raman-spektroskopischen Untersuchungen zeigten die charakteristischen Schwingungsbanden in Bezug auf Cu-S, Cu-O, Pb-S und Pb-O-Bindungen als Beweis für Cu- und Pb-Chelatbildung auf der Si(4-CMTB)-Oberfläche. Die Cu-N-verwandten Raman-Banden auf der Cu-Ionen-behandelten Si(4-PPzB)-Oberfläche bestätigten somit auch die Bindung von Cu-Ionen an diese funktionale Schicht. Darüber hinaus war die Chelatisierung von Cu auf der Si-(4-CMTB)-Oberfläche durch eine Rotverschiebung der C-O Schwingung von etwa 10 cm^{-1} gekennzeichnet, während die Bindung von Cu auf der Si(4-PPzB)-Oberfläche eine bathochrome Verschiebung von ~ 50 cm^{-1} für die C-N Schwingung zeigte. Die Bindung von Pb, die durch die Pb-S- und Pb-O Raman-Signale auf der Si(4-CMTB)-Oberfläche festgestellt wurde, zeigte jedoch keine nennenswerte Verschiebung der C-O Schwingung. Mittels der X-ray Photoelektronenspektroskopie (XPS) konnte die Schichtdicke der (4-CMTB) bzw. (4-PPzB) modifizierten Si-Oberfläche zu etwa 3 nm bzw. ~ 1,9 nm bestimmt werden. Die Aufnahme von Cu-Ionen sowohl auf der Si(4-CMTB)- als auch auf der Si(4-PPzB)-Oberfläche wurde ebenfalls mittels XPS untersucht. Diese Messungen zeigten die Bindung von Cu durch die PPz-Liganden an die Si(4-PPzB)-Oberfläche durch eine Verbreiterung des N1s XPS Signal.

Die Schwermetallionen-chelatisierenden Nanokompositoberflächen, die in dieser Arbeit erfolgreich hergestellt und charakterisiert wurden, stellen neuartige funktionelle Materialien dar, die potentiell technische Interesse haben könnten.

Keywords: Aryl Diazoniumkationen; Elektroreduktion; Chelatbildner für Schwermetallionen; Organometallischen Chelatkomplexen; Silizium-Oberfläche; Infrarot, X-Ray, Raman spektroskopie.

TABLE OF CONTENTS

1.0 INTRODUCTION

1.1 The Chelate Effect and its Applications

The formation of metal complexes via chelating ligands often proceeds at extraordinarily higher rates as opposed to the formation of the corresponding complexes containing non-chelating ligands.[1,2] This phenomenon can be illustrated by comparing the formation/stability constant K_β of a complex containing a bidentate ligand such as ethylenediamine (*en*) with the corresponding stability constant, K_α, of the tetraamine complex under similar conditions. It is found empirically that the value of, K_β, is always greater than that of, K_α (Figure 1).[3]

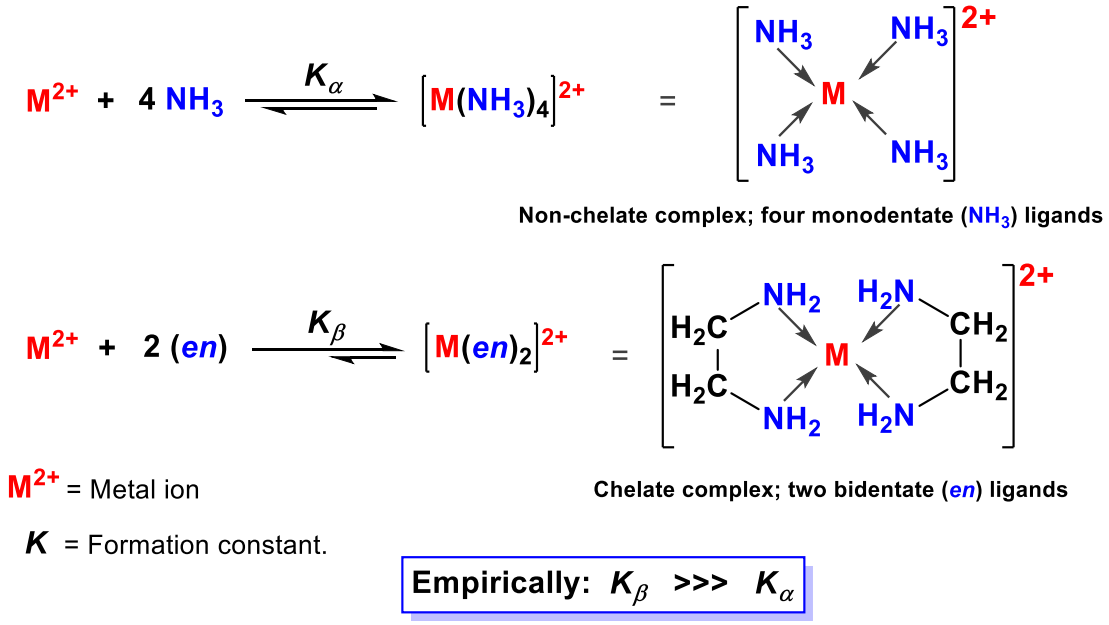

Figure 1: Schematic representation of the chelate effect.[3]

Although the basicities of the NH_3 and ethylenediamine (*en*), $H_2NCH_2CH_2NH_2$, are similar, the *en* forms much more stable complexes. This means that the chelate formed in the reaction K_β is more stable than the complex that is formed in the reaction. For both ligands, the atoms donating the electron pairs are the nitrogen atoms. The bidentate *en* ligand forms “chelate rings” with increased stability constant

compared to the NH_3 complexes. This enhanced stability towards chelate complex formation is referred to as the chelate effect.[3] In the many cases, under similar conditions, complexes that contain chelate rings within their coordination spheres are always present in higher concentrations compared to their analogue counterparts with monodentate (non-chelating) ligands. This implies that the chelate complex formation is generally the more favoured reaction.[4]

Chelating ligands are often exploited as agents in metal binding applications. A case in point that exemplifies the importance of chelation in biological systems is the classic role played by the siderophore group of compounds (polydentate chelating agents naturally synthesized by bacteria and fungi), whose primary function entails heavy metal ion (HMI) scavenging.[5]

The chelate effect can be rationalized based on the thermodynamic point of view, since chelation reactions are driven by the entropy factor. This arises due to the increase in total number of independent molecules in solution upon chelation. From the laws of chemical thermodynamics, the relation between free energy, enthalpy, entropy changes, and equilibrium constants can be expressed by equations 1, 2 and 3 at standard states.

$$\Delta G^o = \Delta H^o - T\Delta S^o \qquad \text{---------- (Eq. 1)}$$

$$\Delta G^o = -RT\ln K \qquad \text{---------- (Eq. 2)}$$

Where ΔG^o = Gibbs free energy, ΔH^o = enthalpy change, T = Kelvin temperature, ΔS^o = entropy change, R = universal gas constant, and K = equilibrium constant.

The enthalpy *H,* is a function of bonds strengths involved in the complexation reaction and can be determined from the Van't Hoff's equation:

$$\frac{d\ ln\ K_{eq}}{dT} = \frac{\Delta H^o}{RT^2} \qquad \text{---------- (Eq. 3)}$$

The entropy, S^o, is related to the degree of disorder in a given system and the reactions characterized by increase in entropy are generally highly favoured. In addition, the larger the value of equilibrium constant K_{eq}, the more negative ΔG^o becomes and hence the reaction processed more spontaneously. In reference to Figure 1, the (*en)* chelating ligand tend to form chelate rings with extra stability compared to that of ammonia (NH_3).[3] Although four equivalent metal – ligand (M-L) bonds are formed in both cases which makes their enthalpy changes ΔH^o comparable, the formation of the chelate complex is distinctly the more highly favoured reaction since the increase in ΔS for the chelate-complex formation is higher compared to the case of non-chelate complex formation.

The mechanism of chelate-complex formation is also favoured kinetically. Once a donor atom of a multidentate chelating ligand is anchored to a metal ion, the probability that the other tethered ligand donor atom of the same chelating group binding to the same metal is greatly enhanced based on the enhanced proximity (Figure 2 (a)).[4]

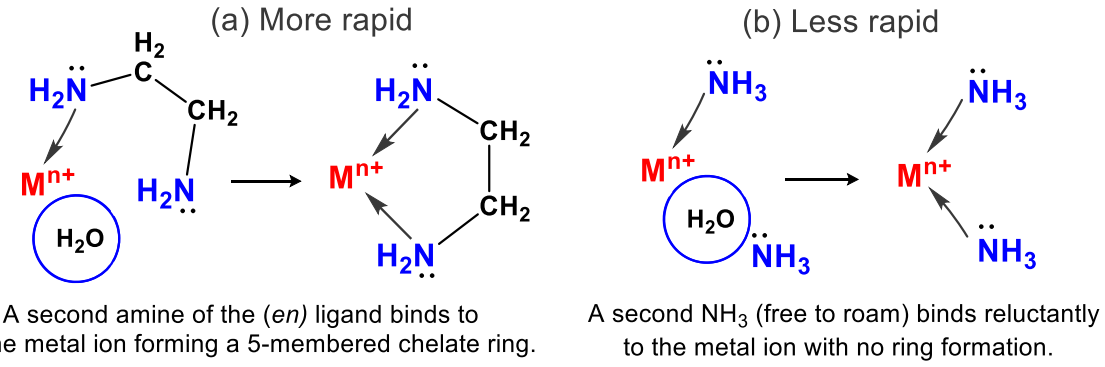

Figure 2: Schematic representation of the kinetics of chelation mechanism. (Adapted from ref.[4])

As opposed to the second case (Figure 2 case (b)), in which the monodentate NH_3 groups can roam more freely, the probability of rate of the first reaction (Figure 2 case (a)) occurring at much faster rate in higher due to the close proximity of the second nitrogen donor atom to the metal. This happens because the "local concentration" of the second ligand donor atom on the chelate in the vicinity of the metal ion becomes greater after the binding of the first donor atom to the metal. This kinetic behaviour explains why the reactions between (bi/multi-)dentate ligands and the metal cations generally have a higher equilibrium constant values compared to the corresponding non-chelating cases.[6]

In recent years, a variety of materials that incorporate organic chelating agents or ligands have been fabricated towards creating a variety of novel applications for the rapid extraction of a variety of HMI's including the remediation and or recovery of radioactive metal wastes.[7,8,9,10,11] Functionalized hybrid-polymeric structures bearing multiple chelating groups for HMI uptake have also been designed and fabricated for the removal or separation of chromium from water, mercury vapor from flue gases and cerium from feed solutions.[12,13,14] The unique conformation of chelating groups as a pre-organized HMI precursor has also actuated developments in HMI assay chips as well as affinity sensing technologies, whereby the chelating group serves the role of a recognition element.[15,16] Metal chelators have also been coupled to nanomagnets in attempts to develop potential methods for rapid removal of selected toxic heavy metals from contaminated water.[17] The mechanism of enhancement of HMI adsorption and/or rapid binding via the formation of chelate complexes on modified surfaces is largely based on chemical equilibrium concepts as well as bonding theories in organometallic chemistry.

1.2 Heavy Metal Contamination: Toxicity of Copper and Lead

The rapid global industrialization leading to exponential rise in fossil-fuel/coal/petroleum emissions, the extensive mining (metal refining and smelting), large-scale prolonged usage of HMI enriched agrochemicals (fungicides, pesticides, herbicides) as well as the excessive dumping of electronic-waste are some of the major factors that have led to widespread accumulation of toxic HMI pollutants in many parts of the world. This poses a threat to marine organisms and freshwater environments.[18,19] Statistics indicate that HMI's constitute the largest share of contaminants affecting soil and ground water in Europe (Figure 3).[20] Heavy metal contamination remains a significant global public health concern that has been labelled as "blind evil" that portends environmental disasters.[19,21,22]

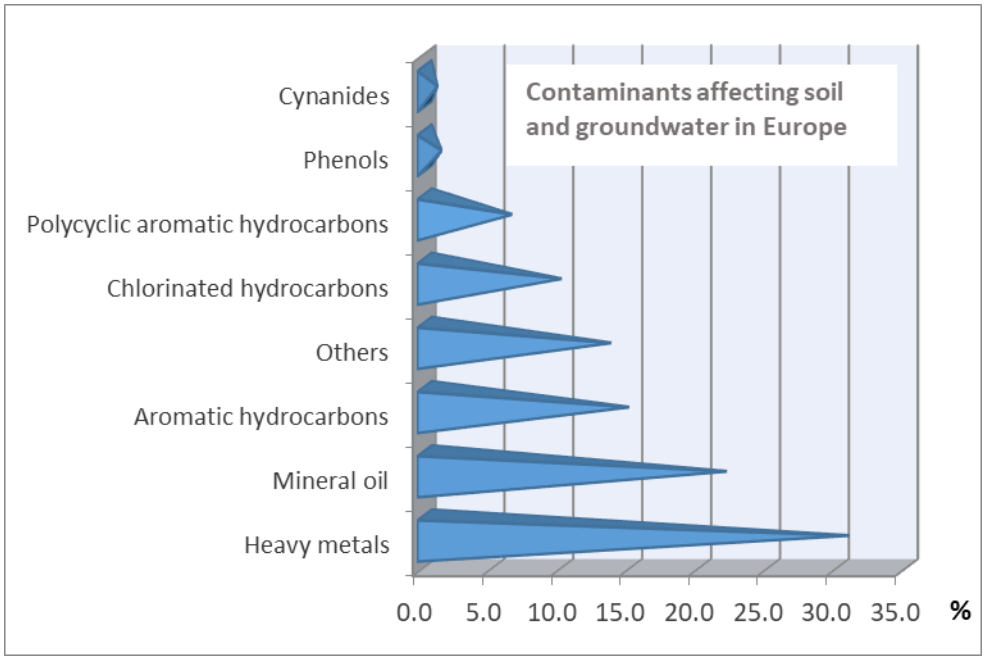

Figure 3: Summary of contaminants affecting soil and groundwater in Europe. (Adapted from ref. [20])

Some HMI - contaminants can potentially be lethal upon bio-accumulation. They are known to penetrate into the human body via inhalation, absorbed by the skin or the

mouth through ingestion or drinking of contaminated water. Once in the body system, the HMI's readily target the binding sites of biomolecules, such as in proteins, leading to disruption of normal biochemical cycles (or enzymatic processes).[18,23]

The most commonly found heavy metals in waste water include arsenic (As), cadmium (Cd), chromium (Cr), copper (Cu), lead (Pb), nickel (Ni), and zinc (Zn), all of which can cause adverse effects to human health and the environment.[24] Studies show that the exponential rise in emissions of HMI's such as Pb and Cu began with in the industrial revolution era, which was characterized by the unprecedented production and use of heavy metals for technological advancements (Figure 4). The cumulative release of HM's in the environment was massive, to an extent of overwhelming the natural biogeochemical cycles in many ecosytems.[22,25]

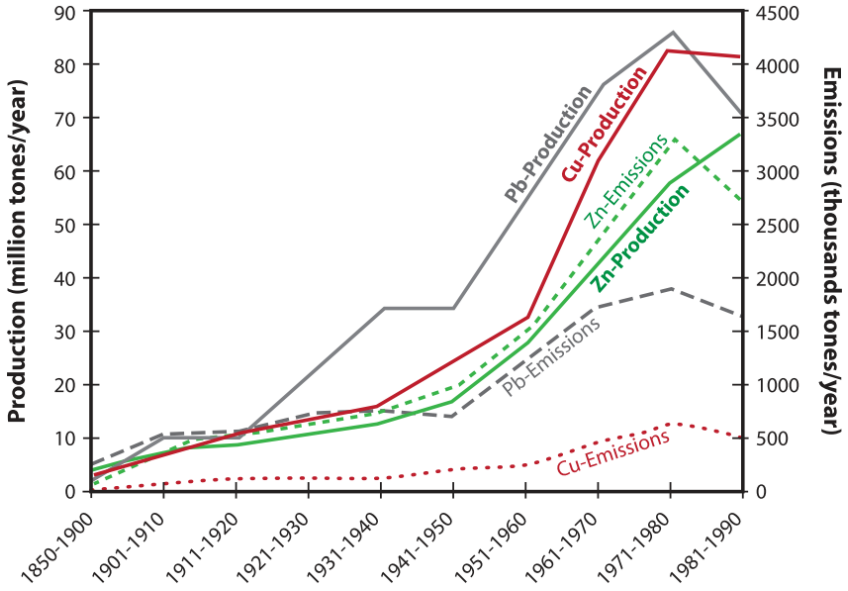

Figure 4: The global production and emission of Pb, Cu and Zn during 1850–1990. (Adapted from ref.[22])

Although, required as a micronutrient in biological systems, excessive levels of Cu in liver, brain, kidney and the cornea often pose adverse health conditions.

Copperiedus is a form of heavy metal poisoning/toxicity condition caused by excess Cu levels in the human blood. This condition can lead to damage of the liver, kidney and brain tissues.[26,27,28] Wilson's disease, which is caused by excess Cu levels in human blood and is characterized by hematemesis (vomiting of blood), hypotension (low blood pressure), melena, coma, jaundice (yellowish pigmentation of the skin), diarrhoea and gastrointestinal distress.[23] Low Cu(II) levels has also been shown to be highly toxic to certain aquatic organisms such as fish, algae and molluscs.[29]

Although lead (Pb) is an industrially important metal, some previous reports have indicated that the Pb-exposure accounted for about 853,000 deaths (in 2013), 494,550 deaths (in 2015) and the loss of 9.3 million disability adjusted life years (DALY) – which refers to the number of years lost due to ill-health.[30] Lead poisoning, commonly known as "plumbism" is a form of toxicity that mainly affects the soft brain tissues. It is characterized by irreversible brain damage, neurological disorders, kidney damage, anemia and toxicity to both the male and female reproductive organs, and miscarriages in pregnant women.[23,31] Other studies have also shown that increase in blood Pb concentrations correlates to impaired learning abilities (Figure 5).[32,33]

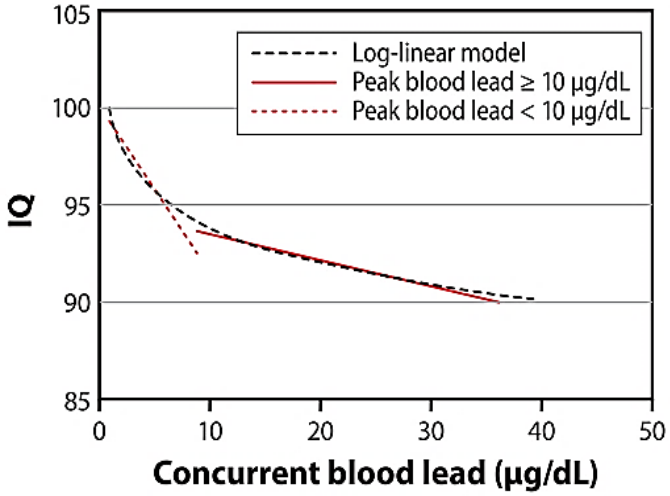

Figure 5: The relationship between blood Pb concentrations and Intelligence Quotient (IQ).[33]

As a result of the high permeability of blood - brain barrier, young children are particularly more vulnerable and susceptible to the neurotoxic effects of Pb exposure [18,19,22,34]. The ionic mechanism of lead toxicity occurs mainly due to the ability of Pb metal ions to replace other divalent cations such as Ca^{2+}, Mg^{2+}, Fe^{2+} and monovalent cations ones like Na^{+} upon coordination, which can lead to disruption of the cell biochemistry and metabolic procesess.[22] This can manifest into changes in biological processes such as cell adhesion, intra- and inter-cellular signalling, protein folding, maturation, apoptosis, ionic transportation, enzyme regulation, and release of neurotransmitters. Some studies have further shown that low levels of divalent Pb can substitute Ca^{2+} and adversely affect the Ca^{2+} - dependent “protein kinase C” enzyme, which is responsible for regulation of signal transduction mechanisms, neural excitation and memory storage.[22]

This justifies the exploration of the chelate modified surfaces towards developing tangible applications that would contribute towards the rapid sensing and trace-level extraction of the HMI’s. The approach investigated in this work is that of introducing the selected chelating agents onto Si and Au surfaces via the electrografting of the aryl diazonium salt derivatives.

1.3 Aryl Diazonium Salts in Surface Modification

The electrografting of aryl diazonium derivatives (R-Ar-N_2^{+}) is a powerful technique for coupling organic groups onto metallic and semiconducting surfaces.[35,36] In recent years, researchers have explored interesting strategies that entail the modification of various substrates including multi-step functionalization approaches involving complex oligomers and peptides as ligands via the diazonium grafting route to create platforms for sensing and/or trace-level trapping of HMI’s.[37,38,39,40] The electrophilic

nature or strong electron-withdrawing effect of the diazonium group ($-N_2^+$) and stability of the nitrogen molecule (N_2) makes them excellent leaving groups during reduction of the salt ($Ar-N_2^+ BF_4^-$). These are unique properties that make them suitable for introducing functional groups (such as organic chelant groups explored in this work) through the direct cathodic electrografting route (Figure 6).[41]

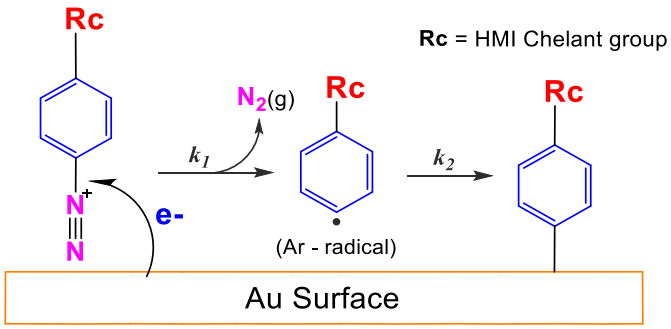

Figure 6: Schematic of the electroreduction of aryl diazonium cation on Au surface. (Mechanism adapted from refs.[35,42])

Figure 7a illustrates how aryl diazonium salts can readily be synthesized via diazotization process in both aqueous solutions and organic solvents from aromatic primary amines.

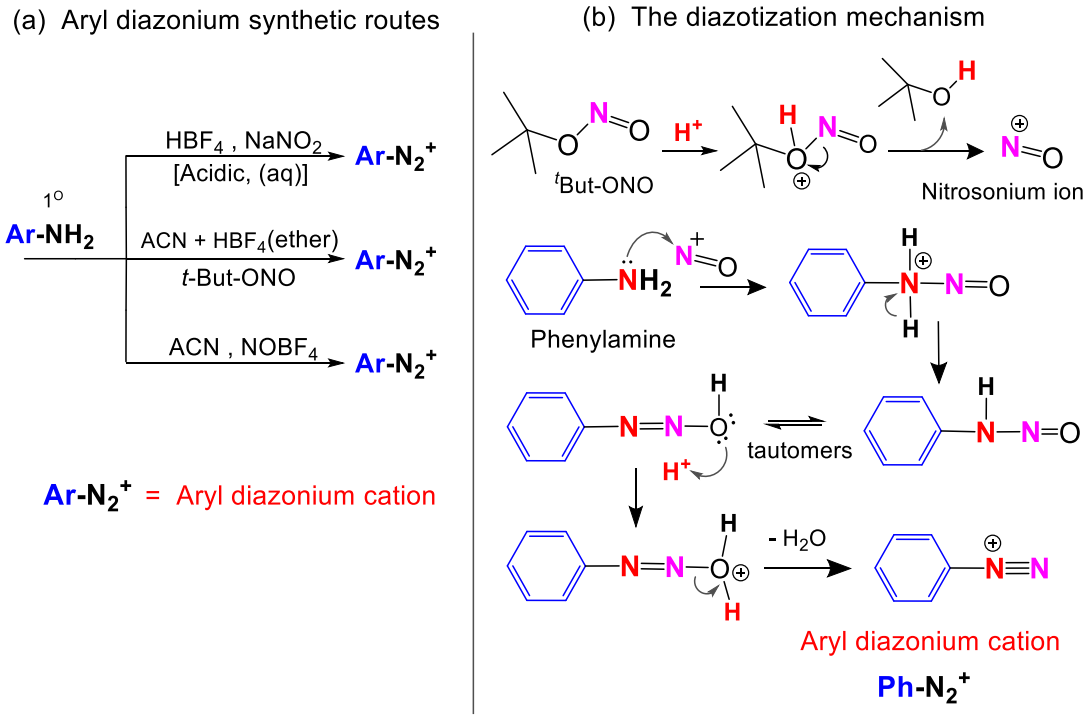

Figure 7: (a) Aryl diazonium synthesis routes and (b) the diazotization mechanism.[43]

Figure 7b shows the diazotization mechanism which involves the nucleophilic attack of the nitrosonium ion generated *in-situ* from the primary aryl amine. The ensuing reactions involve the loss of water molecule and the resulting aryl diazonium salt is stabilized by negatively charged tetrafluoroborate anion BF_4^-.[41,43] A variety of substituent groups can be attached onto the starting aniline compound (Ar-NH_2) prior to the diazotization process, which is a unique feature that lends it suitable for surface modification.

1.4 Modification of Silicon Surface and Potential Applications

Silicon is an abundant and robust semiconducting material whose suitable surface chemistry has fostered organic functionalization/modification efforts towards the fabrication of chip-based bio-electronic devices for biosensing, bio-medical diagnostics and toxic-metal testing.[44,45,46,47,48,49] The exploration of surfaces as molecular reagents towards development of novel applications with selective chemistry has continued to motivate surface modification research towards developing surface sensitive applications that exploit ligand-analyte interactions and semiconductor electronics.[50,51,52,53] There is also a growing demand for more robust, sensitive, efficient, low-cost functional surfaces with good selectivity that are ideal for use as forensic probes or assay kits for the analysis of inorganic toxins.[45,54]

This work explores the design and fabrication of surface modification strategy via aryl diazonium grafting route, which entails the electrochemical modification of hydrogen – terminated silicon surface with chelating groups that can readily bind Cu and/or Pb (Figure 8). The fabrication process and the investigation of the actual HMI uptake and binding are characterized by X-ray photoelectron- and Raman backscattering spectroscopic techniques. The mass deposition of the aryl diazonium

chelate derivatives and their HMI binding capabilities are also investigated using electrochemical quartz crystal microbalance (EQCM) experiments on Au surfaces.

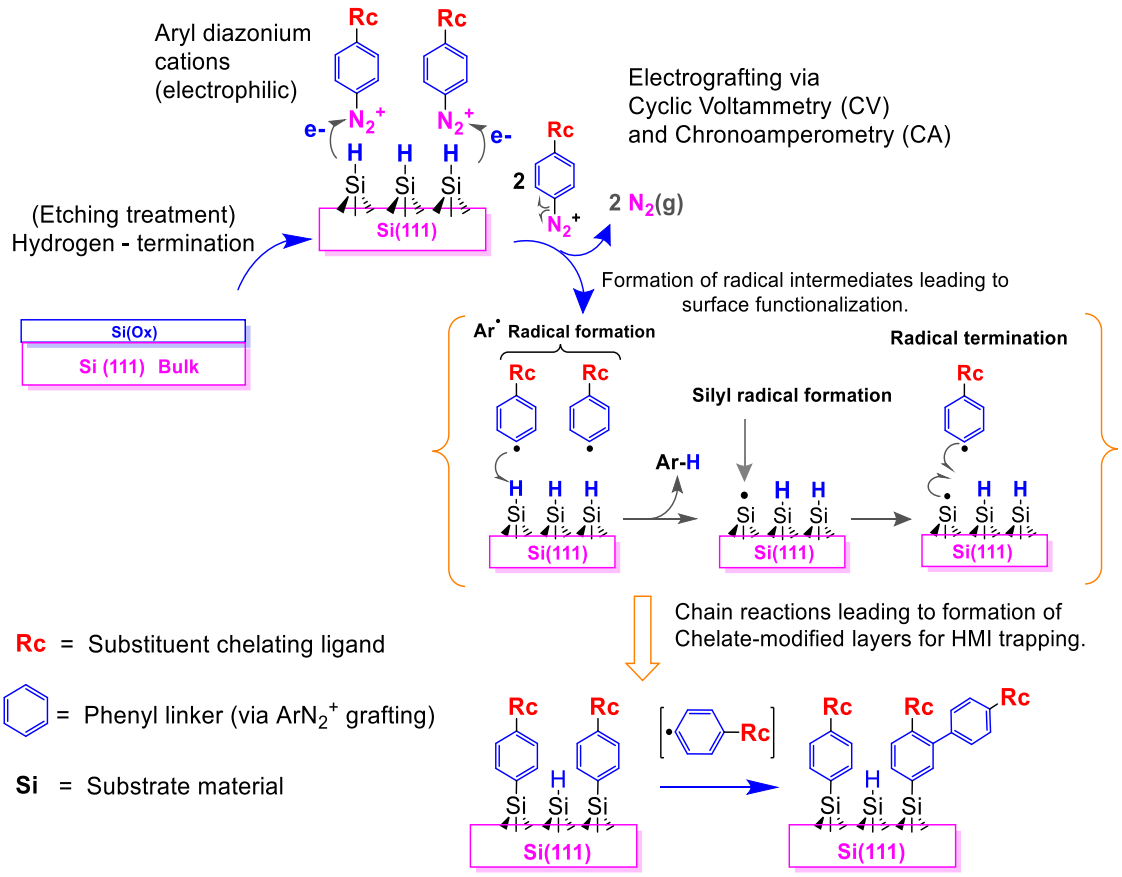

Figure 8: A schematic of aryl diazonium electroreduction and subsequent electrografting of the Ar• radical on the Si(111) surface. (Mechanism adapted from refs. [35,55,56])

The electrografting mechanism of aryl diazonium salts (Ar-N_2^+ BF_4^-) on Si(111)-H surface is known to proceed via aryl radical (Ar•) intermediates generated close to the substrate surface. The Ar• intermediate can then attack a silyl surface radical (Si•) in a termination step to form Si-C covalent bounds producing covalently bound organic layers (Figure 8).[56,57,55] This mechanism is supported by the disappearance of Si-H bonds on the Si(111)-H surface and the absence of diazonium group as a results of its conversion to N_2 gas in the process. The modified surfaces prepared via

this route are very stable against a range of treatments, including sonication and boiling in chloroform, boiling in water, and extended exposure to fluoride and hydroxides.[56,58] The covalent attachment and stability of the resulting substrate – aryl bonding has previously been investigated by X-ray photoelectron spectroscopy (XPS), and infrared (IR) spectroscopy.[35,57,55]

2.0 EXPERIMENTAL METHODS

This section highlights brief theoretical principles and practical aspects of the methods employed in the preparation (via direct electrografting) and the spectroscopic characterization of the chelate functionalized surfaces.

2.1 Pre-treatment of Si(111) Surface (Hydrogen Termination)

The atomically flat hydrogen (H) – terminated Si(111) surface Si(111)-H constitutes one of the most industrially important starting substrate for organic surface modification.[59,60] A wet chemical treatment method was used to realize the atomically flat H - terminated Si(111) surfaces employed in this work. Firstly, the Si wafers containing oxide films, were cut and ultrasonically cleaned in isopropanol for 10 min followed by washing with copious amounts of Milli-Q pure water (18.2 MΩ). The cleaned wafers were then immersed in 5 % HF solution for about 7 minutes to induce the dissolution of the surface oxides leading to the formation of the Si-H bonds on the surface (eq. 4 and Figure 9).[61,62]

$$SiO_2 + 6\,HF \longrightarrow [SiF_6]^{2-} + 2\,H^+ + 2\,H_2O \qquad \text{---------- (Eq. 4)}$$

The hydrophobic Si-H surface was then rinsed briefly with Milli-Q pure water and then treated with ozone gas (in an ozone chamber) for about 9 min to achieve slight surface re-oxidation to reproduce a thin oxide layer with Si-O bonds by removing some Si-H bonds.[63] The Si(111) wafers were finally treated with 40 % NH_4F solution for about 4 min in yet another H - termination step yielding atomically flat Si(111)-H surfaces, after which they were dried with N_2 gas and used immediately in the electrografting procedures.

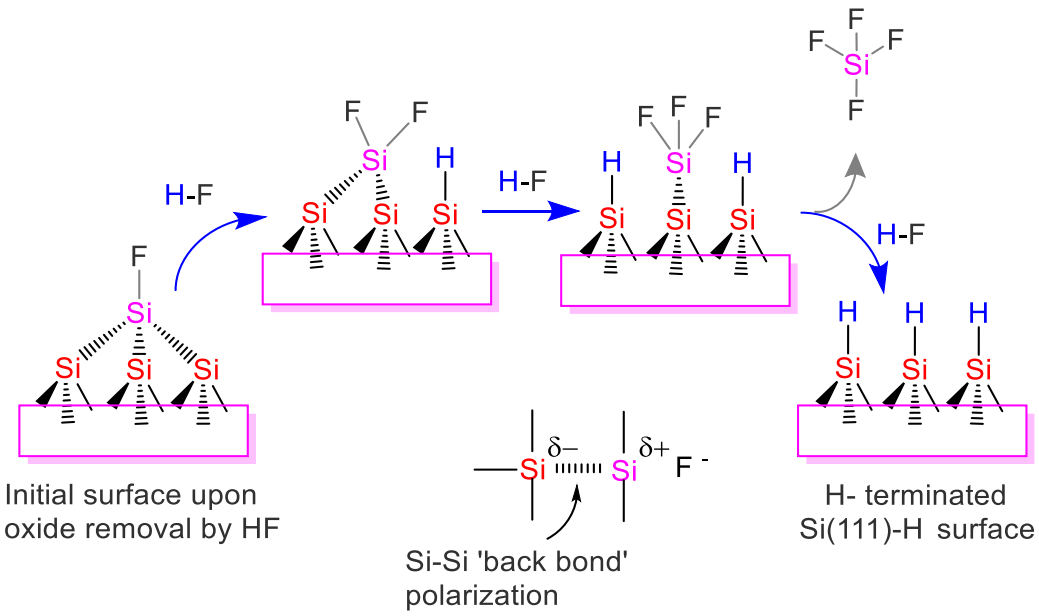

Figure 9: Schematic of the mechanism for the H-termination on Si(111) surface. (Adapted from ref.[64])

The mechanism for H- termination begins with polarization of the surface Si-F bond which destabilizes the Si-Si "back bonds". During this process, the surface Si-F bonds are sequentially formed and eliminated as valence satisfied water soluble SiF_x species, which eventually leads to the formation of a layer of substrate Si atoms that terminated by H atoms or the Si-H surface bonds (Figure 9).[62,64]

2.2 Cyclic Voltammetry (CV) and Chronoamperometry (CA)

Cyclic voltammetry (CV) is an electrochemical technique which measures the current that develops upon cycling (or applying) electrical potential to a working electrode surface.[65] In a CV experiments, the potential of the working electrode is cycled linearly versus time in a three electrode assembly set-up (using a potentiostat) in order to generate the current (*i*) response as function of the applied voltage (*U*) (Figure 10). The reaction of interest (such as surface modification on Si-H in this case) occurs at the working electrode (W.E). The potentiostat maintains a potential difference, *U*, between the reference electrode (R.E) and the W.E while supplying

the current (*i*) needed to effect electron transfer reactions happening at surface of the W.E.

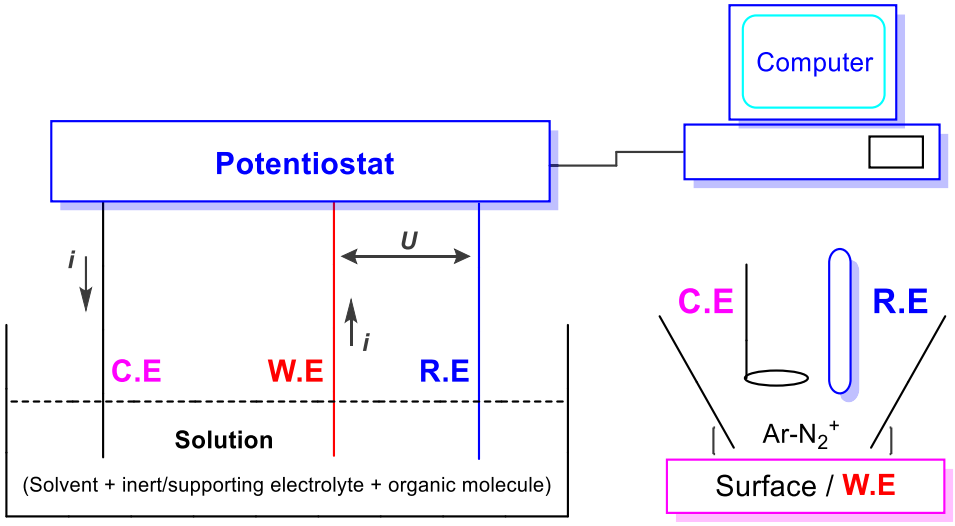

Figure 10: The electrochemical set-up with potentiostat connected in the three-electrode assembly unit.

The *i-U* or CV curve is then obtained by recording *i* as the applied voltage is slowly varied linearly with time. This is equivalent to controlling the energy of the electrons within the W.E material. The counter electrode (C.E) or auxiliary electrode completes the circuit. The solutions are composed of anhydrous acetonitrile (ACN - 98 % Pure Sigma Aldrich) as the primary solvent, the inert electrolyte 0.1 M tertbutylammonium tetrafluoroborate ($TBABF_4$) salt and the selected aryl diazonium derivatives bearing the chelating groups.

Figure 11 illustrates the behaviour of electrons in a metal electrode substrate such as Si, which can be understood by considering the Fermi level (E_F). This level in the electrode is not fixed, and can be varied by supplying electrical energy.[66] Depending on the relative position of the E_F, it may be thermodynamically feasible to reduce or oxidise an electroactive organic species (labelled “A” in figure 11) next to electrode surface in solution.[67,68]

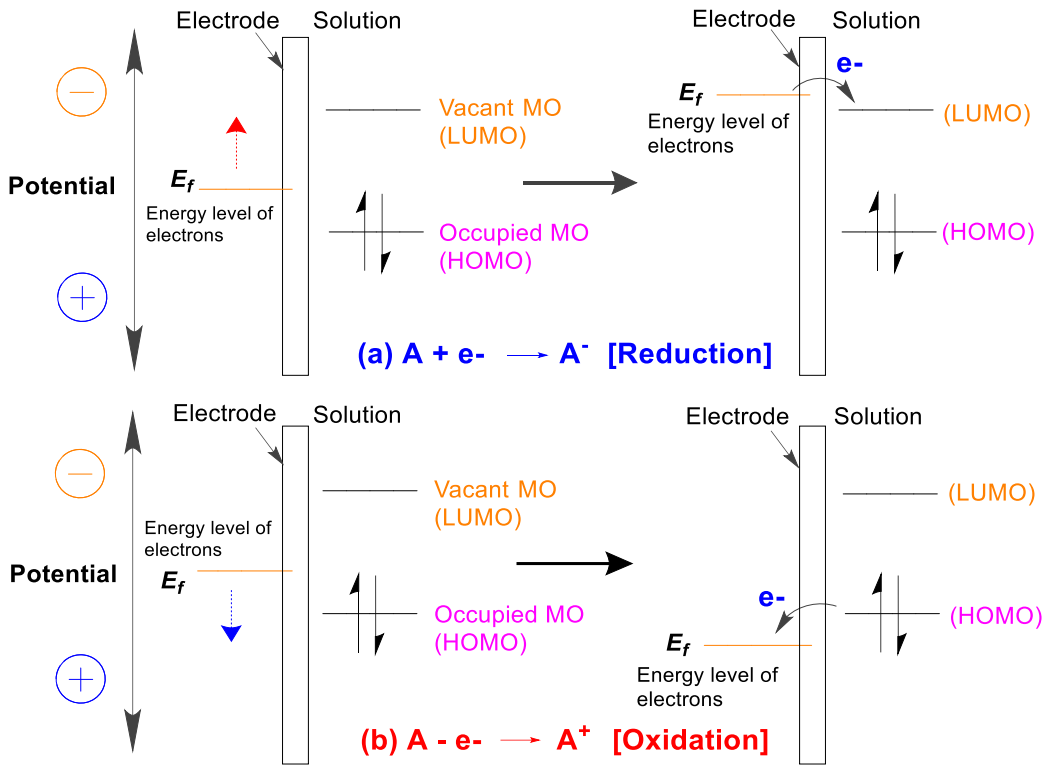

Figure 11: Illustration of redox reactions at electrode surface in relation to the Fermi levels. (Adapted from refs.[66,67])

Of interest in this work, was the cathodic electroreduction of aryl diazonium chelate derivatives. The substrate Fermi levels are driven to more negative or cathodic potentials (E_F moves higher in energy) in transfer electrons via quantum mechanical tunnelling effect into the vacant electronic states (lowest unoccupied orbitals, LUMO) of the electrophilic aryl diazonium cations (next to the surface). A broad cathodic reduction current indicating the concurrent charge flow observed in the resulting *i-U* or CV curve provides evidence of electroreduction process at the electrode surface.

Fixed voltages (electrical energy) can also be applied in a step-wise manner on an electrode surface using a potentiostat in a three-electrode assembly while monitoring the resulting current flow as a function of time in chronoamperometric (CA) experiments. When a fixed reduction potential of the species A is applied, the

reduction currents are typically observed to decay over time which signals an electroreduction reaction in progress.[67]

2.3 Electrochemical Quartz Crystal Microbalance (EQCM)

The principle of EQCM is based on perturbation of the resonant frequency f_o of the shear wave oscillations, which result from foreign mass deposition on a piezoelectric quartz crystal resonator. The bare quartz crystal acquires a fixed mechanical resonant mode and oscillates at a frequency f_0 when a sinusoidal electrical voltage is applied to it. The deposition of foreign mass on the QCM crystal leads to a drop in the resonant frequency and vice versa. In the EQCM set-up, the QCM crystal, which is set as the W.E in a three-electrode cell, is driven by an oscillator circuit to enable real-time tracking (or *in-situ* monitoring) of the resonant frequency changes of the crystal that occur upon mass depositions (Figure 12).

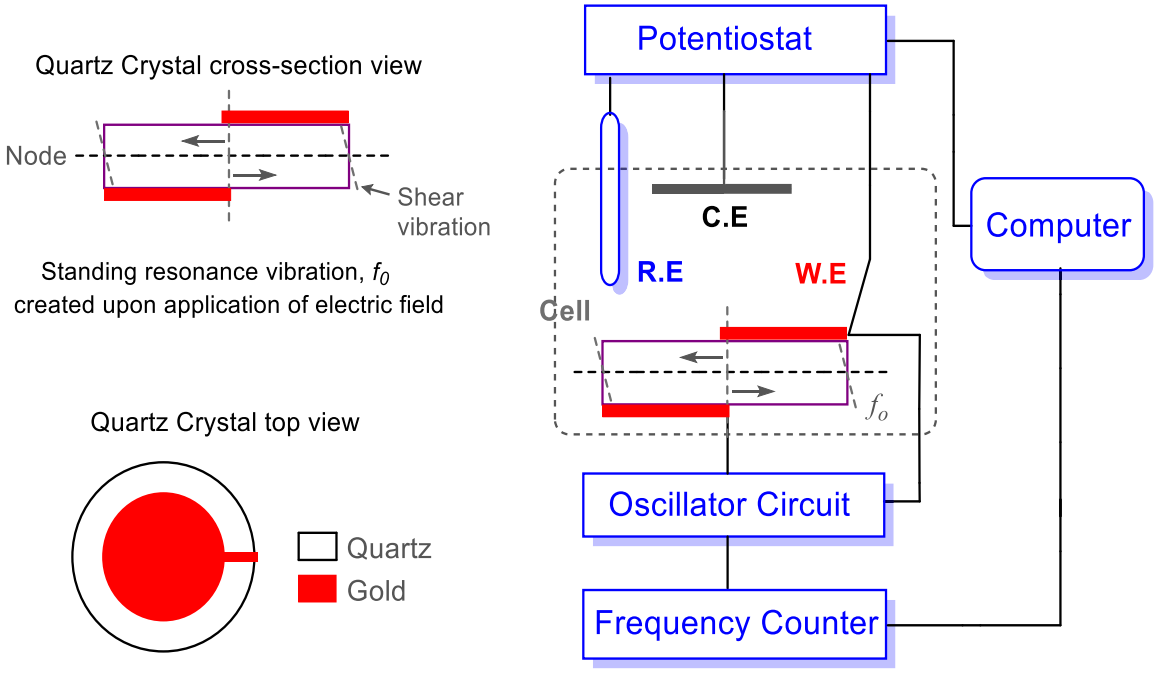

Figure 12: Schematic of the piezoelectric quartz crystal and the EQCM set-up.

A frequency counter records the frequency changes during the electrochemically-induced mass changes resulting from electrografting reactions (surface modification)

on fresh Au-QCM electrode surface. The frequency of oscillation is sensitive to foreign mass changes on the crystal surface as expressed by the *Sauerbrey* relation (eqn. 5): [67,69,70]

$$\Delta f = -2f_o^2 mn/\sqrt{(\rho\mu)} = -C_f m \quad \text{--------- (Eq. 5)}$$

where Δ*f* denotes the frequency change (Hz) caused by addition of a mass per unit area *m* to the crystal surface, *n* is the harmonic number of the oscillation (e.g., *n* = 1 for 5 MHz with a 5 MHz crystal), *μ* = shear modulus of quartz (2.947 x 10^{11} $g.cm^{-1}s^{-2}$), and *ρ* = density of quartz (2.648 g/cm^3). The constants are usually lumped together to formulate a new single constant term, the sensitivity factor C_f which has the value of 56.6 Hz $cm^2/\mu g$ for a 5 MHz AT-cut quartz crystal at room temperature.[71]

This means that the attachment (or deposition) of mass Δ*m* on the Au-QCM crystal causes a decrease Δ*f* in the resonant frequency f_0. In typical *in-situ* QCM experiments such as depositions of organic molecules (substrate modification), adsorption/desorption studies,[72,73,74] the Δ*f* is monitored with variation of potential of the working electrode. In this work, the recorded frequency change Δ*f* was converted into the corresponding mass change, Δ*m* (eq. 6) based on the *Sauerbrey* equation.

$$\frac{\Delta m}{A} = \frac{\Delta f}{C_f} \quad \text{---------- (Eq. 6)}$$

where *A* is the total disk area (Au coated) in cm^2 and $1/C_f$ = 17.668 ng/Hz (or 0.017668 μg/Hz). The Faradaic efficiency η_f for the electrografting process was estimated by dividing the actual measured mass deposited Δm_{EQCM} by the theoretically calculated mass based on charge flow Δm_{max}.[72,75]

$$\eta_f = \frac{\Delta m_{EQCM}}{\Delta m_{max}} = \frac{\Delta m_{EQCM}}{(M.Q)/(z.F)} \quad \text{---------- (Eq. 7)}$$

where *M* is the molar mass of the monomer, *z* is the number of transferred electrons, *F* is Faraday's constant (96 485.34 C/mol.), and *Q* represents the electrical charge related to the electroreduction.

2.4 Infrared Spectroscopic Ellipsometry (IRSE)

The IRSE is as a powerful, non-destructive and sensitive vibrational spectroscopic tool applied in the analysis of ultrathin organic films based on the measurement of elliptical polarization of the reflected light. It is based on the principle that the sample under probe interacts with the incident linearly polarized infrared light (electromagnetic wave) and transforms it into elliptically polarized light based on its molecular vibrations or structure (Figure 13). In this technique, the characteristic vibrational spectrum of a given sample (typically bound on a given surface) is acquired (or measured) and normalized against a spectrum of the bare surface as a reference.[76,77]

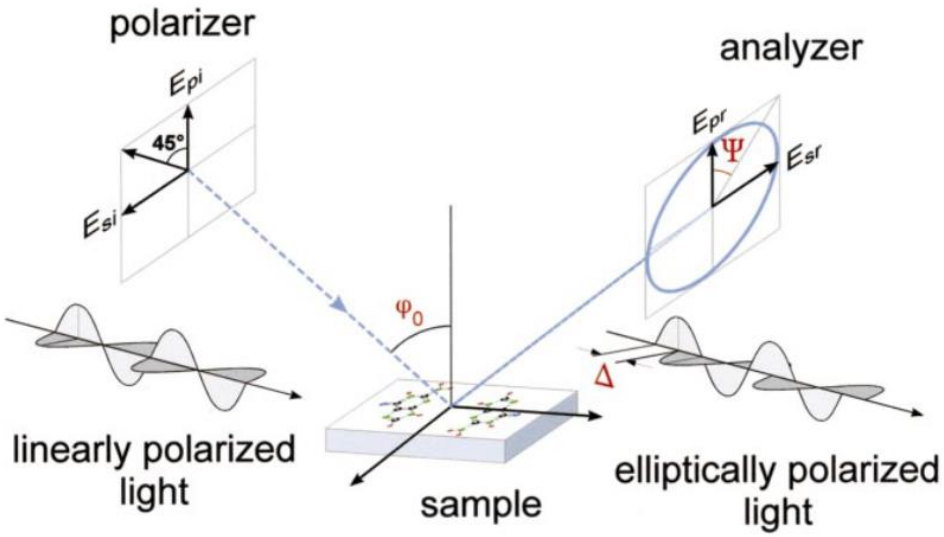

Figure 13: Schematic representation of the IRSE measurement principle. (Adapted from ref.[76]).

The state of polarization, emanating from the transformation of linearly polarized light into elliptically polarized light by the sample, can be described using two

ellipsometric parameters; the amplitude ratio (tan ψ) and phase shift difference (Δ) of the two orthogonally polarized components of the reflected wave (r_s and r_p) (see Figure 12). The ellipsometric parameters are defined by the quantity ρ, which is the ratio of the complex reflection coefficients r_s and r_p (equation 8):

$$\rho = \frac{r_p}{r_s} = \tan\psi\, e^{i\Delta} \qquad \text{---------- (Eq. 8)}$$

In recent years, IRSE has emerged as a formidable tool for probing the vibrational spectroscopic information of organic thin films (including modified Si surfaces) and their molecular structures.[76,78]

In this study, an IRSE spectrometer (TENSOR 37, Bruker, Germany), fitted with a mercury – cadmium – telluride (MCT) detector or a Bruker 55 Fourier-transform Infrared (FTIR) was used to acquire spectroscopic data. The IRSE vibrational spectral data obtained were used in the characterization of the surface molecular structures and dynamics with respect to the chelate electrografting on Si(111) and Au surfaces.

2.5 X-ray Photoelectron Spectroscopy (XPS)

The XPS is a surface sensitive analytical tool used to probe the elemental composition of materials, the chemical states of atoms including their binding partners. It is based on the irradiation of a sample with monochromatic X-rays, E = *hv* (e.g., the Al K_α excitation line at 1486.6 eV or the Mg K_α line at 1253.6 eV), which causes electrons to be ejected (photo-emitted) from the sample atoms into a surrounding vacuum (Figure 14).[79] The energy of the emitted photoelectrons is then analysed by the electron spectrometer and the data presented as a spectrum of intensity (usually expressed as counts or counts/s) versus electron energy.

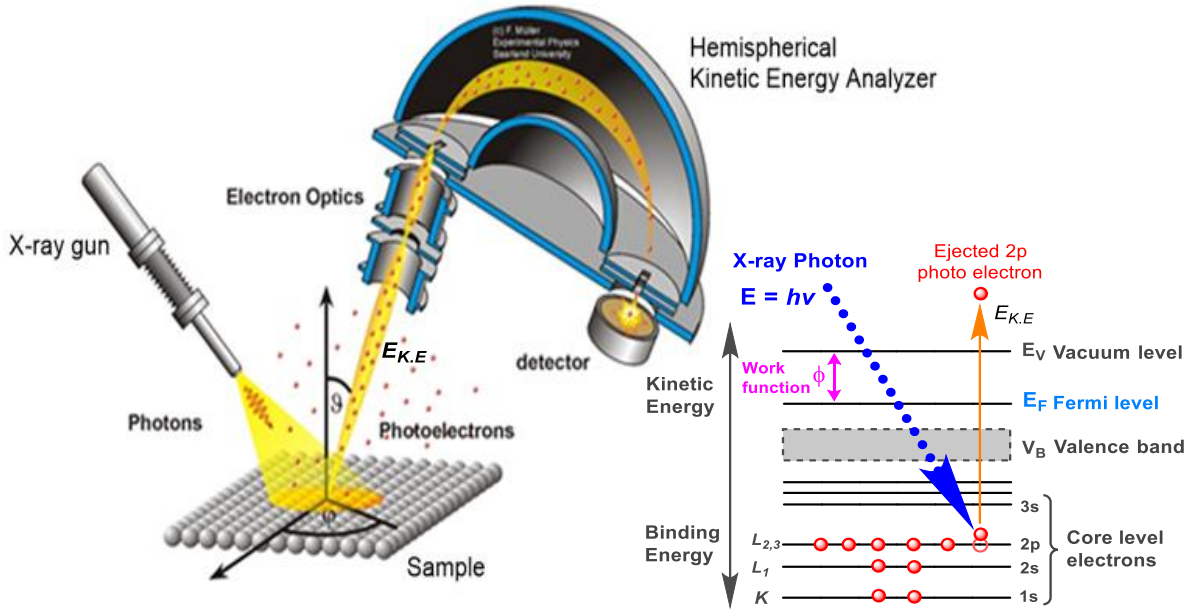

(a) Instrumentation of XPS (b) Working principle

Figure 14: (a) Schematic of the XPS instrumentation and (b) the photoemission measurement principle. (Adapted in part from ref.[80]).

The kinetic energy, $E_{K.E}$, depends on the photon energy of the X-rays used and is therefore not an intrinsic material property. The binding energy of the electron, $E_{B.E}$, is the parameter which identifies the electron specifically, both in terms of its parent element and atomic energy level.

The two parameters involved in XPS experiment are related as follows:

$$E_{K.E} = hv - E_{B.E} - \varphi \qquad \text{---------- (Eq. 9)}$$

where hv is the energy on incoming X-ray photon (h = Planck's constant, v = frequency) and φ is the work function of the spectrometer.

The Beer-Lambert's expression permits the use of XPS signals in confirming the existence of overlayer material (or thin films) on top of a given surface and can further be used to estimate the thickness via signal attenuation experiments, which are based on sampling depth parameters.[79,81] A comparison of intensities of the

same photoelectron before and after thin film deposition on the surface can be used to decipher the thickness of the surface bound overlayer material (Figure 15).

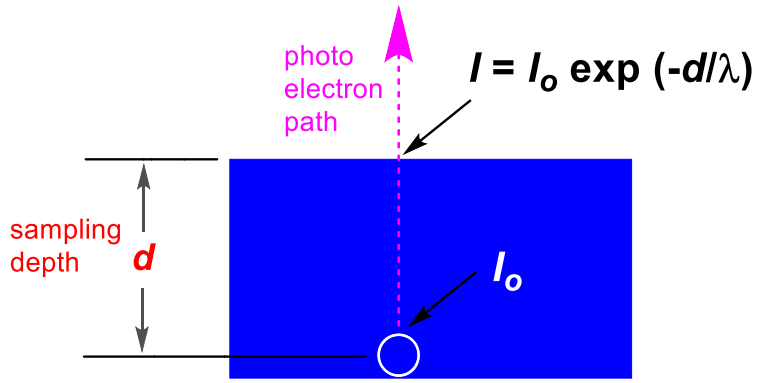

Figure 15: Schematic representation of Beer-Lambert law for XPS sampling depth profile. (Adapted from ref.[81]).

The intensity of a photoelectron, I_o, emitted at a depth, d, below the surface (or on a bare surface), attenuates or decays due to inelastic scattering of some of the photoelectrons as they traverse through a layer, if the overlayer material exists. The emission of photoelectrons I as a function of the depth d is predicted by the Beer-Lambert equation:[81]

$$I = I_o \exp\left(-d/\lambda_{(E_{K.E})}\right) \qquad \text{---------- (Eq.10)}$$

where I_o = the intensity of the emitted photoelectron on clean surface (bare surface with no layer) and I = the intensity of the same electron after attenuation due to introduced overlayer on the surface, d = sampling depth (which depends on the overlayer thickness), and λ (nm) is the depth of analysis (or attenuation length of photoelectrons) which is synonymous to inelastic mean free path (IMFP) that is dependent on the nature of substrate and the kinetic energy $E_{K.E}$ of the photoemission. The values of λ are derived from the IMFP universal curve.[81,82]

In this work, XPS instrument was used to acquire spectral data for the investigation of the chelate functionalized Si(111) and Au substrate. Signal attenuation

experiments using the Si2p peak were conducted to investigate surface functionalization and HMI uptake. The binding of the heavy metals on the chelate modified surfaces was also investigated and characterized using XPS signals related to the ligand donor atoms such as the N1s, S2s and C1s of the O=C-O- group. The National Institute of Standards and Technology (NIST) XPS spectral database was used as a reference in this work.[83] The Shirley baseline computation employing Voigt fitting functions were used to deconvolute selected XPS signals.

2.6 Raman Backscattering Spectroscopy

Raman spectroscopy is a technique based on the use of scattered light to study molecular vibrations. Raman backscattering experiments involves the excitation of a sample with monochromatic laser photons to cause intense backscattering. The incident photons can be imagined as raising a molecule to a "virtual state," which is a non-stationary state of the system. Immediate re-emission without loss of energy causes "Rayleigh scattering", while the re-emission to a final state other than the original state (usually $1/10^6$ of the re-emitted photons) produces the "Raman effect" (Figure 16).[84]

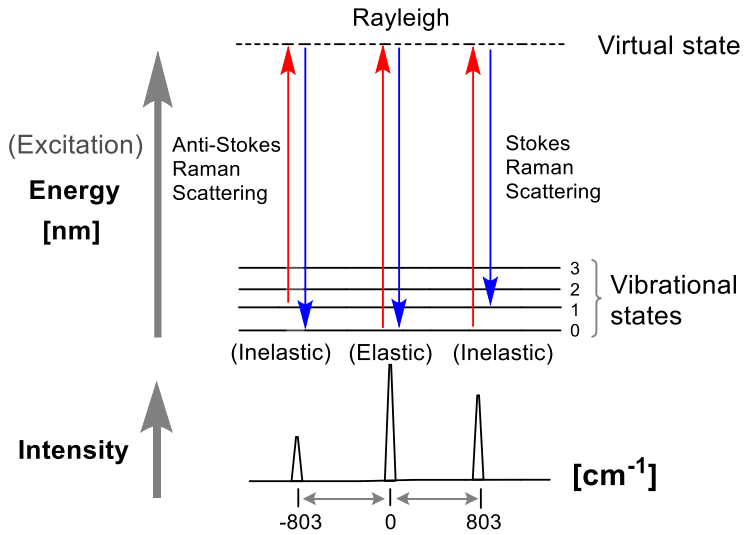

Figure 16: Schematic illustration of the Raman scattering.
(Adapted from ref.[84]).

In Raman backscattering experiments, discrete energy differences relative to the energy of incident light are observed based on the molecular polarizability, which refers to the deformability of the electron cloud about the molecule brought about by the external electric field from the incident radiation.[84] The observed differences (or shifts) in energies in the scattered photons correspond to the quanta of vibrational modes related to molecular bonds present in the scattering molecule.[84] Since the distinct peaks in the Raman spectrum are based on the chemical formula, structure of the compound, functional groups, and skeletal vibrational modes, the technique can be useful for monitoring molecular dynamics during a given chemical reaction and also in identifying samples using on empirical characteristic absorption bands or fingerprint spectra.

The strength or intensity of a given Raman signal, I_R, is proportional to the power of the incident laser among other parameters described in eq. 11.[84] This generally means that the application of shorter excitation wavelength (or higher energy) laser radiation can increase the value of I_R.

$$I_R = v^4 I_o N \left(\frac{\partial \alpha}{\partial Q}\right)^2 \qquad \text{-------- (Eq. 11)}$$

where I_o is the incident laser intensity, N is the number of scattering molecules, v is the frequency of the exciting laser, α is the polarizability of the sample molecule and Q is the vibrational amplitude.[84]

Two key aspects in Raman spectroscopy based on eq.11 are: Firstly, the signal is concentration dependent hence can permit quantitation. Secondly, only molecular vibrations that result into change in polarizability are Raman active and can be

detected as long as the differential change in polarizability with respect to the vibrational amplitude, *Q* is more than zero.

In recent years, Raman spectroscopy has been used in the vibrational characterization of organometallic complexes. Modern laser optics systems and high performance charge coupled device (CCD) detectors have been incorporated into its instrumentation for improved data acquisition.[85] In this work, a Raman spectrometer fitted with a CCD detector was used to probe existence of metal - organic binding and to diagnose the molecular dynamics (including bathochromic/red shifts if any) that characterize heavy metal binding on the chelate modified surfaces. A laser excitation source of 632.8 nm was used in the spectral data acquisition. The Raman spectra of the hydrated metal salts were also obtained in this work for reference purposes.

2.7 Treatment of the Chelate-Modified Surfaces with HMI Solutions

A number of complexation recipes (involving systematic changes temperature and HMI concentration, and reaction times) were investigated by treating the functionalized surfaces with droplet aliquots of the HMI solutions. The recipes that produced evidence of surface bound chelated metals (indicating HMI's binding on modified Si surfaces) based on solid-state Raman backscattering measurements are reported herein.

For the chelation experiments with carboxymethylthio – functionalized Si(111) surface Si-(4-CMTB), solutions of Cu(II) and Pb(II) were prepared and used in the investigation. The Cu ion solution (965 ppm) was prepared by dilution of weighed anhydrous copper(II)chloride ($CuCl_2$, 99.0 %, Sigma-Aldrich) in hot water (~ 55^{o}C).

The functionalized surface Si-(4-CMTB) was then treated with this solution by shaking using an orbital shaker (Neolab, GmbH; DOS-20S) at 200 revolutions per minute for 5 mins. The reaction chamber was then sealed with a transparent parafilm and left to soak for about 48 hours in a hood. The Cu^{2+} solution was later carefully drained off (in HMI waste container) and the treated surface, Si-(4-CMTB)-Cu, cleaned in ultrasonic bath for 5 min and dried with a stream of nitrogen gas.

Lead ion solution (400 ppm) was prepared by dilution of weighed anhydrous lead(II)nitrate ($Pb(NO_3)_2$, 99.0 %, Sigma-Aldrich) in warm water (~ 40 ^oC). The functionalized surface Si-(4-CMTB) was then treated with this solution by shaking using an orbital shaker (Neolab, GmbH; DOS-20S) at 90 revolutions per minute for 3 mins. The reaction chamber was then sealed with a transparent parafilm and left to soak for about 72 hours in a fume hood. The residual Pb-ion solution was later carefully drained off (in HMI waste container) and the treated surface Si-(4-CMTB)-Pb, was washed briefly with ice-cold water and finally dried with a stream of nitrogen gas.

In the case of the piperazinyl – functionalized Si surface, the Cu-ion solution (250 ppm) was prepared by dilution of weighed anhydrous $CuCl_2$ (99.0 %, Sigma-Aldrich) in warm water (~40 ^oC). The functionalized surface Si-(4-PPzB) was then treated with this solution by shaking using an orbital shaker (Neolab, GmbH; DOS-20S) at 120 revolutions per minute for 4 mins. The reaction chamber was then sealed with a transparent parafilm and left to soak for about 72 hours. The Cu-ion solution was later carefully drained off (in HMI waste container) and the treated surface, Si-(4-PPzB)-Cu, rinsed slightly with ice-cold water for 1 min., after which the surface was dried with a stream of nitrogen gas.

3.0 RESULTS AND DISCUSSION

3.1 Pre-treatment of Si Substrates (H-Termination)

Figure 17 shows the IRSE spectra of the H-terminated Si(111) surfaces derived from the investigation of the two pre-treatment recipes employing different surface re-oxidation reagents; namely, ozone (O_3) gas and piranha (H_2O_2/H_2SO_4) solution. Samples A and B were exposed to O_3(g) treatments in the re-oxidation phase as described in section 2.1. Sample A was left in air for about 48 hours after the H-termination treatment to serve as a reference while the measurement for sample B was done about 30 minutes after the pre-treatment process. Sample C was treated with piranha solution in the re-oxidation phase for a comparative analysis.

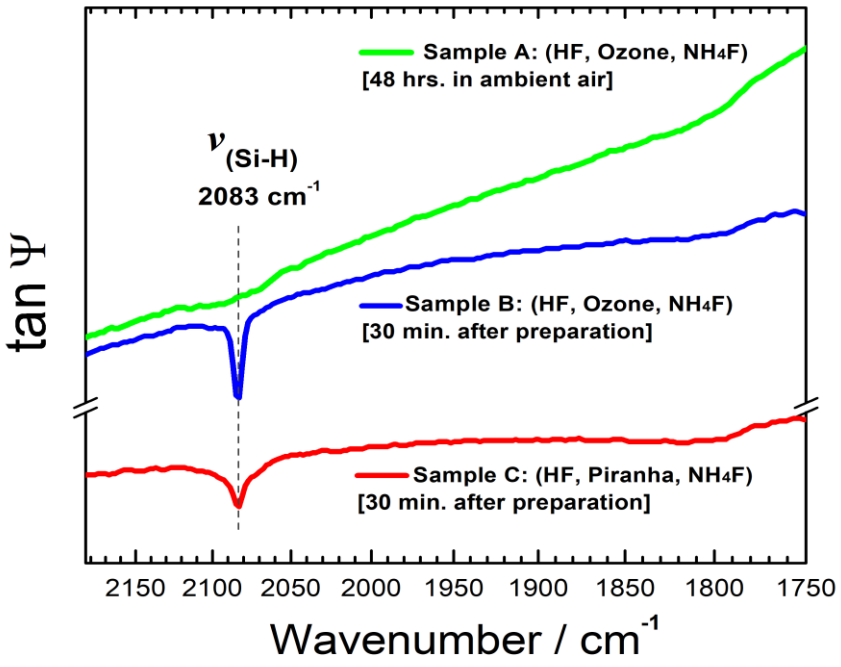

Figure 17: IRSE spectra highlighting the Si-H signals arising from the different methods of H-termination of the Si(111)-H substrate surface.

The sharp peak appearing at about 2083 cm^{-1} in both samples B and C characterized the formation of Si-H bond upon the H-termination procedues.[64] This shows that both the pre-treatment methods investigated were successful in producing the Si-H surface bonds. However, the IRSE spectrum of sample A illustrates the disappearance of the Si-H absorption band after about 48 hours, which shows that the Si-H surface bonds are unstable in nature when exposed to air.

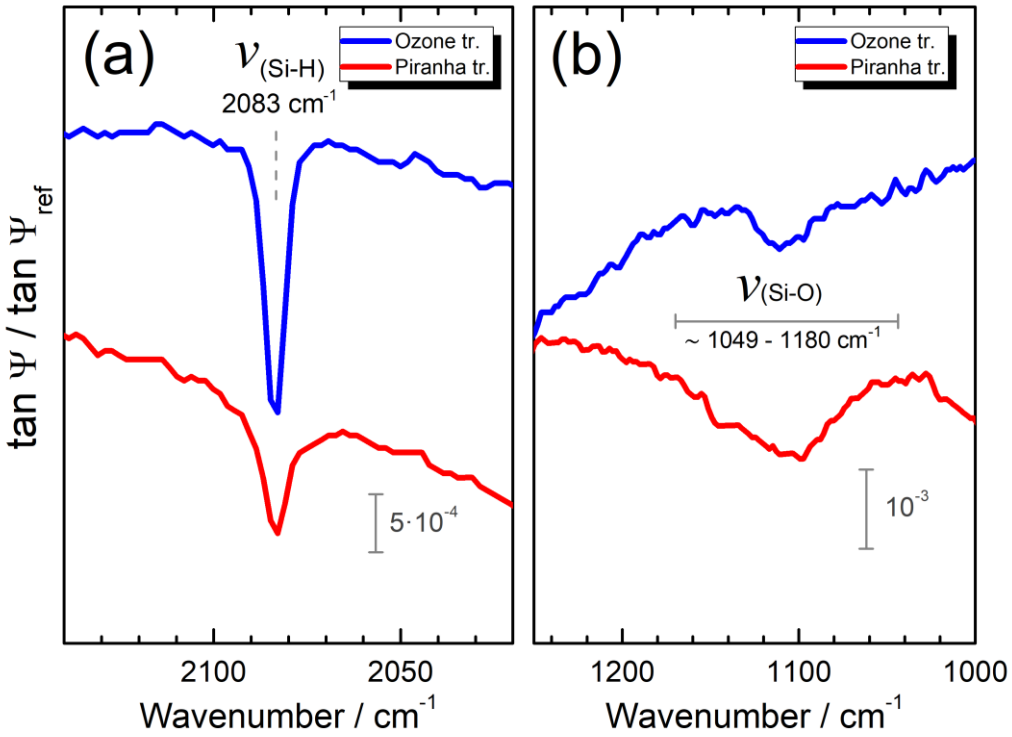

Figure 18: IRSE graphs highlighting (a) the Si-H and (b) the Si-O absorption bands on the Si(111)-H substrates pre-treated with O_3(g) (blue) versus piranha solution (red).

Figure 18 shows an extension of the comparative IRSE spectra of Si(111) substrate surface subjected to the two H-termination pre-treatment methods. Figure 18a shows that the formation of Si-H bonds via the pre-treatment procedure involving O_3(g) is more pronounced in comparison the one that involves piranha treatment based on a comparison of their Si-H absorption peak intensities. Figure 18b shows the vibrational bands related to the Si-O bonds.[86,87] A comparison of the magnitude of

the intensities of the Si-O absorption peaks shows that the pre-treatment procedure involving piranha produces relatively more Si-surface oxides than in the case of O_3(g) pre-treatment. The extra surface Si-oxides perhaps contributes to the broadening and reduction in intensity of the Si-H signal of the piranha treated Si(111) surface. The sharpness of the Si-H absorption band in the O_3(g) treated surface hints towards a more regular and ordered H-terminated surface structure in comparison to the one obtained for piranha pre-treatment.

It can be concluded that the treatment of Si(111) substrate surface tends to produce a higher surface coverage of the H – terminated Si(111) surface atoms as opposed to those produced by the piranha pre-treatment procedure. The use of O_3(g) in the re-oxidation reaction step in the H-termination procedure of Si(111) as illustrated in this work is important finding that may potentially in future contribute towards minimizing the usage of the piranha solutions in H-termination procedure, hence mitigating the corrosive and explosive hazards related to piranha usage.[88]

3.2 Surface Modification with Carboxymethylthio (CMT) Chelate

The carboxymethylthio (CMT) groups contain sulphur (S) and oxygen (O) donor atoms in suitable orientation for the bidentate chelation of heavy metals. The structure of the CMT group (see Figure 19) is closely related to that of dimercaptosuccinic acid (DMSA), also called "Succimer", which has been used for the pharmacological treatment of some HMI toxicity conditions.[89] It follows that the successful functionalization of a surface with CMT chelating ligands would provide a facile way for developing kits for applications that involve the rapid trapping and/or removal of Pb and Cu. One potential future diagnostic biomedical application would be the fabrication of disposable forensic toxicological assay chips for the HMI detection/sensing and trace-level extraction from biological fluids, such as urine or blood.

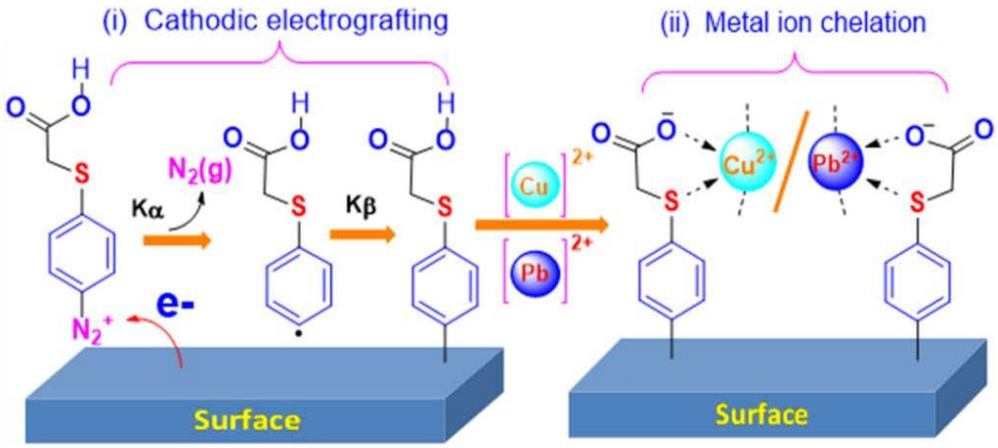

Figure 19: (i) Surface functionalization with CMT groups and (ii) chelation of either Cu or Pb.

This section describes the results obtained from the electrochemical functionalization strategy which entails introducing CMT chelating groups via the direct electroreduction of the diazonium cation 4-(carboxymethylthio)benzenediazonium - (4-CMTBD) onto Si(111)-H surfaces (Figure 19). The uptake and binding to Cu and

Pb ions via the CMT chelating ligands on the modified Si surface is also qualitatively investigated and characterized by spectroscopic methods. In addition, the electroreduction of 4-CMTBD molecules on Au surface is studied by the electrochemical quartz crystal microbalance (EQCM) experiments.

3.2.1 Electroreduction of 4-(Carboxymethylthio)benzenediazonium cation [4-CMTBD]

Figure 20 shows the (a) CV and the corresponding (b) CA curves obtained from the cathodic electrografting of 4-CMTBD on the Si(111)−H surface. Figure 21 depicts the (a) CV and the corresponding (b) CA curves for electrografting of 4-CMTBD on the Au surface. As evident in their CV graphs, the electroreduction of the 4-CMTBD diazonium cations is observed by the characteristic first broad cathodic reduction wave (Figures 20a and 21b). In both cases, the second cathodic potential cycles (or second CV waves) depict marginal cathodic reduction waves with respect to the first waves, which characterize the blockage of the surface by the grafted 4-CMTB molecules in the first scan.

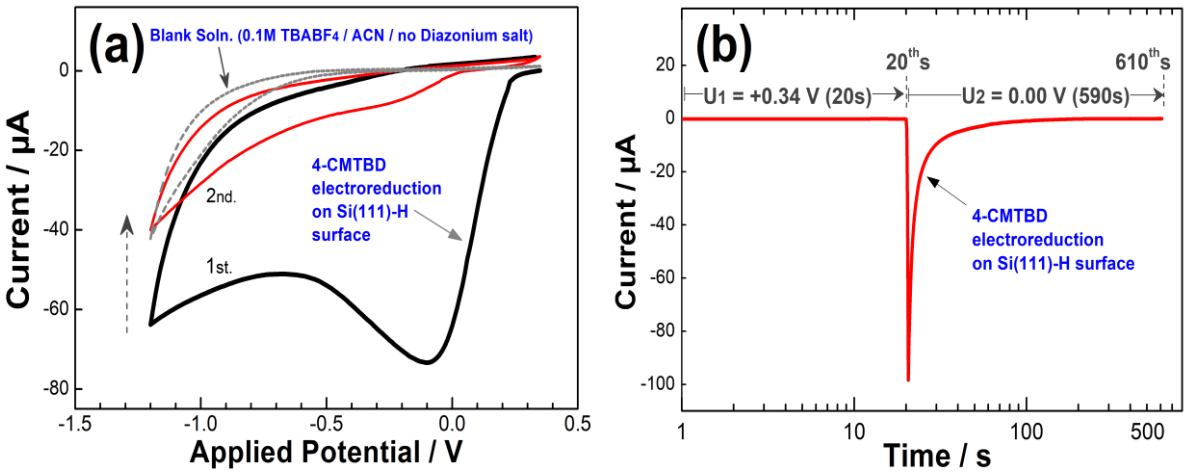

Figure 20: (a) CV and (b) CA for the electroreduction of 5 mM 4-CMTBD on Si(111)-H surface.

On the Si(111)−H surface, the reduction of 4-CMTBD starts at about +0.24 V, reaching a peak at about −0.10 V. A solution containing (ACN + 0.1 M $TBABF_4$) with no diazonium salt labeled 'blank' (depicted as the hatched grey curve) shows no characteristic broad reduction peak its cathodic CV on the same Si(111)-H surface (Figure 20a). The 'Blank' CV only registers some reduction at about -1.2 V, which is related to the cathodic potential window of the inert electrolyte solvent.

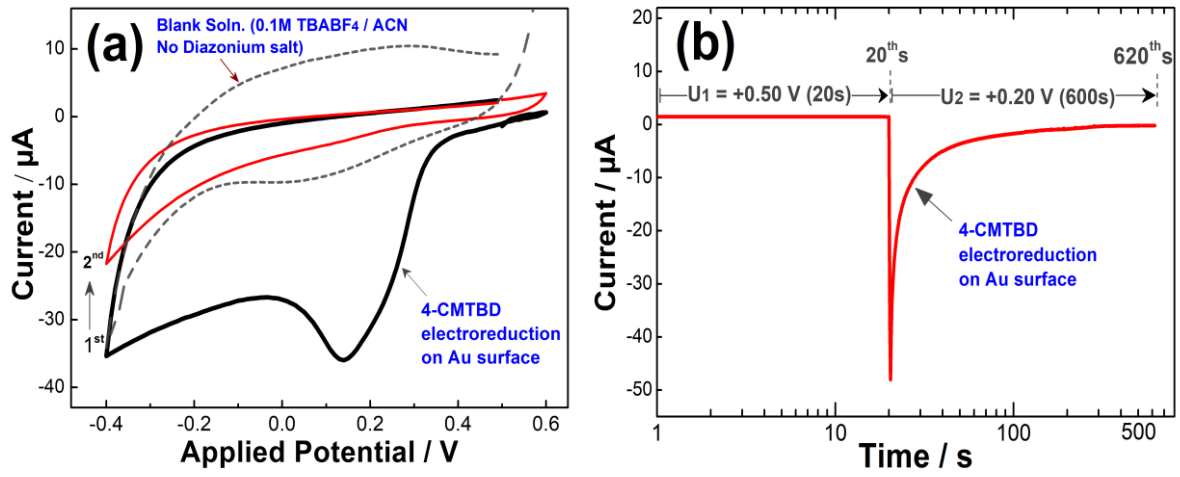

Figure 21: (a) CV and (b) CA for the electroreduction of 5 mM 4-CMTBD on Au surface.

On the Au surface (Figure 21a), the reduction of the 4-CMTBD molecules starts at an onset potential of about +0.42 V and reaches a peak at about +0.14 V during the cathodic cycle. The 'blank' solution in this case shows no reduction peak at +0.14 V, providing a confirmation that the observed reduction in the first broad cathodic wave for the solution containing the 4-CMTB molecules is due to electroreduction of 4-CMTBD on the Au surface.

The respective CA graphs shown in Figures 20b and 21b, reveal characteristic sharp drops in currents indicating the rapid electroreduction of 4-CMTBD cations, which is the principal reaction leading to surface modification. The steep decay in currents only occur when the reduction potentials are applied at fixed voltages and they

represent the gradual blocking of the electrode surface due to the electrografting of 4-CMTB units on the Si(111) and Au surfaces.[36]

The conventionally accepted aryl diazonium electrografting mechanism on the Si(111)−H surface is known to proceed via the silyl and phenyl diazonium radical couplings in a termination step, which leads to formation of closely packed surface-bound phenyl layers on the substrate.[36,58,78,90] The formation of Au−carbon covalent bond resulting from the grafting of phenyl groups via reduction of diazonium salts has previously been confirmed by surface-enhanced Raman scattering (SERS) technique.[42]

Figure 22 is derived from the integrated CA graphs directly obtained from the electroreduction of 4-CMTBD on Si(111)-H and Au surfaces. At the onset of the electroreduction reactions (when the fixed reduction potentials are applied right after the 20th second), the curves depict the variation of electroreduction-dependent charge transfer over time during the electroreduction of 4-CMTBD. It can be noted that within the first 20 s, when fixed voltages of +0.34 V (on Si) and +0.50 V (on Au) are applied, no significant charge accumulation occurs. However, only slight amount charge accumulation on the Au surface seems to develop in this region. Two factors that can possibly contribute to the marginal rise in charge is the spontaneous electrografting of 4-CMTBD on the Au surface or the minimal adsorption of the thioether or sulphur (S) – containing 4-CMTBD molecules on the Au surface based on the affinity of S for Au atoms. The spontaneous deposition of thioether groups on Au surface is a phenomenon that has previously been reported.[91]

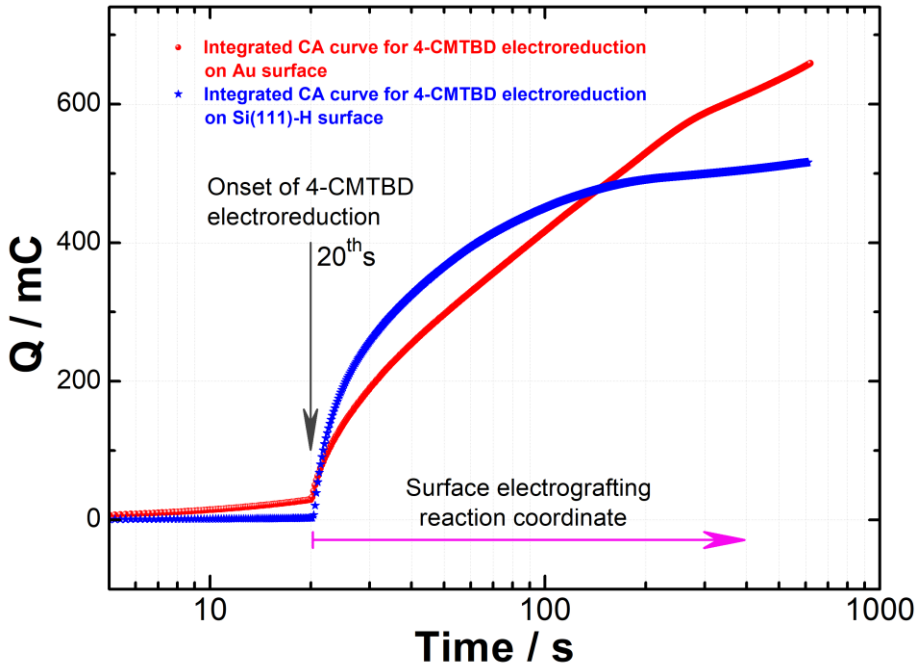

Figure 22: Charge flow (Q) obtained from the integrated CA graphs for the electroreduction of 4-CMTBD on Si(111)-H and Au surfaces.

The sudden and sharp rise in the charge flow (*Q*), in both cases (after the 20th s onwards) depicts the onset of the electroreduction for the 4-CMTBD, which signals the surface electrografting reaction. The time axis therefore mimics the reaction coordinate since the reduction reaction is an electron transfer process. The accumulation of charge ($Q = I \cdot t$), where *I* is current and *t* is time; at the onset of electroreduction is expected to occur at rapid rates initially and to decay gradually as the surface is modified during the electrografting reactions. This is because the grafted units gradually inhibit the electron transfer process between the electrode surface and conducting species in the electrolyte during the electroreduction process.

Figure 22 also gives further comparative information on the reaction paths or hints about the mechanisms for the electrografting of 4-CMTB on the Si(111)-H and Au surfaces, which may not be obvious in the CA graphs. Both trends in the *Q* versus *t*-

plot describe the general electrografting behaviour from the onset of the reaction and as it proceeds.

A peculiar observation in the reaction coordinate curve for Au surface is the appearance of linear curve within fairly significant time interval (approximately between the 20th to 110th s) during the reaction as opposed to the corresponding reaction coordinate curve for the Si-(111)-H surface, which largely resembles an exponential decay trend throughout the reaction. Based on this disparity, it can be argued that, under similar conditions, the electrografting of 4-CMTBD on Au surface is affected or inhibited to some extent by an extra competing side reaction. Gold atoms are not only known to possess exceptional affinity for thioether groups but also their surface atoms in a substrate can also possess a number of crystallographic facets.[91,92,93] One factor that may contribute to the observed disparity in the case of electrografting reaction on Au surface here is the presence of a possible competing mechanism such as the association or adsorption of the S atoms (of the thioether group of the 4-CMTBD cations) with the Au surface atoms during the random radical formation in the electrografting process.

3.2.2 EQCM Measurements: Electrografting of 4-CMTB on Au Surface

Figure 23 shows the results of the EQCM measurement depicting the corresponding mass change as calculated using eq. 6 (in section 2.3) from the measured real-time frequency change recorded during the electrochemical grafting of 4-CMTBD on Au surface. Figure 23a shows that the mass deposition due to electrografting of 4-CMTBD on Au surface increases more rapidly and by the greatest amount within the first CV cycle (Figures 23b). However, the detected change in mass per unit area, $\Delta m^* = \Delta m/A$, (eq. 7), in the subsequent cycles gradually decreases (Figure 23a).

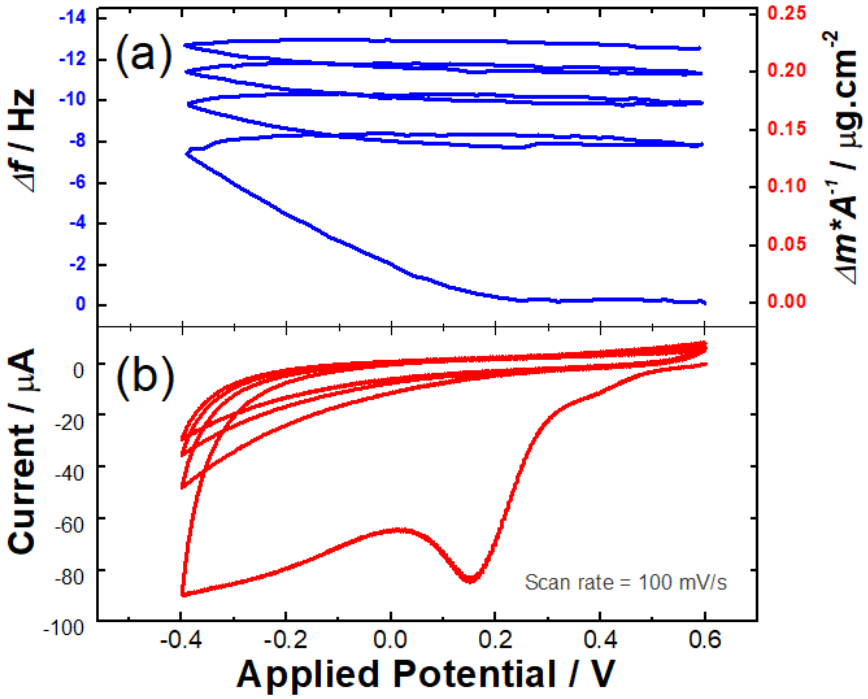

Figure 23: The variation of EQCM frequency shifts (*Δf*) and the corresponding mass change (*Δm*) in relation to the CV obtained from the electrografting of 4-CMTBD on Au surface.

The recorded CV from the electrografting of 4-CMTBD on the Au surface on QCM chip (Figure 21b) shows similar cathodic peak potential (of about +0.14 V) to the obtained from the Au surface anchored on glass substrate (Figure 19a). The characteristic first broad reduction peak disappears in the subsequent scans in both CV's. This electrodeposition behaviour characterizes the passivation of the Au surface due to grafting of the 4-CMTB molecules generated during the cathodic electroreduction of 4-CMTBD cations.

Figure 24 shows a plot of the quantified EQCM mass depositions versus the corresponding charge flow (Q) for the respective cycles determined from the electrodeposition of 4-CMTBD on Au surface. It shows that the greatest increase in mass deposition is accompanied by the greatest amount cumulative charge transfer,

which occurs only in the first. The charge transfer per cycle, however, diminishes in the successive scans.

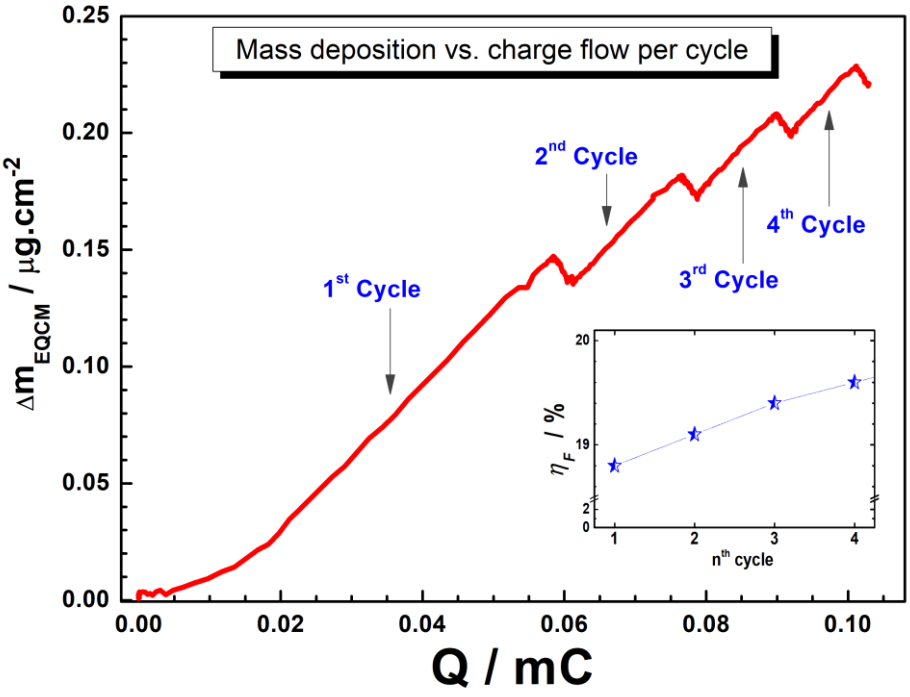

Figure 24: Plot of the deposited mass per unit area (*Δm*EQCM) vs. cumulative electrical charge Q for the first four CV cycles in the electrografting of 4-CMTB on Au surface.

The charge transfer increments and their dependence on the mass depositions in the respective CV scans, demonstrates that the initially grafted layer(s) of 4-CMTB units in the first cycle participate in impeding or inhibiting the electron transfers in the subsequent scans. This corresponds to a reduction of the deposited masses recorded in subsequent cycles. The respective average gradients for the mass changes with respect to charge flow in the first four cycles remain almost the same. This indicates that the deposition efficiencies for each of cycles are comparable because the ratio $\Delta m_{EQCM/Q}$ is proportional to ηF (eq. 8, section 2.3).

The inset chart in Figure 24 is a plot of the Faradaic efficiencies, ηF, obtained from the electrografting process as calculated by eqn. 8. The approximate grafting efficiencies achieved in this experiment ranges from about 18.8 – 19.6 % in the first

four cycles. This hints towards the existence of side reactions other than the aryl diazonium generated radical binding directly to surface atoms. Some possible side reactions would include that of an aryl radical to aryl radical binding close to the surface or the aryl radical binding onto surface grafted 4-CMTB units.

3.2.3 IR Spectroscopy: Molecular Structure of the 4-CMTB Modified Surfaces

Figure 25 shows the transmission-mode FTIR spectrum of the powder sample of the prepared aryl diazonium salt, 4-CMTBD (orange line) plotted in the same graph alongside with the IRSE spectra of the modified surfaces, Si-(4-CMTB) and Au-(4-CMTB) (blue and red lines, respectively). The IRSE spectra are normalized against the respective non-functionalized Si and Au substrates. The spectrum of the 4-CMTBD salt reveals the IR absorption bands of its phenyl ring (Ph), the carbonyl (C=O) and the diazonium ($N\equiv N^+$) groups at about 1560, 1720, and 2256 cm^{-1}, respectively. The IRSE spectra of the electrochemically fabricated Si−(4-CMTB) and Au−(4-CMTB) surfaces illustrates the complete disappearance of the diazonium groups at 2256 cm^{-1}. This is attributed to their transformation to N_2 (g), which is lost during the electroreduction reaction on the surfaces.

The decrease of the erstwhile present Si-H bonds after surface electrografting is also evidently characterized by normalized Si-(4-CMTB) spectrum, where v(Si-H) signal (at about 2083 cm^{-1}) points upwards with the respect to the other absorption bands present on the surface. The disappearance of the diazonium groups and Si-H bonds observed here support the proposed electrografting mechanism cited earlier in section 1.4.

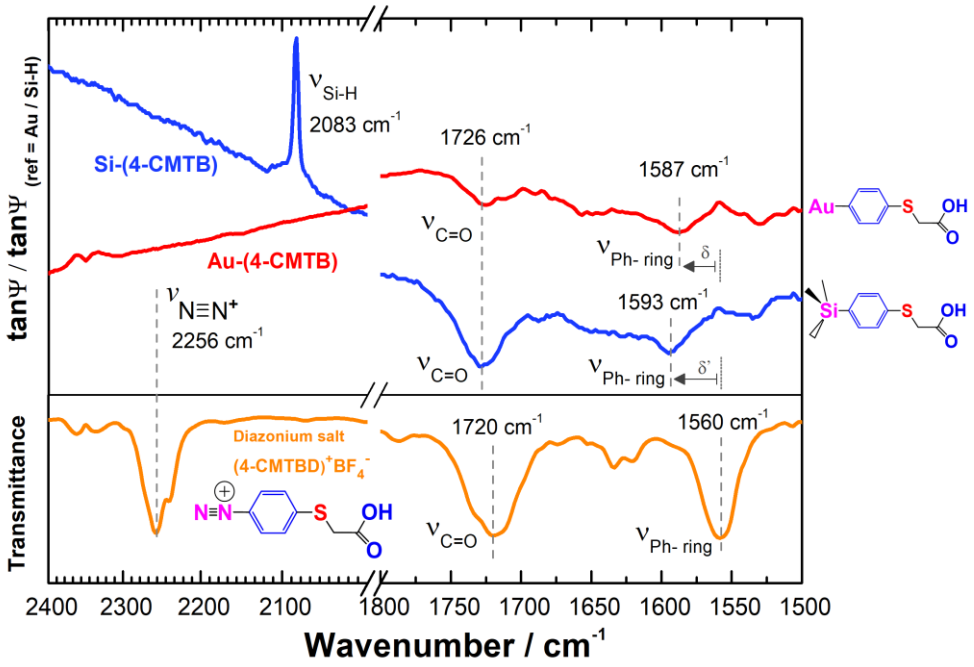

Figure 25: IRSE tan ψ spectra of: the Si−(4-CMTB) surface (blue line) and the Au−(4-CMTB) surface (red line) and the IR spectrum of the diazonium salt 4-CMTBD (orange line).

The Ph- ring and C=O absorption bands remain present on the surfaces after the electrografting process though somewhat shifted to ~1590 and ~1726 cm^{-1} respectively upon electrografting. The observed shift (δ) in the C=O absorption band on the modified surfaces with respect to the C=O signal of the 4-CMTBD salt is about 6 cm^{-1}. The Ph- ring vibration bands the case of both the Si−(4-CMTB) and Au−(4-CMTB) surfaces are observed to shift to higher wavenumbers by approximately 30 cm^{-1} with respect to the original 4-CMTBD pure salt. The shifts in the Ph- ring absorption peaks after surface electrografting can be attributed to an alteration in their nature of binding, which arises from the resultant loss of the erstwhile present ($N\equiv N^+$) groups and leading to their subsequent grafting onto the substrate surface.

The infrared spectra discussed herein provide evidence of the presence of 4-CMTB molecular units on the modified surfaces. They confirm successful surface functionalization in which the pendant CMT groups are introduced onto the surface un-degraded (based on the observed C=O bond) along with the substrate bound Ph-groups on both Si(111) and Au surfaces.

3.2.4 Kinetics of [4-CMTBD] Electroreduction on Si(111)-H and Au Surfaces

A measurable physical characteristic whose values depend on the concentration of a given reactant versus time can be used to determine the rate of the reaction under investigation.[94,95] The aryl diazonium cations are electrophilic in nature [96] and their electroreduction on surfaces (as monitored by CA experiments) are often characterized by very sharp decrease in currents, which do not obey a Cortell equation but are related to the charge transfers that occur due to the electroreduction reactions responsible for rapid blocking of the electrode surface (surface modification).[36] In this study, the 4-CMTBD molecule is the principal organic reactant undergoing electroreduction next to the electrode surface and its concentration is expected to decrease as a function of time during the chronoamperometric electrografting process. The disappearance of the diazonium groups at about 2256 cm^{-1} in IR spectroscopy (section 3.2.3) also attests to the conversion of 4-CMTBD to the surface grafted 4-CMTB units from the electroreduction reaction. It follows that the experimental CA graphs (a plot of the current response as function of the electroreduction time) can permit the derivation of the kinetic equation for the conversion of 4-CMTBD to 4-CMTB that is responsible for surface electrografting.

In general, the instantaneous rate of disappearance of a reactant species over time can be expressed by integrated rate law expressions. The integrated rate laws for first- and second- order kinetics are expressed by equations 12 and 13: [97]

$$\ln[A] = -kt + \ln[A_o] \qquad \text{(First – order)} \quad \text{--------- (Eq. 12)}$$

$$\frac{1}{[A]} = kt + \frac{1}{[A_o]} \qquad \text{(Second – order)} \quad \text{--------- (Eq. 13)}$$

where A = the concentration of a reactant at a time t during the reaction, A_o = the initial reactant concentration at the onset of reaction, and k = the rate constant or slope of the integrated rate equation.

The substitution of the concentration terms with the current I in the integrated first- and second- order rate equations would modify them into the corollary expressions, eqns. 14 and 15;

$$\ln[I] = -kt + \ln[I_o] \qquad \text{(For first – order)} \quad \text{--------- (Eq. 14)}$$

$$\frac{1}{[I]} = kt + \frac{1}{[I_o]} \qquad \text{(For second – order)} \quad \text{--------- (Eq. 15)}$$

where I = the current at a time t during the reaction, I_o = initial current at the onset of reaction, and k = the rate constant or slope of the integrated rate equation.

The kinetic analysis of experimental data has been explained in a number studies and reported, where a characteristic property of reactant (that is dependent on its concentration) is monitored as function of time during the reaction.[94,95,97] In the this case (where the reaction of the electrophilic diazonium cation is monitored via chronoamperometry), the graph of ln [Currents] versus time would be expected to give a linear plot with negative slope in first-order kinetics; whereas in the second-order kinetics test, a plot of 1/[Current] (or the inverse of current) as a function of

time would be expected to produce a linear plot with a positive gradient, as shown by the “dummy” lines in the six combined charts in Figure 26.

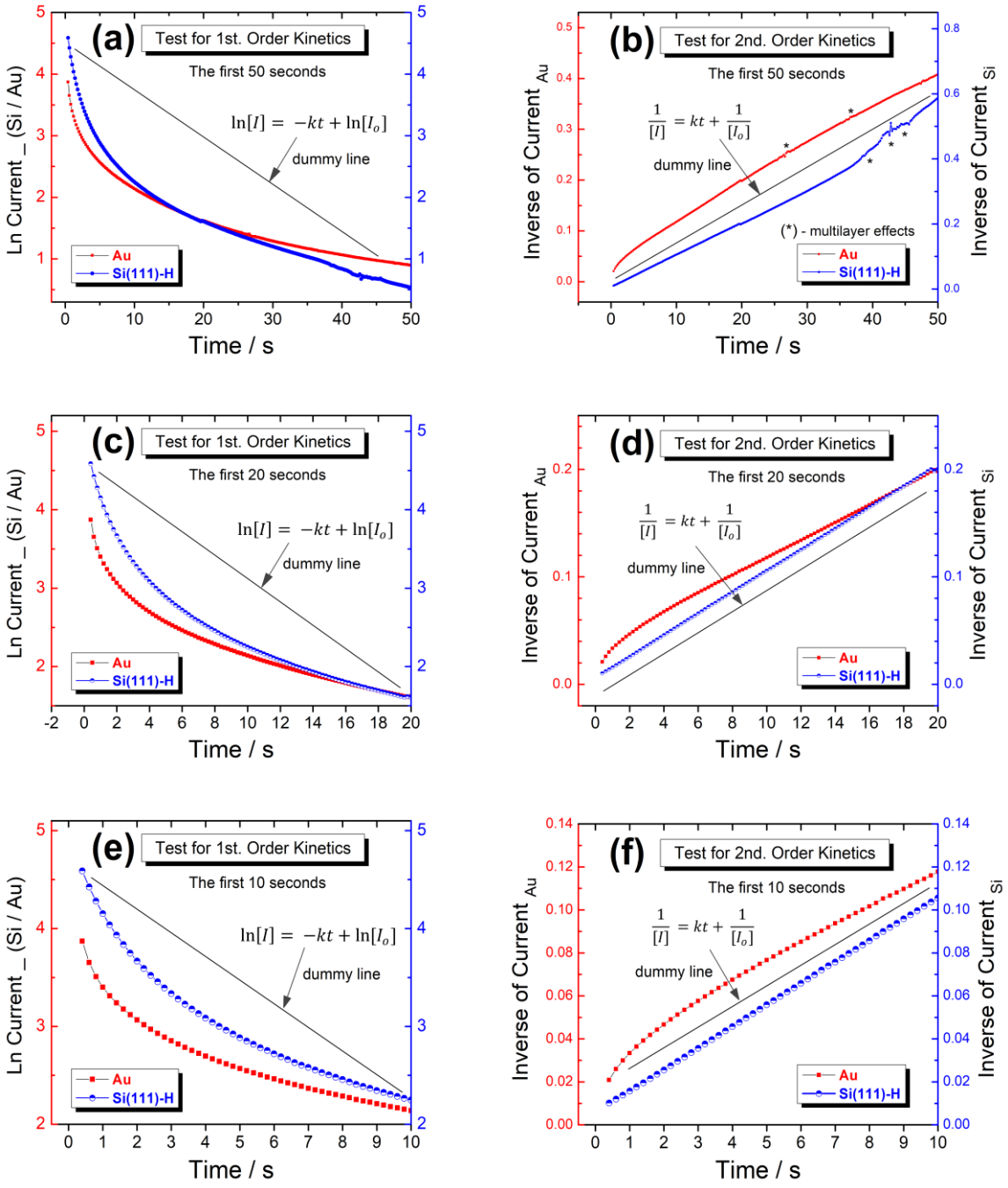

Figure 26: Kinetic analysis of the experimental CA data from the electroreduction of 4-CMTBD on Si(111)-H and Au surfaces.

Figures 26a, 26c, and 26e shows the graphical tests for first-order kinetics for the electroreduction 4-CMTBD within the first 50 s, 20 s, and 10 s respectively, while

Figures 40b, 40d and 40f show the corresponding second-order kinetics tests. The analysis is based on the CA experimental data derived from Figures 20b and 21b. The straight lines or “dummy lines” representing the relevant integrated first- or second- order rate equations are indicated in each of the test graphs for cursory comparisons. The graphs in Figures 26a, 26c, and 26e (the tests for first-order kinetics), show pronounced deviations with respect to the “first- order dummy lines”. However, in the tests in Figures 26b, 26d, and 26f (for second-order kinetics), show relatively smaller deviations with respect to the second-order rate equation. The deviations marked using asterisks (*) in Figure 26b appearing from about 35 - 50 s in the kinetic data provides an indication that the products (grafted multilayers) begin to affect the rate and they are referred to as “multilayer effects” in this case. This also suggests that the active surface sites are occupied fairly in the early parts of the reaction, which happens within the first 30 s in this case.

The inert electrolyte comprising the solvent and the conducting salt are generally present at much higher concentrations than the reactants (the diazonium salts in this case), therefore they are assumed to have minimal contributions to the rate of diazonium electroreduction next to electrode surface throughout the course of the reaction. It can be concluded from the analysis of the kinetic graphs in Figure 26 that rate of decay in current accompanying the early stages of the electroreduction of 4-CMTBD on Si(111)-H and Au surfaces simulate the integrated second-order kinetic rate equation. In Figure 26f, the of the kinetic plot for the electroreduction on Au surface shows a pronounced curvature within the first 3 s as opposed to a linear plot in the case on Si(111)-H surface, however after the 3rd s, the electroreduction on both Si and Au surface proceed at fairly similar rates till about the 20th s as shown

also in Figure 26d. This suggests that the electroreduction of 4-CMTBD seems to begin with a slightly higher rate constant on Au surface than on the Si(111) surface.

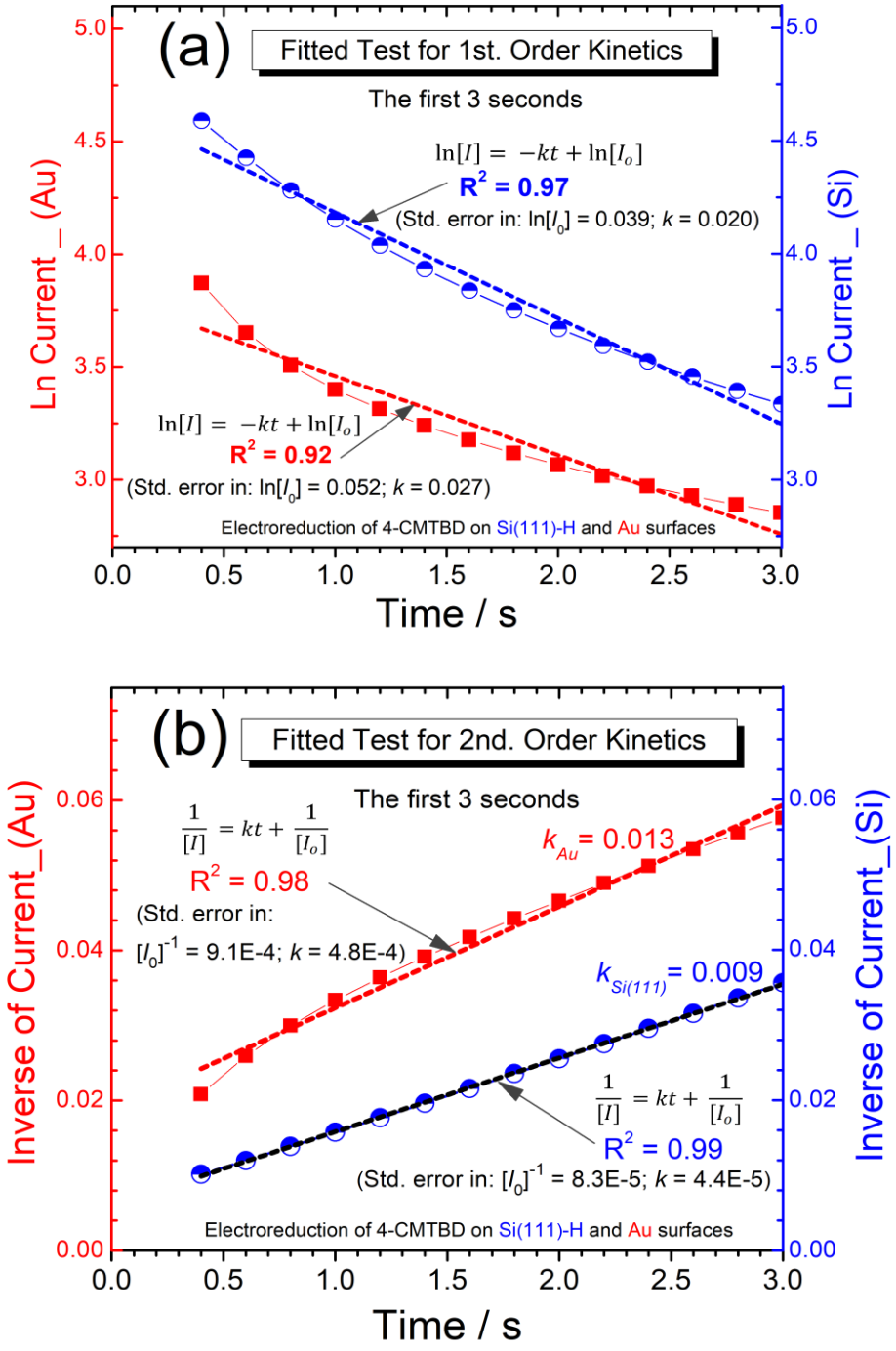

Figure 27: The fitted analysis of the (a) first- and (b) second- order kinetics for the first three seconds of the electroreduction of 4-CMTBD on Si(111)-H and Au surfaces.

Figures 27(a) and 27(b) shows the fitted kinetic analysis for the first- and second-order integrated rate equations respectively. The experimental values are fitted using

the line regression model. The values of the coefficient of determination, R^2 are higher in the test for second-order kinetics (Figure 27b) compared to the values obtained in the first-order test (Figure 27a). In addition, the standard errors in the intercepts and slope arising from the regression fit in the case on first-order test are greater than the corresponding standard errors in the case on second-order test. In the case of electrografting on Si(111)-H surface as depicted in Figure 27b, the experimental CA data fits very well with the integrated second-order rate equation. Figure 27b also reveals that the rate of electroreduction of 4-CMTBD is about 1.5 times greater on Au surface than on the Si(111)-H surface within the first 3 seconds based on rate constants.

Chronoamperometric data has previously been useful in estimating the kinetic parameters for a number of electron-transfer reactions including cases where the diffusion coefficients and effective electrode surface area unknown.[98,99,100] In this case, the rate of conversion of 4-CMTBD to the 4-CMTB units show a dependence on the current flow (generated by electron transfer process) during the electroreduction time. The kinetic analysis (in Figures 26d, 26f, 27a, and 27b) of the rate of current decay shows a correlation with the integrated second-order rate equation. It can therefore be proposed that the rate of electroreduction of 4-CMTBD that leads to the electrografting of 4-CMTB molecules on both Au and Si surfaces, in the early stages (0 ~ 30 s) obey the differential rate law in equation 16:

$$Rate = -\frac{d[(4\text{–CMTBD})]}{dt} = k[(4-\text{CMTBD})]^2 \quad \text{------ (Eq. 16)}$$

where d[(4-CMTBD)]/dt = the rate of electroreduction of 4-CMTBD over time, k = the rate constant, and [(4-CMTBD)] = the concentration of the aryl diazonium cation – 4-

CMTBD. Equation 16 means that the order of the reaction with respect to [(4-CMTBD)] is two.[97]

3.2.5 Raman Spectroscopy: Chelate Complex Formation (Cu and Pb binding)

Raman backscattering spectroscopy was used here to ascertain heavy metal binding to the CMT ligand groups on the chelate-functionalized Si(111) surfaces since IRSE was not able to detect lower vibrations (< 700 cm^{-1}). Both the Si-(4-CMTB)-Cu and Si-(4-CMTB)-Pb surfaces, whose preparations are described under section 2.7, were investigated for the existence of Cu-S, Cu-O, Pb-S, and Pb-O Raman bands as proof of the heavy metal binding.

Figure 28 shows the Raman spectra, in the region between 245 – 275 cm^{-1}, obtained from the surfaces of Si−(4-CMTB) (blue line), Si−(4-CMTB)−Pb (black line), and Si−(4-CMTB)−Cu (red line). This particular spectral region shows a signal at about 250 cm^{-1} related to the Pb-S,[101] on the Si-(4-CMTB)-Pb surface and at ~ 266 cm^{-1} assigned to the Cu-S vibration,[102,103,104] on the Si-(4-CMTB)-Cu surface.

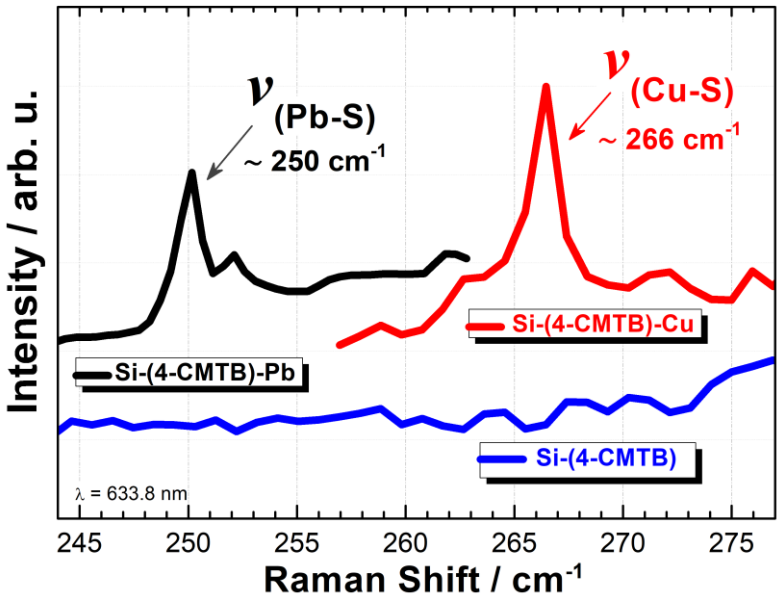

Figure 28: Raman spectra highlighting the Pb-S and Cu-S bonds on Si-(4-CMTB)-Pb and Si-(4-CMTB)-Cu surfaces respectively.

Figure 29 shows the reference Raman fingerprint spectra obtained from the hydrated $CuCl_2$ and hydrated $Pb(NO_3)_2$, which are the hydrated heavy metal salts used in the chelate complexation reactions on the respective modified surfaces. They provide critical spectral information to help decipher the formation on the new metal – chelate bonds when they are cross referenced against the spectra of Si-(4-CMTB)-Cu and Si-(4-CMTB)-Pb surfaces. The grey downward arrows mark the positions and values denoted by asterisks (*), where the signals related to Cu-S, Pb-S, Cu-O, and Pb-O bonds appeared from the experiments. These metal-ligand Raman vibration values as extracted from the spectra of Si-(4-CMTB)-Cu and Si-(4-CMTB)-Pb surfaces and presented in previous Figure 28 (for Pb-S, Cu-S), and the later Figures 30 (for Cu-O) & 31 (for Pb-O).

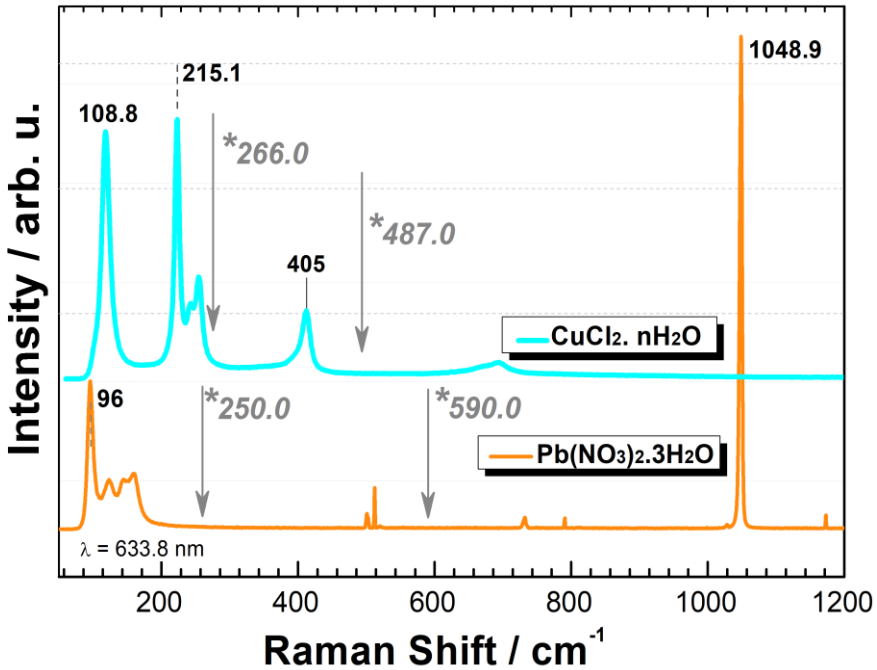

Figure 29: Raman backscattering spectra of the hydrated salts of: $Pb(NO_3)_2$ (orange line) and $CuCl_2$ (light blue).

Figure 30 highlights a section of the Raman spectra that reveals the characteristic sharp signal at ~ 487 cm^{-1} on the Si-(4-CMTB)-Cu surface which is ascribed to the Cu-O stretching vibration.[102,105,106] It can be observed that the Raman spectra of the

hydrated $CuCl_2$ salt (in light blue), the Si-(4-CMTB) surface (in blue), and the Si-H surface (in dashed violet) show no vibrational bands within the same spectral region.

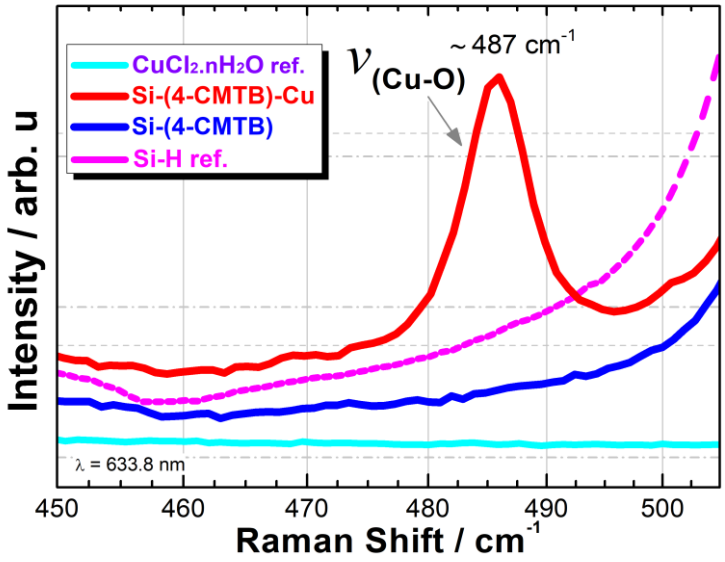

Figure 30: Raman spectra highlighting the Cu-O bonds in the Si-(4-CMTB)-Cu surface.

The Cu-O Raman band shown in Figure 30 appears in the same Si-(4-CMTB)-Cu spectrum that also reveals the presence of the Cu-S signal, which is illustrated the earlier Figure 28. The simultaneous occurrence of both Cu-S and Cu-O bonds in the same Raman spectrum provides evidence of polydentate chelation of Cu on the Si-(4-CMTB)-Cu surface as sketched earlier in Figure 19.

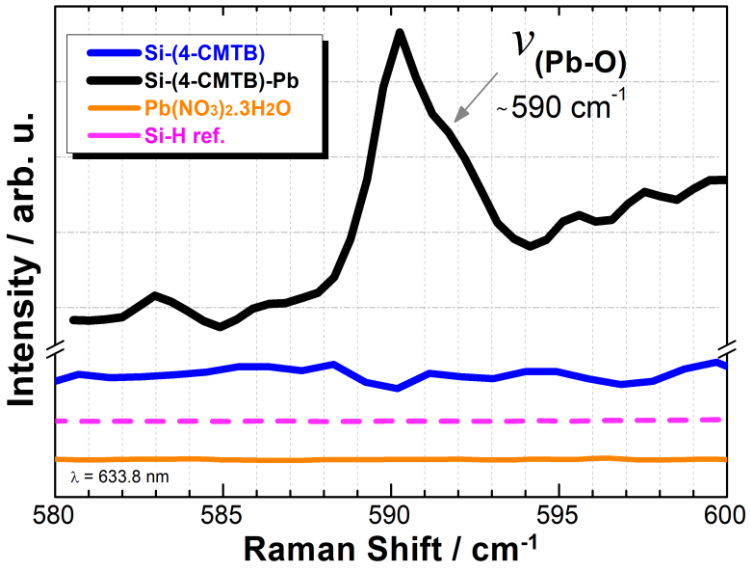

Figure 31: Raman spectra: Evidence of Pb-O bonds on the Si-(4-CMTB)-Pb surface.

Figure 31 illustrates the Raman spectral region of the Si-(4-CMTB)-Pb surface that reveals the characteristic vibrational band ascribed to the Pb-O stretching vibrations at about 590 cm^{-1}.[107,108] It is also evident that the spectra of the hydrated $Pb(NO_3)_2$ salt, Si-(4-CMTB) surface, and Si-H surface show no Raman vibrational bands in the spectral region associated with the Pb-O bond. Both the Pb-O related signal (Figure 31) and the Pb-S Raman signal ~ 250 cm^{-1} (Figure 29), occur within the same Si-(4-CMTB)-Pb spectrum. This attests as to the existence of multidentate chelation/binding of Pb by the CMT ligands (via S and O donor atoms) on the Si-(4-CMTB)-Pb surface.

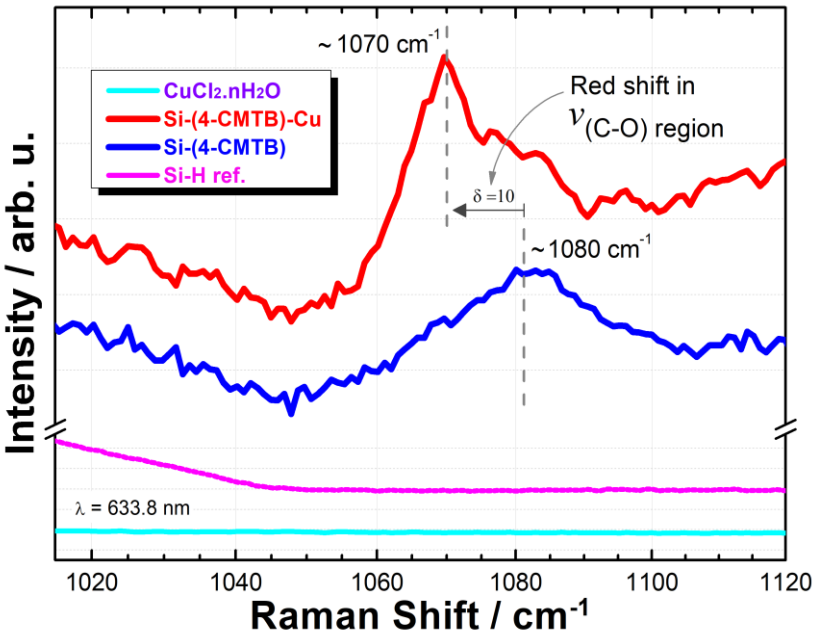

Figure 32: Evidence of red-shift upon Cu – chelation on the Si-(4-CMTB) surface.

Figure 32 shows a comparison between the spectra of the Si-(4-CMTB)-Cu surface (red line) and the initial Si-(4-CMTB) surface (blue line) which illustrates the conspicuous red/bathochromic shift observed as a result of Cu chelation. The spectra of the hydrated $CuCl_2$ salt and Si-H surface show no Raman signals in this spectral regime (see light blue and violet lines). The characteristic C-O bond vibration occurs in the spectral region between 1040 − 1120 cm^{-1}.[84] The vibrational

band in this region appears slightly shifted to lower wavenumbers (by about 10 cm^{-1}) upon Cu binding on the Si-(4-CMTB) surface. However, a shoulder peak is still visible around 1080 cm^{-1} providing a hint that not all the CMT ligands on the surface participate in the chelation of Cu. The delocalization of electron density from the oxygen donor atoms of the carboxylate ligand groups into the valence orbitals of the Cu, leading to the formation of Cu−O coordinate bonds, is a major factor that would possibly weaken the C−O bonds, hence causing the observed red shift in the region associated with the C−O signals. This red-shift as illustrated in Figure 32 characterizes the involvement of carboxylate groups in the chelation or covalent binding of Cu on the Si-(4-CMTB) surface.

However, no appreciable red-shift was observed in the case of Pb binding on CMT chelating ligands. Copper (II) is one of the transition metal ions that is often known to be capable of binding strongly with high formation constants to ligands. It also possess a relatively high polarizing power towards ligands and has a peculiar tendency undergo Jahn-Teller distortions in its organo-complexes to acquire extra stability.[109] Lead is a non-transition element unlike Cu (which would involve d-orbitals in coordinate binding); moreover, the number of electrons in its valence shell is closer to that of the next noble gas configuration in the same period than in the case of Cu. These are perhaps important factors that would explain the disparity in regards to presence and absence of the red-shift in their organometallic complexes as observed in this work.

A summary of the experimentally determined Raman bands due to the (Cu/Pb)–(O/S) bonds (from Figures 28, 30 and 31) are reported in table 1. These vibrational bands are all absent the Raman reference spectra of the respective hydrated metal

salts (Figure 30), which confirms the formation of the metal – ligand bonds on the Si-(4-CMTB) surface upon treatment with the Pb- and Cu- ion solutions. It can be noted from this work that the S-(Cu/Pb) coordinate bonds are relatively weaker compared to the O-(Cu/Pb) bonds. Some studies have shown that the Pb-S bond length is approximately 2.64 Å, while that of Pb-O is approximately 2.45 Å in typical chelate environments.[110]

Table 1: The Raman signals related to the metal-ligand bonds on the Si-(4-CMTB) surface.

CMT ligand – Metal bonds on the Si-(4-CMTB) surface	Raman bands / cm^{-1} and intensity	Spectral range of the Raman signals in the spectrum / cm^{-1}
Cu-S	266 (w.sh.)	260 – 275
Pb-S	250 (w.sh.)	246 – 255
Cu-O	487 (s.sh.)	470 – 498
Pb-O	590 (s.sh.)	586 – 595

*N/B: w. – weak, sh. – sharp, s. – strong.

The (C=C) bonds in the benzene ring are only about 1.2 Å long, which is about half the length of Pb-(O/S) bonds (2.45 / 2.64 Å). Considering the Pb-(O/S) bond lengths from literature and the Si(111)-H surface structure a theoretical rationalization from a molecular level would permit the possibility of electrografting two CMTB units on adjacent Si atoms (formally of Si-H origins) and the binding of Pb atoms by the CMT chelate groups with minimal steric hindrance can be rationalized to exist. Moreover, Pb has a higher atomic radii compared to Cu and so a similar theoretical rationalization may hold in the case of Cu-chelation. However, further the crystallographic data obtained from X-ray diffraction (XRD) technique in future may help to better elucidate the actual molecular structure of the nanocrystals formed.

3.2.6 X-ray Spectroscopy: Characterization of the Modified Surfaces and Cu Uptake

Figure 33 shows the X-ray photoelectron spectra of the Si−(4-CMTB)−Cu, Si−(4-CMTB), and Si-H surfaces in the region between 0 – 320 eV. The Si2p and Si2s signals at 100 and 151 eV, respectively, are present in the survey spectra of the three surfaces, although they appear lower in intensity in the case of the modified surfaces, Si−(4-CMTB) and Si−(4-CMTB)−Cu. This is due signal attenuation caused by the electrodeposited overlayer material (containing 4-CMTB units) and formation of organometallic structures on the Si substrate (in the case of Si-(4-CMTB)-Cu surface). The presence of S atoms of the CMT groups is also ascertained by the signals: S2s at 228 eV and S2p at 164 eV observed in the spectra of Si-(4-CMTB) and Si-(4-CMTB)-Cu surfaces.

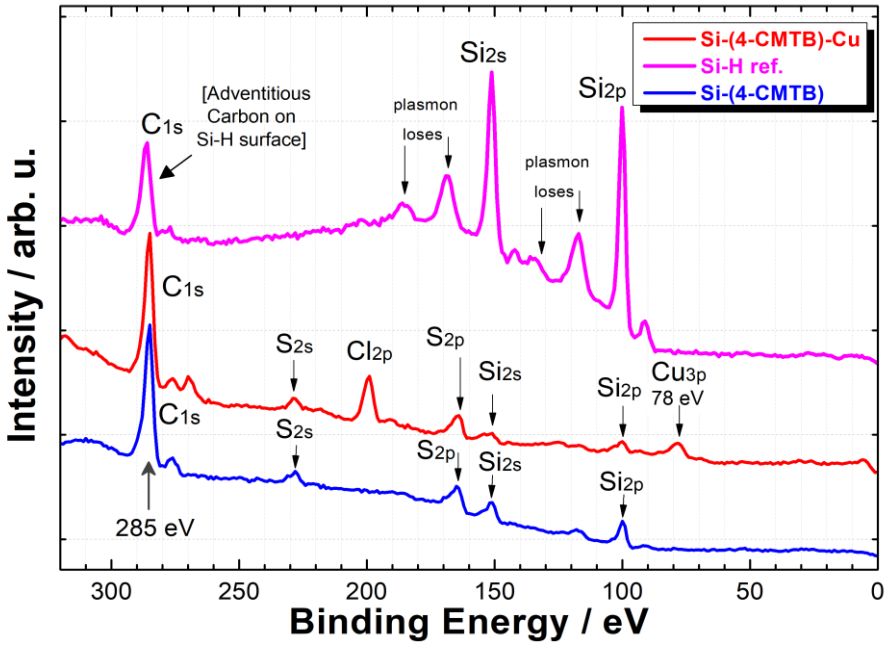

Figure 33: XPS survey spectra of Si-(4-CMTB)-Cu, Si-H, and Si-(4-CMTB) surfaces.

The C1s signal (at 285 eV) in the modified surfaces, Si−(4-CMTB) and Si−(4-CMTB)−Cu are similar in terms of intensity. They are more intense than the Si2p and

Si2s signals in the two respective spectra. However, the Si−H bare surface reference spectrum reveals a C1s peak that is less intense than Si2p and Si2s signals (with the same spectrum). This C1s signal is caused by the adventitious carbon atoms, which originate from the exposure to air and substrate solution processing before the measurement. The two extra intense C1s signals on the modified surfaces which coexist with both the S2s and Si2p signals in the XPS overview survey spectra qualitatively characterizes the existence of grafted organic layers containing 4-CMTB units on the Si(111) surface. The spectrum of the Si-(4-CMTB)-Cu surface in Figure 33 also shows evidence of Cu by the characteristic Cu3p signal at 78 eV.

Figure 34a shows the Cu2p spectrum obtained from Si-(4-CMTB)-Cu surface, which reveals the $Cu2p_{1/2}$ at about 955 eV and the $Cu2p_{3/2}$ at about 935 eV.[83] The signal contains typical shake-up satellites at about 943 and 963 eV, which are known to characterize the (+2) oxidation state of the Cu.[111] The shape of the satellite peaks closely resembles that of Cu^{2+} species partly coordinated to acetate ligands. This suggests the existence of the Cu(II) species chelated by carboxylate ligands.[112]

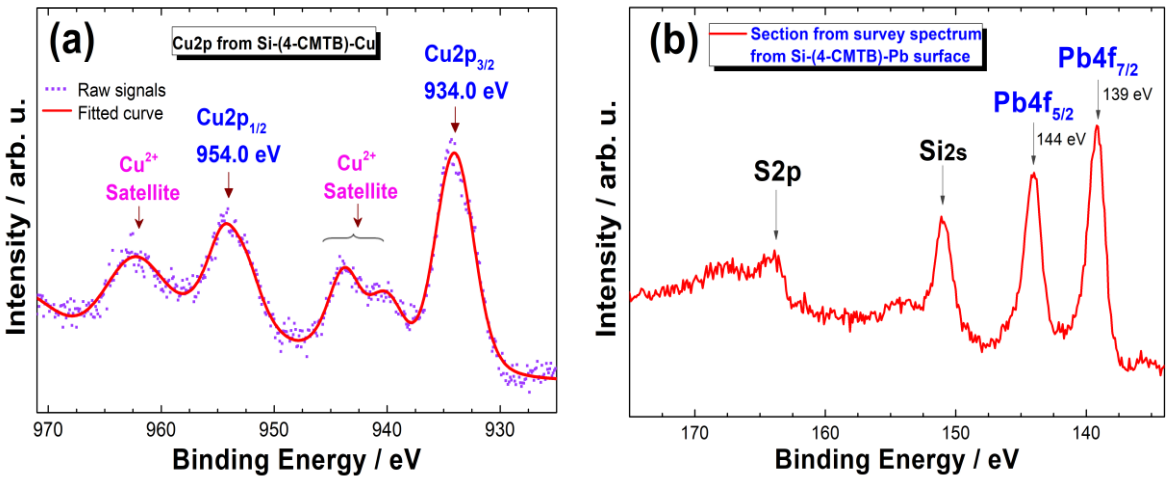

Figure 34: XPS spectra of (a) Cu2p signals from the Si-(4-CMTB)-Cu surface and (b) Pb4f signals from the Si-(4-CMTB)-Pb surface.

Figure 34b shows a section of the survey region highlighting the S2p, Si2s and Pb4f XPS signals. The characteristic $Pb4f_{7/2}$ and $Pb4f_{5/2}$ doublet signals occur at 139 eV and 144 eV respectively with a peak separation of about 5 eV.[83] The observed Si2s and the S2p signals along with the Pb XPS signals provide qualitative evidence as to the existence of the Si substrate, the CMT group and Pb on the surface.

Figure 35 shows the intensity attenuation of the XPS Si2p signals from the surfaces of: Si−H, Si−(4-CMTB), and Si−(4-CMTB)−Cu, as investigated further under similar measurement conditions. The intensity of photoelectron, I_o, emitted at a certain depth - “d” or “x” below the surface under probe, is known to attenuate across the overlayer material to a new intensity, I, in accordance with the Beer−Lambert decay eq. 10 (section 2.5).[79] This implies that thicker or more densely packed overlayer material on top of a surface would cause an increase in signal attenuation by altering the sampling depth hence decreasing the signal intensity.

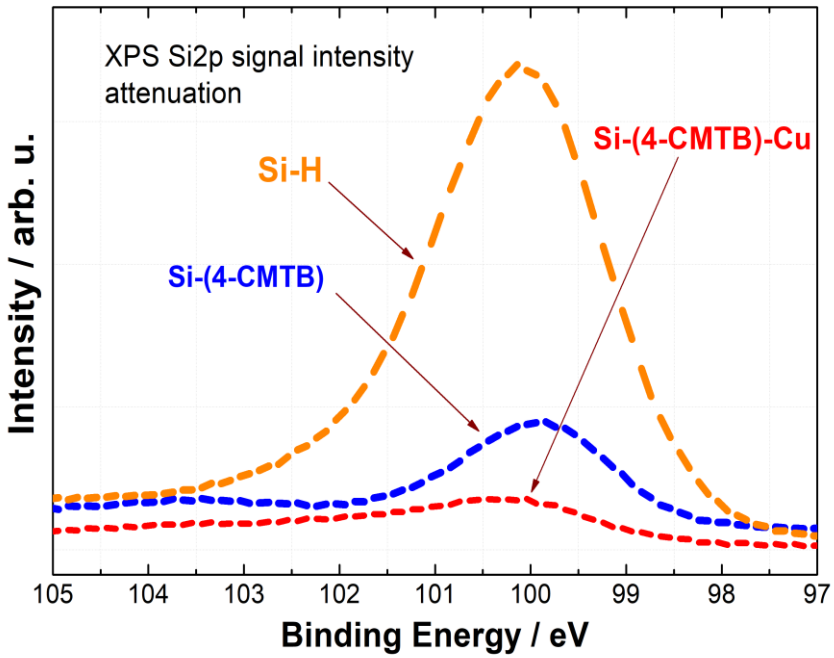

Figure 35: XPS Si2p signal attenuation among the surfaces of Si-H (in orange), Si-(4-CMTB) (in blue) and Si-(4-CMTB)-Cu (in red).

Figure 36 shows the plot and the calculation used in the estimation of the thickness of the electrografted 4-CMTB units on of the Si(111) surface. It also provides evidence of Cu uptake on the Si-(4-CMTB)-Cu surface. The Si−H surface records the highest peak intensity relative to the two modified surfaces, Si-(4-CMTB) and Si-(4-CMTB)-Cu. This is because it experiences the highest sampling depth due to the lack of the overlayer material with respect to the modified surfaces. The modified surface Si−(4-CMTB) shows a lower intensity than that of the Si−H surface due to the attenuation caused by the organic overlayer containing the grafted 4-CMTB units. The thickness of the grafted 4-CMTB units on the Si(111) substrate surface was estimated to be about 3.08 nm. The estimation multilayer structure of organic thin film attached on the Si(111) surface, which is known to arise from the free radical mechanism via the aryl diazonium electrografting route.[35,90]

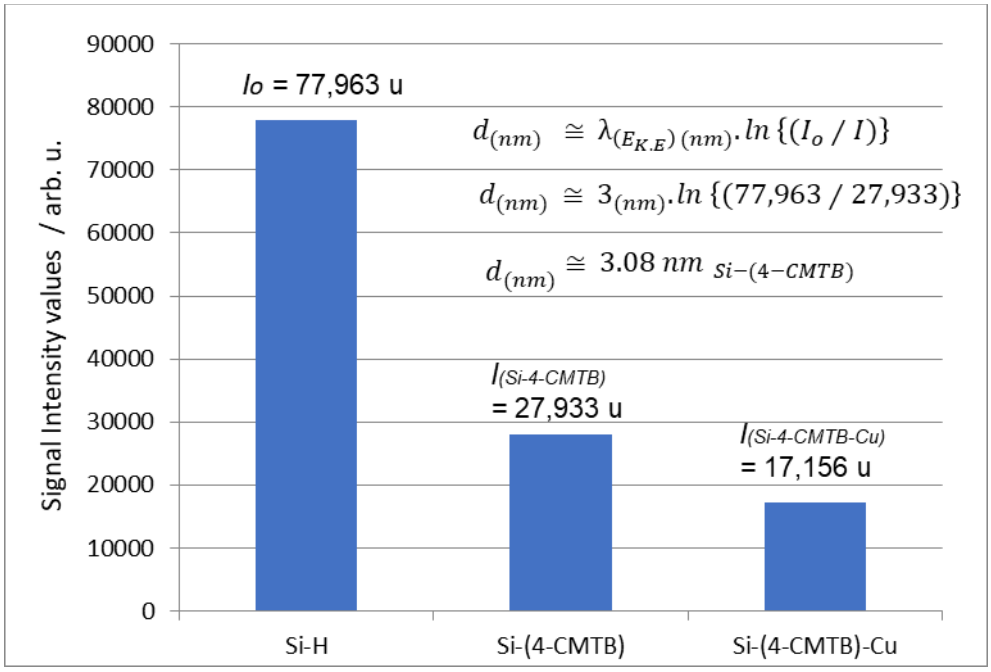

Figure 36: A histogram plot of the Si2p signal intensity values of: Si-H, Si-(4-CMTB) and Si-(4-CMTB)-Cu surfaces.

The estimated thickness of the overlayer material on Si-(4-CMTB)-Cu surface was about 4.50 nm, representing an increase of about 1.48 nm (implying further increase in signal attenuation) with respect to the Si-(4-CMTB) surface. This characterizes the uptake or “packing” of Cu via chelation mechanisms. The further reduction in signal attenuation upon Cu treatment is due to the formation of the organo-Cu complex structures (based on the observed Cu-S and Cu-O in the Raman spectra) on the chelate-modified surface. This possibly leads to a “swelling effect” partly contributed by the enhanced density of the overlayer material due to the new metal-ligand bonds formed on the modified surface.

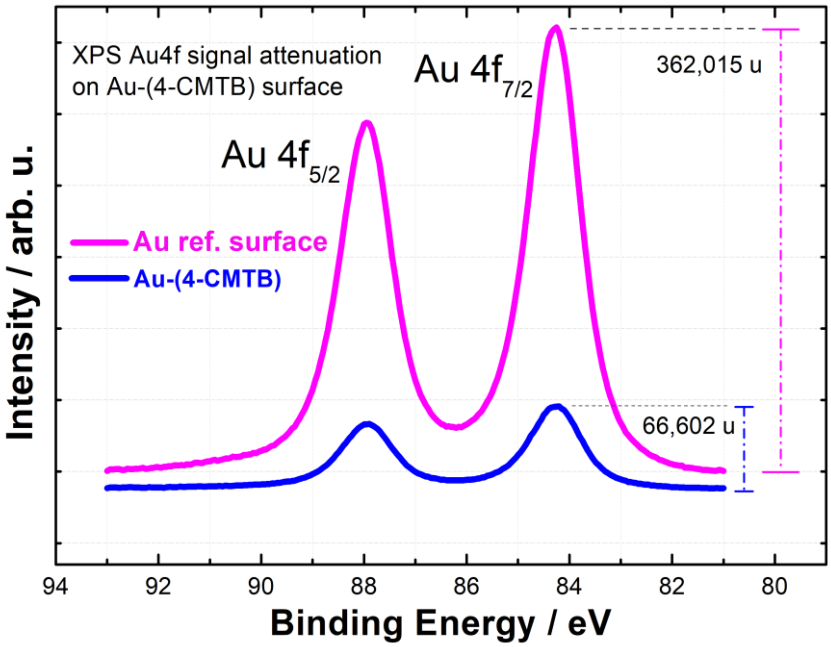

Figure 37: XPS Au 4f signals from the surfaces of Au-(4-CMTB) (in blue) and clean Au reference (in magenta).

Figure 37 shows the XPS Au 4f doublet signals ($Au4f_{5/2}$ and $Au4f_{7/2}$) from a clean Au reference substrate surface (in magenta) and the other sample containing electrografted 4-CMTB (in blue). The intensity of the Au4f signal attenuates upon surface electrografting on Au substrate surface. The signal attenuation observed here upon Au functionalization has also has also been reported in previous studies.[72]

Table 2: Summary of the approximate thickness estimates from 4-CMTB grafting.

Si-(4-CMTB)	Au-(4-CMTB)	Si-(4-CMTB)-Cu
3.08 nm	3.40 nm	4.50 nm

Table 2 shows a summary of the estimated overlayer thicknesses on the modified Si(111) and Au surfaces. It reveals that nanoscale layers are realized from the electrodeposition of 4-CMTB on both Au and Si(111) surface. The estimated thickness of the 4-CMTB units grafted on Au surface is about 3.40 nm, which also provides evidence of a multilayer thin film structure on the Au-(4-CMTB) surface.

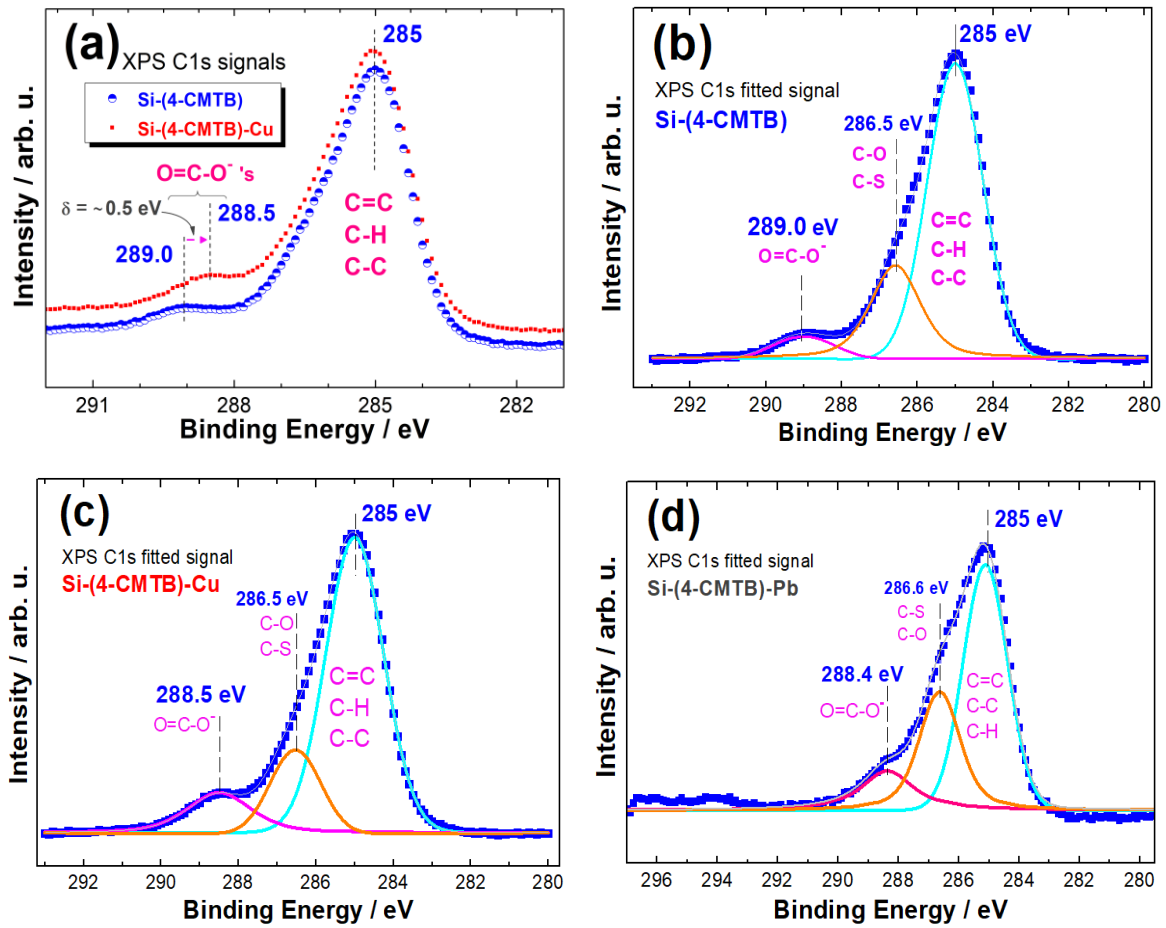

Figure 38: XPS C1s signals from the Si-(4-CMTB), Si-(4-CMTB)-Cu, and Si-(4-CMTB)-Pb surfaces.

Figure 38 shows the detailed XPS spectra of the C1s signals obtained from the Si−(4-CMTB), Si−(4-CMTB)−Cu, and Si−(4-CMTB)−Pb surfaces. The fitted C1s signals are illustrated in Figures 38b, 38c, and 38d and labeled accordingly. The presence of carboxylate groups (O=C-O⁻'s), which typically occurs in the region ~ 290.0 − 288.5 eV [83] within the C1s XPS signal was observed in the C1s signals of all the modified surfaces. The presence of O=C-O- groups (as in -COOH) on the modified surfaces, as validated in the XPS spectra, provides a hint that the CMT chelating groups remain undegraded upon the cathodic electrografting procedure. This is further supported by the existence of the characteristic C=O vibrations observed in the IRSE spectra of the Si-(4-CMTB) surface (in section 3.2.3). Figure 38b shows the fitted C1s signal of the non-HMI treated Si-(4-CMTB) surface. The C1s signal related to the (COO-) group at about 289 eV notably shifts to lower binding energies by ~ 0.5 eV in the case on Si-(4-CMTB)-Cu (Figures 38a, 34c) and ~ 0.6 eV in the case of Si-(4-CMTB)-Pb surface (Figure 38d). The shifts are a sign of changes in chemical environment the C1s of the COO- groups upon interacting with the HMI's. One factor that would explain this phenomenon is the distortion of the electron cloud or density around the C atom of the COO- group, which is brought about by the involvement of the adjacent O atoms in the formation metal coordinate bonds upon chelation of Cu/Pb on the surfaces. This means that the COO- groups are no longer free since the previously non-bonded electrons take part in metal binding. The formation of coordinate O-(Cu/Pb) bonds proceeds via delocalization of electron densities from donor atoms into the metal valence shells. As the metal cations attract electron densities from the oxygen donor atoms of the COO- groups to form coordinate bonds and chelate rings, the electron cloud of the ligand is altered in a way that changes the chemical environment of the C1s of COO- groups.

Moreover, the Cu/Pb atoms also possess a highly positively charged nucleus that possibly offers extra attraction to the C1s electrons (of COO- groups) upon binding. This would possibly cause the new characteristic C1s signal of the Cu/Pb bound COO- groups) to be detected at relatively lower binding energies due to the external influence brought about by the nuclear attraction force of the neighboring coordinated/chelated heavy metal.

3.3 Surface Modification with Piperazinyl (PPz) Chelate

The selectivity of PPz groups in binding of Cu ions has previously been exploited in spectrophotometric studies.[113] This was the motivation behind the fabrication of a PPz modified surface that is potentially selective towards Cu ions. The electrografting of Cu selective chelating agent onto the Si(111) surface, as investigated in this section, could therefore extend efforts towards developing viable functionalized surfaces that may exhibit good selectivity for Cu ions. Such devices may also augment environmental protection strategies such as in the development of new miniaturized bio-electronic sampling kits for monitoring industrial effluent Cu contamination.

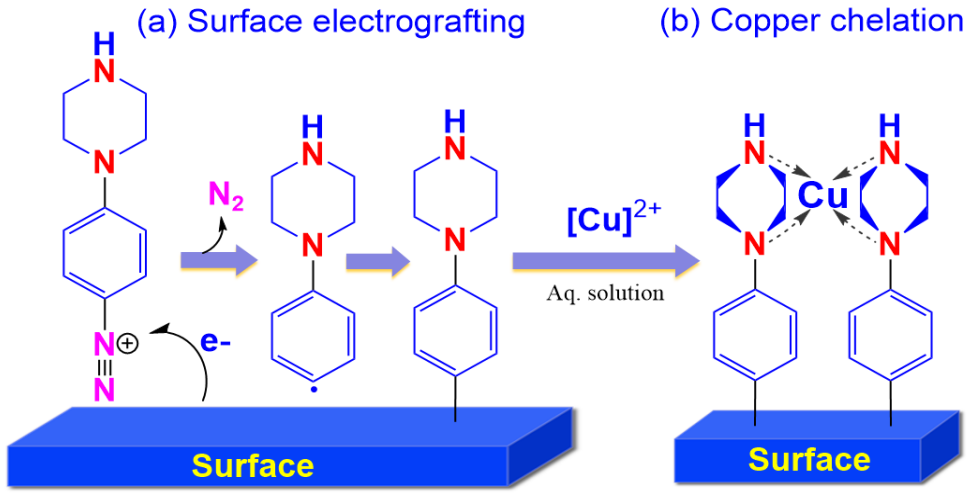

Figure 39: Idealized surface functionalization with PPz groups for Cu chelation.

This section describes a functionalization approach for introducing the PPz chelating ligands on H-terminated Si surface Si(111)-H via the direct electrografting of the 4-(Piperazinyl)benzenediazonium cation 4-PPzBD (Figure 39). A graphical determination of the kinetics of electroreduction of 4-PPzBD on Si(111)-H and Au surfaces based on the rate of decay in currents derived from the chronoamperometric measurements is discussed. In addition, the *in-situ* mass electrodeposition of 4-PPzBD on Au surface is also investigated via the EQCM

electrografting technique. The uptake and binding of Cu on the modified Si(111) surface Si-(4-PPzB) is also characterized by X-ray and Raman spectroscopic techniques.

3.3.1 Electroreduction of 4-(Piperazinyl)benzenediazonium cation [4-PPzBD]

The CV's and their corresponding CA curves of the electroreduction of 4-PPzBD on Si(111)-H and Au surfaces are shown in Figures 40 and 41 respectively. Figures 40a and 41a reveal the characteristic first broad cathodic reduction peaks due to the electroreduction of 4-PPzBD on Si(111)-H and Au surfaces respectively. The rapid electroreduction of the 4-PPzBD diazonium cations lead to formation of electrografted 4-PPzB units on the surfaces. The reduction of 4-PPzBD on Si(111)-H surface begins at an onset potential of about -0.30 V and approaches a cathodic peak voltage at about -1.0 V (Figure 40a). The reduction of 4-PPzBD on Au surface occurs from about +0.30 V to about -0.6 V within the first cathodic scan (Figure 41a). The first cathodic CV curve for the corresponding "Blank" solutions (which contains no 4-PPzBD salt), as indicated in CV graphs, show no characteristic broad reduction waves within the cathodic electrografting potential windows (Figure 40a and 41a).

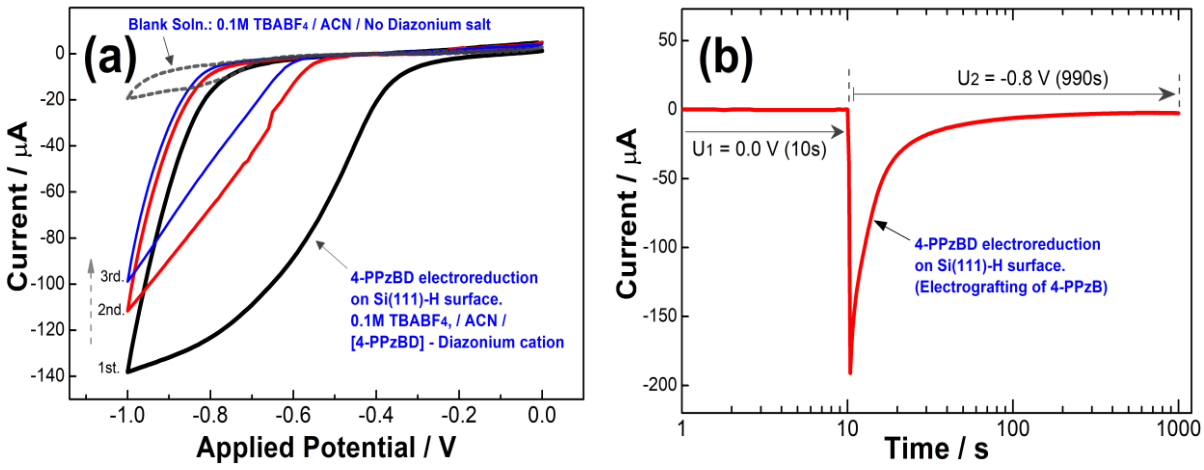

Figure 40: (a) CV and (b) CA for the electroreduction of 10 mM 4-PPzBD on Si(111)-H surface.

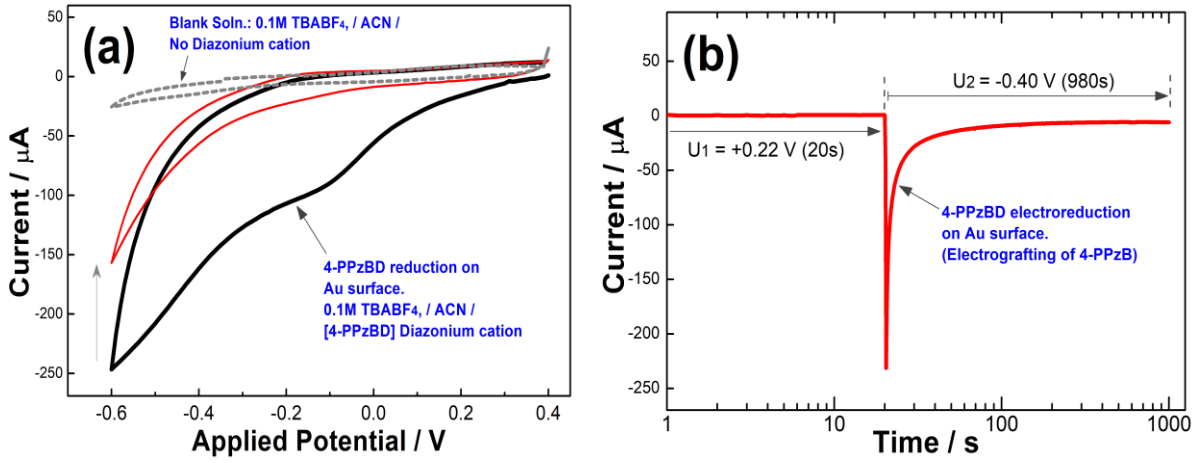

Figure 41: (a) CV and (b) CA for the electroreduction of 10 mM 4-PPzBD on Au surface.

The “Blank” CV’s serve as controls which further confirms that the observed broad cathodic waves in the corresponding non-“Blank” CV’s are related to the electroreduction of 4-PPzBD molecules responsible for the electrografting of 4-PPzB on the respective surfaces. In addition, the disappearances of the typical broad cathodic waves in the second and subsequent cathodic CV scans indicate the blocking of the charge transfers due to the electrografted of 4-PPzB groups on the Si(111) and Au surfaces.

Figures 40b and 41b show the respective CA graphs that reveal the steep decays in currents that accompany the electroreduction of 4-PPzBD on Si(111)-H and Au surfaces respectively. The applied fixed voltages in the CA experiments are selected based on the erstwhile recorded corresponding CV graphs. In typical CA investigations, fixed “non-reduction” and “reduction” voltages are applied over time on the electrode surface to monitor current response. The drop or decay in currents observed over time at the selected “reduction” voltages in both the CA graphs represents the 4-PPzBD electroreduction reaction coordinate as a function of charge transfer. The characteristic sharp decay in currents observed denote the rapid

conversion of 4-PPzBD molecules that leads to formation of the surface bound (or electrografted) 4-PPzB units.

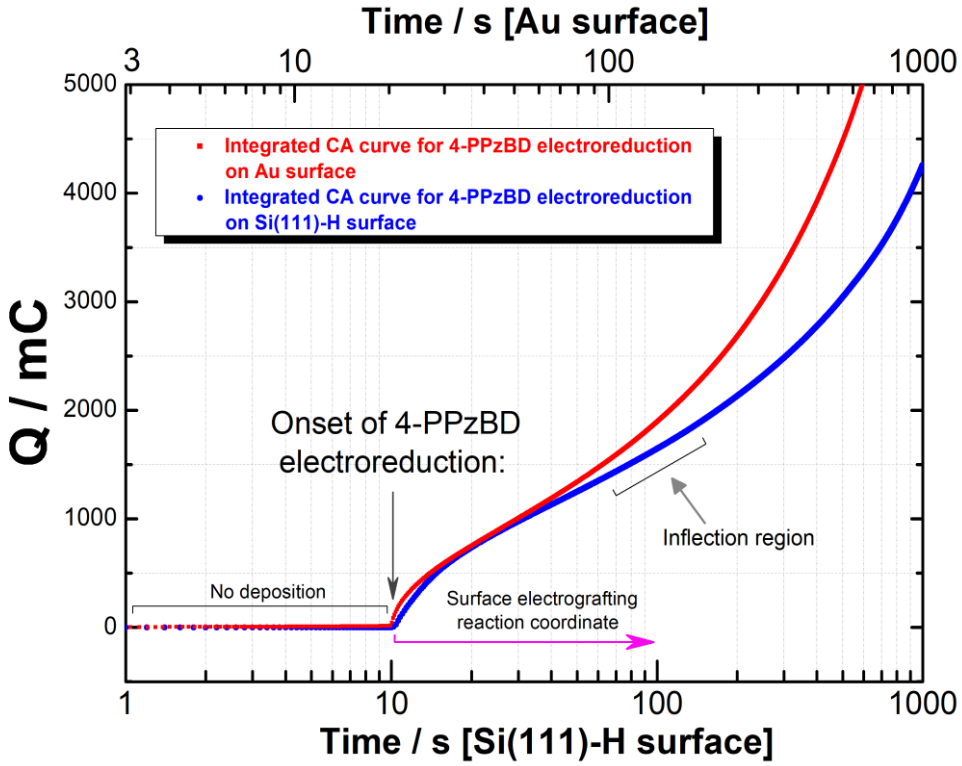

Figure 42: Charge flow (Q) obtained from the integrated CA graphs for the electroreduction of 4-PPzBD on Si(111)-H and Au surfaces.

Figure 42 shows the charge flow as a function of time as derived from the integrated CA graphs arising from the electrografting of 4-PPzBD on Si(111) and Au surfaces. The two curves look fairly similar in terms of curvature/shape, and they characterize the electroreduction of 4-PPzBD on the respective electrode surfaces as function of time. They also give a more detailed picture of the surface electrografting reactions in terms of the charge transfer at the electrode surface than the traditional CA graphs. In both the Si(111)-H and Au electrografting reactions, there is an initial sharp rise in charge from the onset of the reactions, which arises from the initiated 4-PPzBD electroreduction reaction. However, the charge begins to decay rapidly (due to initial surface modification) as it approaches an inflection or a turning point, from

which the charge unusually rises up again exponentially. The notable exponential rise in the Q(t) plot after the inflection point (indicated on the graph), is a unique feature of the 4-PPzBD electroreduction that distinguishes it from the electrografting behavior of 4-CMTBD shown earlier in Figure 22. This behavior suggests that, in the case 4-PPzBD reduction, there exists an initial rapid layer growth/coating formation due surface electrografting which happens approximately within the first 60 s of the reactions as depicted by the corresponding decay in charge. However, the modified Si-(4-PPzB) and Au-(4-PPzB) surfaces begin to show an increase in conductivity at later stages as depicted by the rapid exponential rise in charge after the inflection points. The exponential rise in charge observed in the case of 4-PPzBD electrografting after the initial surface modification stage may also suggests either the formation of conducting oligomer/polymeric structures on the surface or formation new surface bound conducting ionic species, (Surface)-Ph-PPz-H^+ BF_4^-.

3.3.2 EQCM Measurements: Electrografting of 4-PPzB on Au Surface

Figure 43 shows the EQCM measurement results obtained from the real-time electrodeposition of 4-PPzBD on Au substrate surface. It shows the dependence of the resonant frequency changes (Δf) in relation to the CV (line in red) obtained during the electrografting of 4-PPzBD on Au surface. Based on the CV, the reduction of the 4-PPzBD occurs between +0.25 V to about -0.8 V during the first cathodic scan. The characteristic first broad cathodic reduction wave observed and its disappearance in the subsequent scans provides evidence of surface modification due to the electroreduction of 4-PPzBD molecules. Faradic electrografting efficiency of about 17.8% (estimated using the Sauerbrey eq. 6 in section 2.3) was realized from the QCM electrografting on Au substrate.

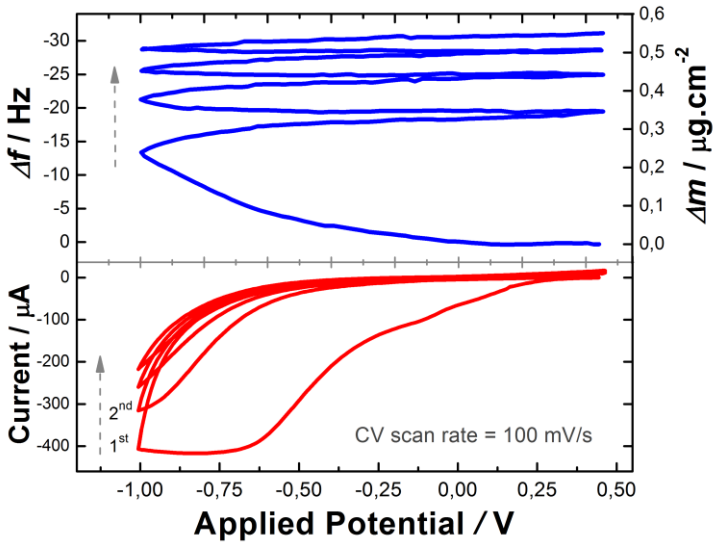

Figure 43: The variation of QCM frequency shifts (*Δf*) in relation to the CV derived from the electrografting of 10 mM 4-PPzBD on Au surface.

Figure 44 shows a plot of the variation of resonance frequency shift (*Δf*) along with the corresponding mass changes (*Δm*) for the first four potential cycles (+0.5 to -1.0V) during the electroreduction of 4-PPzBD. It reveals that the greatest decrease in *Δf*, which corresponds to the greatest increase in *Δm*, occurs within the first cycle during the electrografting of 4-PPzBD.

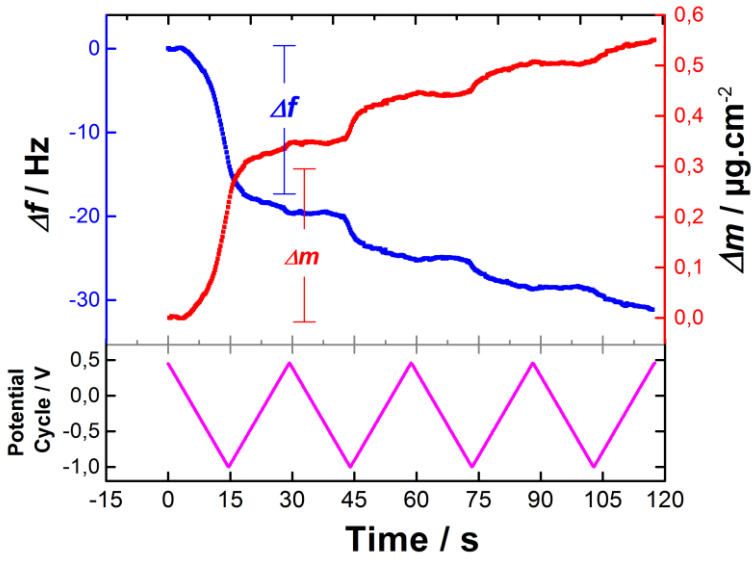

Figure 44: EQCM frequency shift (*Δf*) and calculated mass depositions (*Δm*) in relation to the potential cycles from the electrografting of 4-PPzBD on Au surface.

An estimated electrodeposited mass per unit area of ~ 0.30 µg/cm^2 is achieved within the first CV cycle, which reduces to an increase of ~ 0.10 µg/cm^2 in the second cycle. The formation of electrografted 4-PPzB that occurs within the first cycle contributes to the reduction of electrodeposited mass observed in the subsequent scans. Moreover, the estimated mass depositions in the subsequent cycles (3rd and 4th scans) show a diminishing trend in mass deposition. The smaller mass changes observed in the subsequent potential cycles (2nd, 3rd and 4th) most likely arise from the secondary electrografting reactions involving the residual 4-PPzBD diazonium cations next to the previously electrografted primary layers.

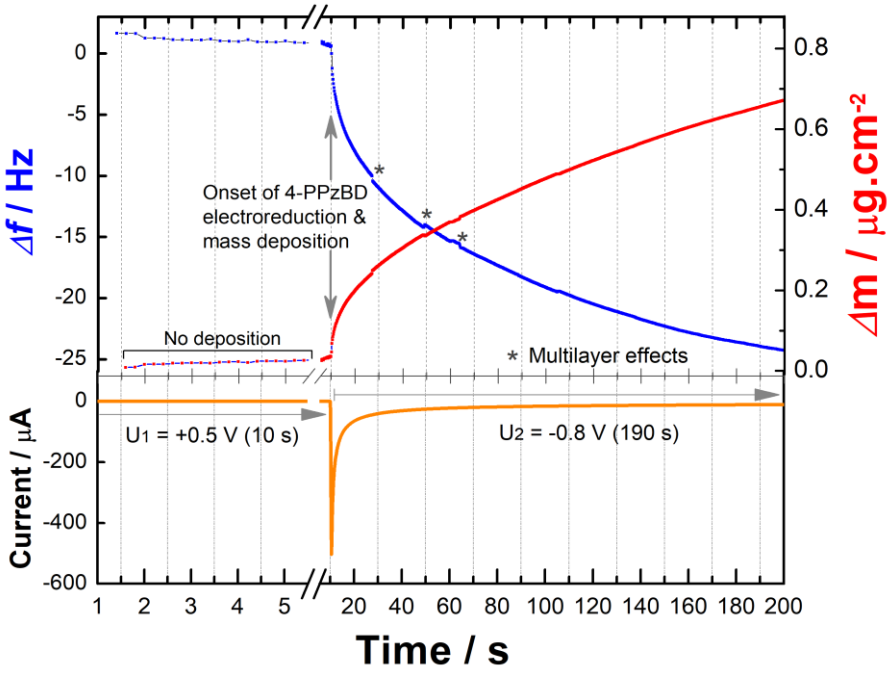

Figure 45: EQCM chronoamperometric deposition of 10mM 4-PPzBD on Au surface in highlighting the frequency response (Δ*f*), and the calculated mass deposition (*Δm*).

Figure 45 shows the recorded QCM-frequency response during the chronoamperometric electrodeposition 4-PPzBD on Au surface. When an initial anodic voltage of +0.5 V is fixed for a duration of 10 s, no electroreduction happens,

therefore no significant frequency change is detected within this period implying that no significant mass deposition occurs under such conditions. When a fixed cathodic potential of -0.8 V is applied, a characteristic sharp drop in current, as evident in the CA graph (orange line) is accompanied by a significant drop in the recorded QCM resonance frequency *Δf* (blue line). The current decay in the CA graph correspond to the rapid blocking of the Au electrode surface by 4-PPzB units due to the electroreduction of 4-PPzBD.

The marked change in resonance frequency observed from the onset of electroreduction reaction (from the 10^{th} s) characterizes the initial electrografting of 4-PPzB units on the Au surface hence providing evidence of initial layer formation. The observed points of discontinuity on the Δ*f* curve, marked by asterisks (*), suggests that the initially modified Au electrode surface is subsequently attacked randomly by residual 4-PPzBD radicals to produce thicker multilayer structures (secondary electrografting) during the chronoamperometric electrodeposition. The first visible sign of multilayer formation is recorded at about the 16^{th} second from the onset of the electrografting reaction after which they seem to become more important as the deposition progresses. The corresponding increases in mass deposition, as estimated from the Sauerbrey equation, reveal that the mass per unit area achieved via CA technique within the first 16 s is about 0.20 μg/cm^2, which doubles to ~ 0.40 μg/cm^2 within the at about the 90^{th} s of the electrografting. Based on the frequency response, the electrodeposition continues at relatively lower CA currents (about the 70^{th} – 100^{th} s of the reaction), which would suggest that the multilayer formation (or secondary electrografting) is, to some extent, influenced by the conductivity of the initially modified Au-(4-PPzB) surface layer(s).

3.3.3 IR Spectroscopy: Molecular Structure of the 4-PPzB Modified Surfaces

Figure 46 shows the IR transmission spectrum of the diazonium salt 4-PPzBD (orange line), and the normalized IRSE tan ψ spectra of the modified surfaces: Au–(4-PPzB) (red line) and Si–(4-PPzB) (blue line). The IR fingerprint spectrum of the powder sample of the diazonium compound, 4-PPzBD, contains the characteristic absorption bands of the diazonium groups at ~ 2180 cm^{-1}, the phenyl (Ph) ring at ~ 1588 cm^{-1}, the $–CH_2–$ vibrations in the PPz groups in the region 2800 – 2950 cm^{-1}. In addition, the two bands observed at about 1457 – 1526 cm^{-1} are ascribed to the PPz ring vibrations in the 4-PPzBD molecule.[114]

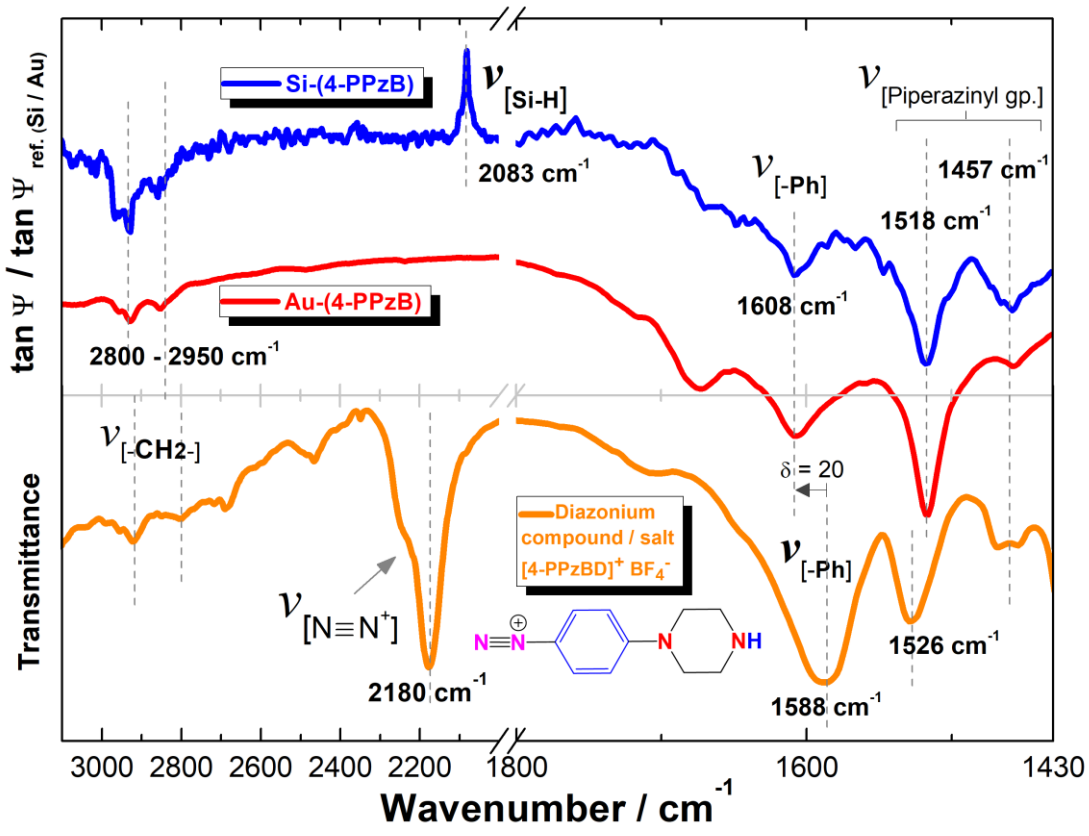

Figure 46: IRSE spectra of the Si-(4-PPzB) (blue), and Au-(4-PPzB) (red) surfaces and the IR transmission spectrum of the 4-PPzBD diazonium salt (orange).

The absorption peak of the diazonium group is conspicuously absent in both the IR spectra of the modified surfaces, Si-(4-PPzB) and Au-(4-PPzB). This is due to the loss of the diazonium group as nitrogen (N_2) gas upon electroreduction of the diazonium salt, 4-PPzBD, on the surfaces. The IRSE spectrum of the Si-(4-PPzB) surface is normalized against that of the Si-H surface and confirms the decrease of the surface Si-H bonds (inverted peak at ~ 2083 cm^{-1} after normalization) upon electrografting. The IR spectra in Figure 46 also reveal the absorption bands related to -CH_2- and PPz, which remain on the modified surfaces after the electrografting reactions. This provides a strong hint that the PPz chelating ligands are not degraded by the electrografting reaction, which points towards a successful surface functionalization strategy with PPz chelating ligands via diazonium grafting route.

The IR spectra in Figure 46 also reveals that the IR absorption peaks due to the aryl ring vibration shifts conspicuously by a magnitude of about 20 cm^{-1} towards higher wavenumbers from about 1588 cm^{-1} (in the diazonium salt) to about 1608 cm^{-1} (in the modified surfaces). This shift stems from the loss of the erstwhile present diazonium groups due to the electrografting process. It is a fact that the N atoms in the diazonium group ($N\equiv N^+$) are more electronegative than the carbon atoms of the Ph rings. In the case of the pure diazonium salt 4-PPzBD, the $N\equiv N^+$ group would therefore partially abstract some electron density from the electron rich aromatic Ph-rings via inductive effects. The absence of the inductive effect contributions from the diazonium groups in the modified Si-(4-PPzB) and Au-(4-PPzB) surfaces is therefore the genesis of the observed shifts in the Ph-ring IR absorption bands. The shifting of the Ph-ring absorption bands is also evident in Figure 25 (in the case in 4-CMTB surface electrografting discussed earlier in section 3.2.3).

3.3.4 Kinetics of [4-PPzBD] Electroreduction on Si(111)-H and Au Surfaces

Figures 47a, 47c, and 47e shows the graphical test for first-order kinetics for the electroreduction of 4-PPzBD within the first 50 s, 20 s, and 10 s respectively, while Figures 47b, 47d and 47f show the corresponding tests for second-order kinetics.

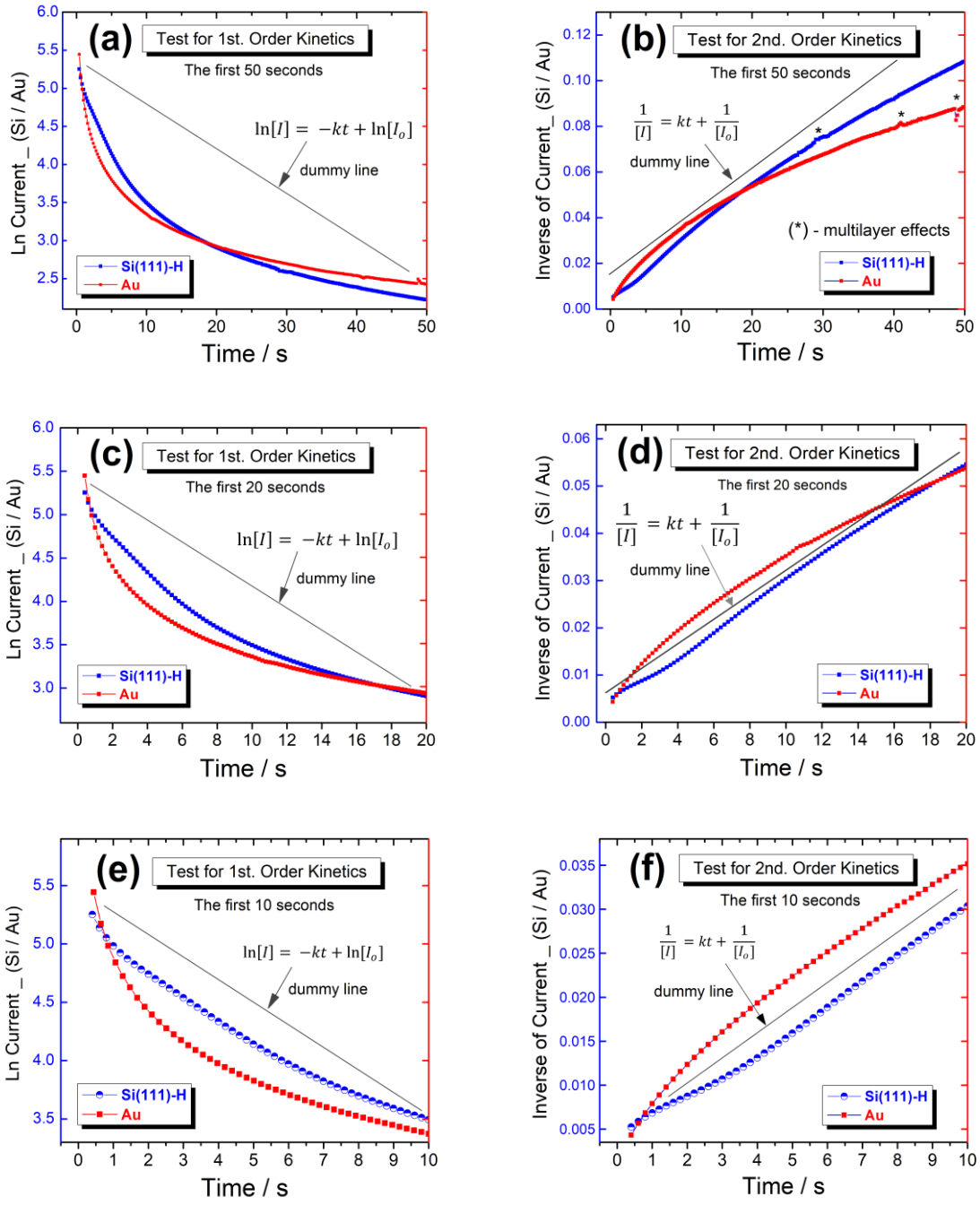

Figure 47: Kinetic analysis of the experimental CA data from the electroreduction of 4-PPzBD on Si(111)-H and Au surfaces.

The graphs in Figures 47a, 47c, and 47e (the tests for first-order kinetics), show pronounced deviations, whereas in Figures 47b, 47d, and 47f (the tests for second-order kinetics), only relatively smaller deviations are observed with respect to the linear plot. In Figure 47b, the electroreduction of 4-PPzBD closely approximates to that of the integrated second-order rate equation, however, the deviations seem to become more pronounced at later stages (~30 – 50 s), suggesting that electrografting reaction has reached critical stages where the rates begins to be affected by the products formed (the multilayer formation as highlighted in both curves). In Figures 47d and 47f, the electroreduction of 4-PPzBD on both Si(111)-H and Au surfaces seem to exhibit much better approximations towards the integrated second-order equation within the early stages (0 - 20 s) of the electrografting reaction. In Figure 47f (0 – 10 s), both kinetic curves begin to turn at about the 3rd – 4th second of the reaction, perhaps distinguishes the primary grafting events from secondary grafting events in the two different substrate surfaces (Si(111)-H and Au).

Figures 48 shows the fitted test graphs for the (a) first- and (b) second- order kinetics for the first three seconds of the electroreduction of 4-PPzBD on Si(111)-H and Au surfaces. The comparative analysis here (in Figure 48a and 48b) is of interest since electrografting/deposition the initial layer (or primary grafting) to begin in this period (as also attested by the EQCM results in section 3.3.2, Figure 45). It can be noted from the fitted lines that the values of the coefficient of determination (R^2) are somewhat lower in the graphical fitted test for first-order kinetics (Figure 48a) compared to those in tests for second-order kinetics (Figure 48 b). In the fitted test for second-order kinetics, all the R^2 values are above 99 %, which is not the case in the test for first-order kinetics.

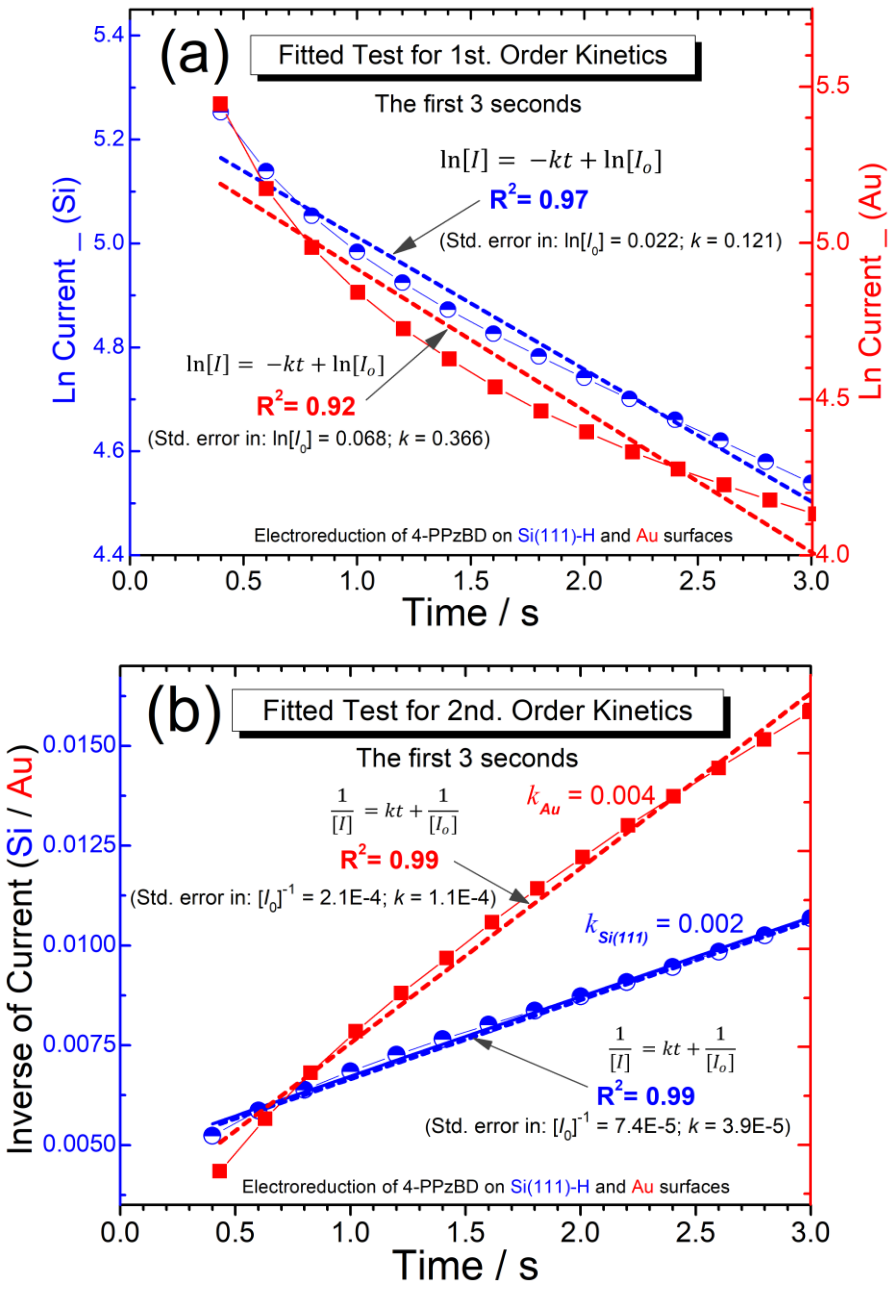

Figure 48: The fitted analysis of the (a) first- and (b) second- order kinetics for the first three seconds of the electroreduction of 4-PPzBD on Si(111)-H and Au surfaces.

It can also be noted that the regression standard errors (in the intercepts: $\ln[I_o]$ and $[I_o]^{-1}$ and slope, k) are higher (orders of 10^{-1} to 10^{-2}) in the fitted first-order test graph (Figure 48a) in comparison to the corresponding standard errors in the fitted second-order test graph (Figure 48b), whose magnitudes are in the orders of 10^{-4} to 10^{-5}. The lower standard errors reported in the regression fitting in Figure 48b provides

proof that the experimental kinetic data from the electroreduction of 4-PPzBD on both Si(111)-H and Au surfaces fits the integrated second-order rate law in a near perfect manner as opposed to first-order kinetics in the early stages of electrografting (from 0 to 3 s or 3000 milliseconds). Moreover, it can also be noted that the rate of electroreduction of 4-PPzBD occurs approximately two times faster on Au surface than on Si(111)-H surface within the first three seconds based on a comparison of the values of the calculated rate constants, k_{Au} and $k_{Si(111)}$ (Figure 41b).

In summary, the kinetic analysis of the experimental data as presented in Figures 47 and 48 reveal that the electroreduction of 4-PPzBD on both the Si(111)-H and Au surfaces follows second-order kinetics in the early stages of the reaction. Therefore, the differential rate equation governing the early stages of the electroreduction of 4-CMTBD that leads to the grafting of 4-CMTB units on both Si(111)-H and Au surface can be represented by equation 17;

$$Rate = -\frac{d[(4\text{-PPzBD})]}{dt} = k[(4 - \text{PPzBD})]^2 \quad \text{------ (Eq. 17)}$$

where *d*[(4-PPzBD)]/*dt* = the rate of electroreduction of 4-PPzBD over time, *k* = the rate constant, and [(4-PPzBD)] = the concentration of the aryl diazonium cation 4-PPzBD. Equation 17 here means that the order of the reaction with respect to [(4-PPzBD)] is two.[97]

Although the electroreduction of both 4-PPzBD and 4-CMTBD (discussed in earlier section 3.2.4) follow second-order kinetics, their rate constants in the early stages of electroreduction (0 - 3 s) are different (compare Figures 27 and 48). Based on the kinetic analysis of the chronoamperometric data, the electroreduction of 4-PPzBD proceeds at lower rates in comparison to 4-CMTBD.

3.3.5 Raman Spectroscopy: Chelate Complex Formation (Cu Binding)

The Raman spectra obtained from the surfaces of Si-H, Si-(4-PPzB), and Si-(4-PPzB)-Cu are presented in Figures 49a, 49b and 50. The spectroscopic investigations reveal the emergence (after the chelation reaction) of two Raman bands at about 167 cm^{-1} (Figure 49a), and ~ 432 cm^{-1} (Figure 49b), which are attributed to the binding of Cu to the PPz groups on the Si-(4-PPzB) surface.

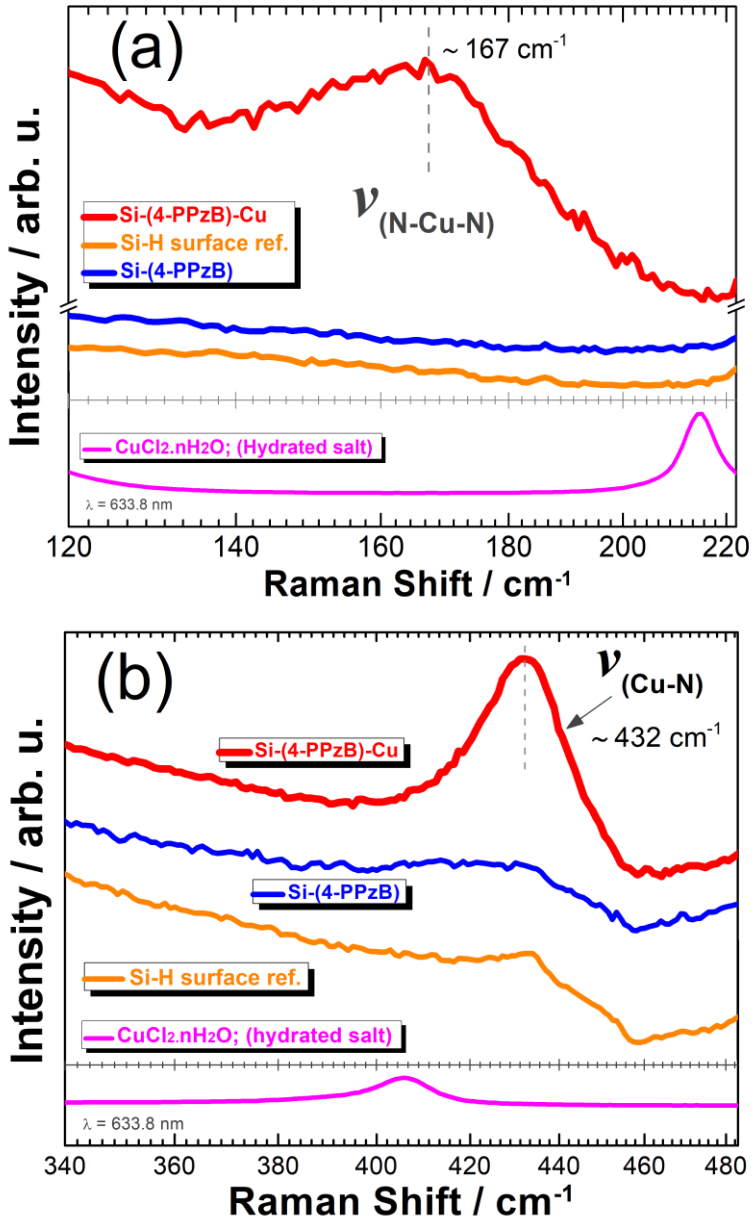

Figure 49: Raman spectra of the Si-H, Si-(4-PPzB), Si-(4-PPzB)-Cu surfaces and the hydrated salt of $CuCl_2$ highlighting the (a) N-Cu-N and (b) Cu-N related vibrational bands.

The broad Raman band on the Si-(4-PPzB)-Cu spectrum observed with a midpoint at about 167 cm^{-1} (Figure 49a) can be ascribed to the N-Cu-N vibration, while the Raman band in the Si-(4-PPzB)-Cu spectrum with a peak at ~ 432 cm^{-1} (Figure 49b) can be assigned to the Cu-N stretching vibration mode.[102,103] The Raman spectra of Si-(4-PPzB) (blue line) and Si-H (orange line) surfaces show no pronounced bands in the range 130 - 220 cm^{-1} (Figure 49a), neither do they reveal an intense broad peak in the region between 400 – 460 cm^{-1} (Figure 49b). The spectrum of the hydrated $CuCl_2$ salt also shows no Raman bands coincident with the observed N-Cu-N and Cu-N related bands (Figures 49a and 49b).

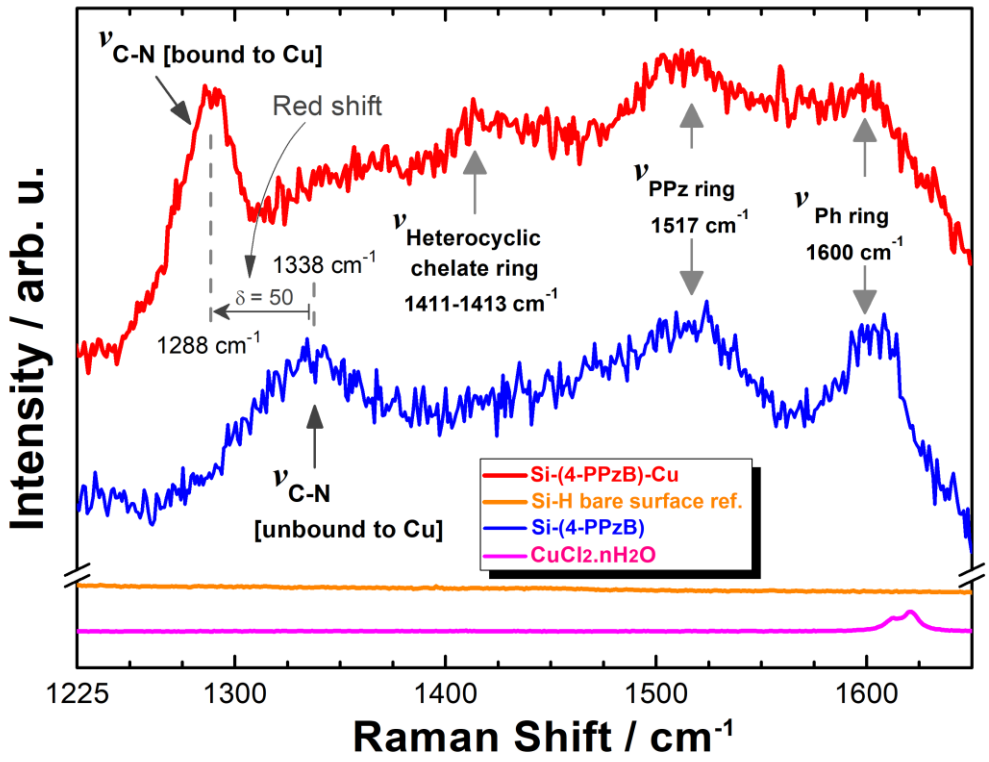

Figure 50: Raman spectra of the $CuCl_2.nH_2O$ powder (magenta), the surfaces of the Si-H (orange), and the Si-(4-PPzB) (blue).

Figure 50 shows a section of the Raman spectra in region 1225 – 1650 cm^{-1}, which typically contains the vibrational bands related to the characteristic C-N (present in

the PPz group in this case) and the Ph – ring groups. The binding of Cu via the N donor atoms of the PPz ligands would lead to the formation of five-membered heterocyclic Cu containing chelate rings on the Si-(4-PPzB)-Cu surface, which can be rationalized by the emergent Raman band at about 1411 - 1413 cm^{-1} in the Si-(4-PPzB)-Cu spectrum (the spectrum in red, Figure 50).[115] The Raman spectra of the hydrated $CuCl_2$ (magenta) and that of the Si-H surface (orange) show no vibrational bands coincident with those existing in the Si-(4-PPzB) and the Si-(4-PPzB)-Cu surfaces in this range. The Raman spectrum of Si-(4-PPzB) surface shows three major peaks at ∼1338, ∼1516 and ∼1600 cm^{-1}, while the Si-(4-PPzB)-Cu surface has four pronounced Raman bands at ∼ 1288, ∼ 1413, ∼ 1516 and ∼ 1600 cm^{-1}. The two Raman bands at ∼ 1516 and ∼ 1600 cm^{-1}, that are present in the spectra of both the Si-(4-PPzB) and Si-(4-PPzB)-Cu surfaces are attributed to the PPz and Ph- ring vibrational modes respectively. These two bands are also evident in the IRSE spectra discussed under section 3.3.3 in Figure 46.

The Raman bands related to the PPz- ring and Ph- ring vibrations do not shift upon Cu binding (Figure 50). However, a conspicuous red-shift is evident within the region 1250 – 1380 cm^{-1}. The vibrational mode related to the C-N stretching typically occurs in the region between 1250 - 1360 cm^{-1}.[116] The Raman band related to the C-N vibrational shifts to lower wavenumbers (a red-shift of about 50 cm^{-1}) upon chelation of Cu by the Si-(4-PPzB) surface. The observed bathochromic / red-shift arises due to the delocalization of the electron density from the N donor atoms into the Cu valence shells (formation of Cu-N bonds), which in effect would weaken the C-N bonds of the PPz ligands. This explains why the C-N bonds of the PPz ligands vibrate at lower energies when the N atoms are bound to Cu metal.

3.3.6 X-ray Spectroscopy: Characterization of the Modified Surfaces and Cu Uptake

Figure 51 shows the X-ray photoelectron survey spectra of the Si−H, Si−(4-PPzB), and Si−(4-PPzB)−Cu surfaces. The N1s signals at about 400 eV, which emanate from the PPz chelating groups, are present in the spectra of both Si−(4-PPzB) and Si−(4-PPzB)-Cu on the surfaces. The Si-H spectrum has no N1s peak except that its Si2p signal shows the greatest intensity of the three spectra. The C1s and O1s signals in the Si-H spectrum are largely of adventitious origin.

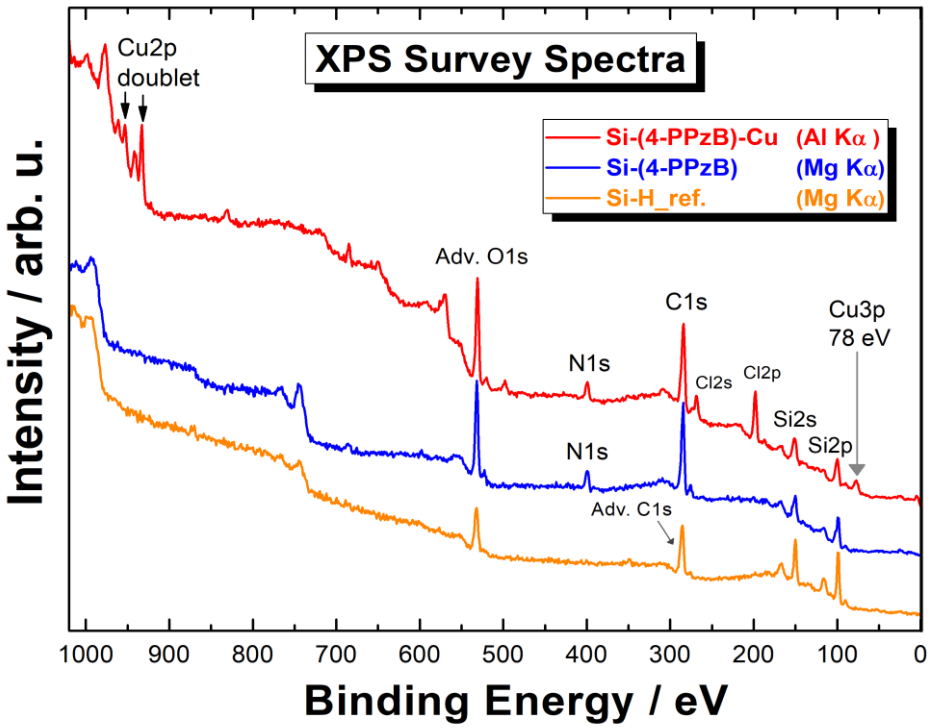

Figure 51: XPS broad survey of the Si-H (orange), Si-(4-PPzB) (blue), and Si-4-PPzB-Cu (orange) surfaces.

The intensities of the C1s signals (285 eV) on the modified surfaces, Si-(4-PPzB) and Si-(4-PPzB)-Cu, are higher than in the Si-H surface due to the extra contributions arising from the electrografted 4-PPzB organic units. Furthermore, the C1s signals of the modified surfaces show higher intensities compared to the

corresponding Si2p signals in their respective spectra as opposed to the C1s : Si2p intensity ratio observed in the Si-H spectrum. This provides evidence of the formation of organic overlayer on the modified surfaces.

The O1s (530 eV) peaks in the modified surfaces, Si−(4-PPzB) and Si−(4-PPzB)-Cu; also possess higher intensities due to washing of the surfaces with water (H_2O) upon surface modification and the subsequent treatment with aqueous Cu solution. The presence of Cu on the Si−(4-PPzB)-Cu surface is qualitatively confirmed by the evident Cu3p (78 eV) and Cu2p (935 – 955 eV) signals.

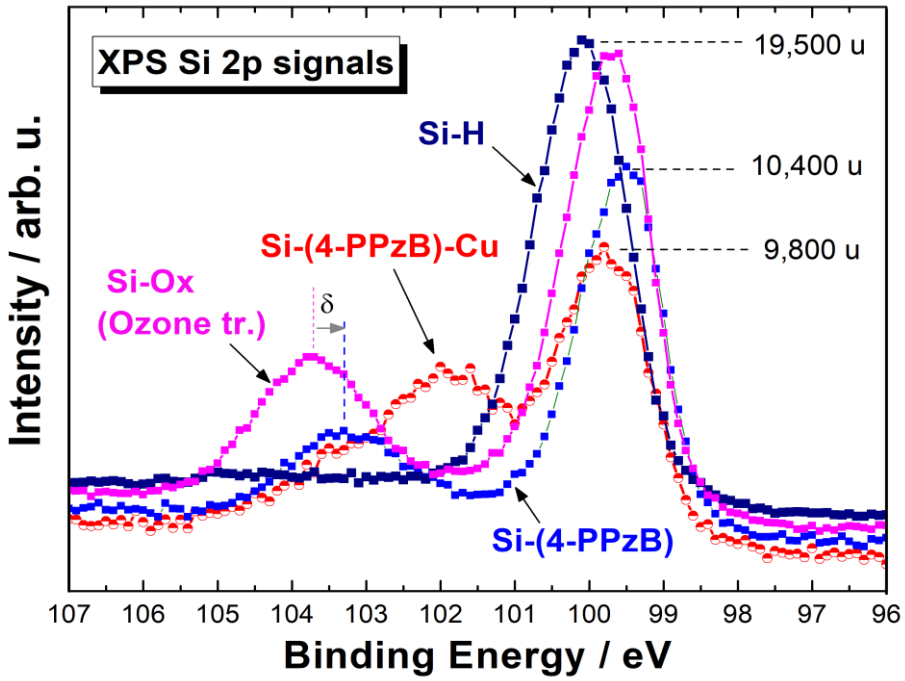

Figure 52: Comparison of the XPS Si2p signals of the Si-H (navy-blue), Si-Ox (magenta), Si-(4-PPzB) (blue) and Si-(4-PPzB)-Cu (red) surfaces.

Figure 52 shows a comparative XPS analysis performed under similar measurement parameters to characterize the individual Si2p signals for the Si-H, Si-Ox, Si-(4-PPzB) and Si-(4-PPzB)-Cu surfaces. Although the four Si2p signals cogitate around 99.5 – 100.1 eV, they reveal some unique characteristics in terms of the difference in

shape and the relative intensities. The Si-Ox surface (with the Si-O bonds, produced as a reference via Ozone treatment) contains the surface oxides such as SiO_2, as depicted by the characteristic satellite peak at about 103.8 eV, specifically denotes the presence of the $Si^{(4+)}$ species on the surface.[117] The bare Si(111)-H surface contains no such satellite peak except for the prominent peak at ~ 99.6 eV indicating the predominance of the $Si^{(0)}$ and $Si^{(1+)}$ species.[117] It can be deduced from the pronounced satellite peak around 103.2 eV, that the attachment of Ph- groups (via formation of Si-C bonds) on the Si(111) surface is characterized by enhanced contributions of Si^{3+} and Si^{2+} species to the Si2p signal as depicted in the Si-(4-PPzB) spectrum (blue).[117] This emergent oxidation states points to the aftermath of free radical reactions (during electrografting reaction), which re-organizes the valence shell electron configuration of the Si atoms on the modified substrate surface.

Another key feature observed in the Si2p signal of the Si-(4-PPzB)-Cu surface (in red) is the emergence of a new pronounced shoulder peak at ~ 102 eV, which is not prominent in the spectrum of Si-(4-PPzB) surface (Figure 52). The organometallic Cu-PPz chelate rings (or Cu-N bonds) neighbouring the Si substrate atoms in the Si-(4-PPzB)-Cu surface is most likely a the major contributing factor for the observed shoulder peak (at ~ 102 eV) since the Si-(111)-H surface treated only with Cu ions show no such shoulder peak.

In Figure 52, both the Si-H and the Si-Ox surface shows comparable signal intensities as they contain no organic layers as opposed to the other two modified surfaces: Si-(4-PPzB) and Si-(4-PPzB)-Cu. It is evident that the binding of 4-PPzB upon surface modification causes a decrease in the signal intensity with respect to

the Si2p signal intensity of the Si-H surface due to the attenuation of photoemission by the grafted overlayer.

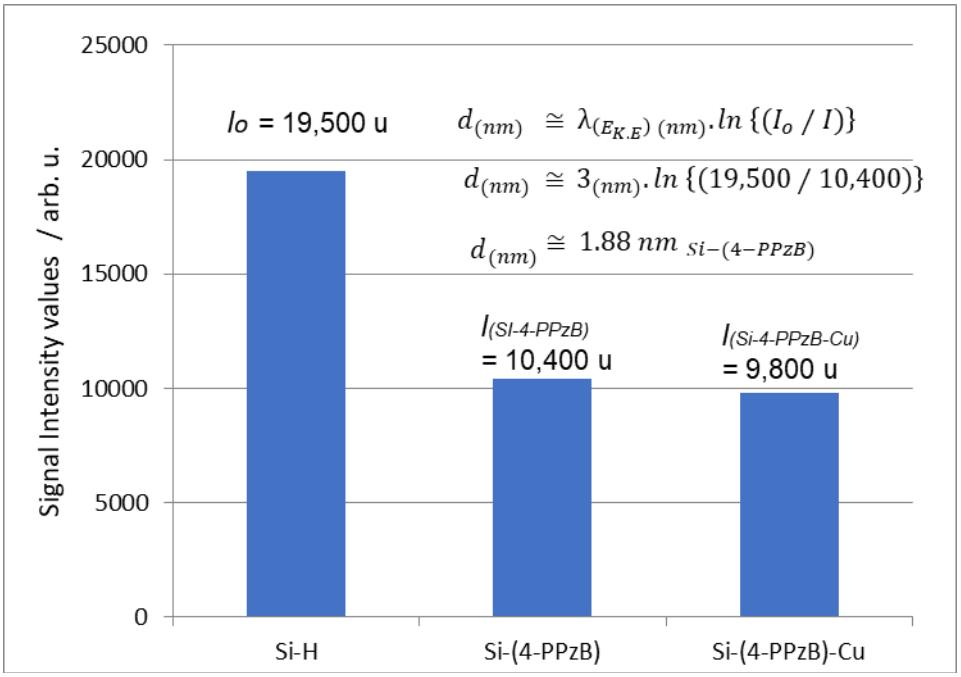

Figure 53: Plot of the Si2p signal intensities of Si-H, Si-(4-PPzB) and Si-(4-PPzB)-Cu for overlayer thickness estimation.

Figure 53 contains the plot of the experimentally derived Si2p signal intensities obtained under a new set of similar XPS parameters, and the calculations for the estimation of overlayer thicknesses based on the Beer-Lambert X-ray photoemission decay equation. The thickness for the Si-(4-PPzB) surface was approximately 1.88 nm while on the Si-(4-PPzB)-Cu surface it was about 2.06 nm. Relatively thinner layers are realized in the case of 4-PPzBD electrografting as opposed to the case of 4-CMTB electrografting discussed in section 3.2.6 (see Table 2 and Table 3). In addition, there is a marginal drop in the XPS signal intensity upon Cu chelation by the Si-(4-PPzB) surface (Figure 53) compared to a larger drop in the case of Si-(4-CMTB) surface (Figure 36). This shows that thinner grafted layers (in the case of Si-(4-PPzB) surface) act to trap or chelate lower amounts of Cu in comparison the

thicker layers (such as in the case of Si-(4-CMTB)-Cu surface, Figure 36) even though coordinate-covalent metal-ligand bonds are observed by Raman spectroscopic measurements (discussed in sections 3.2.5 and 3.3.5).

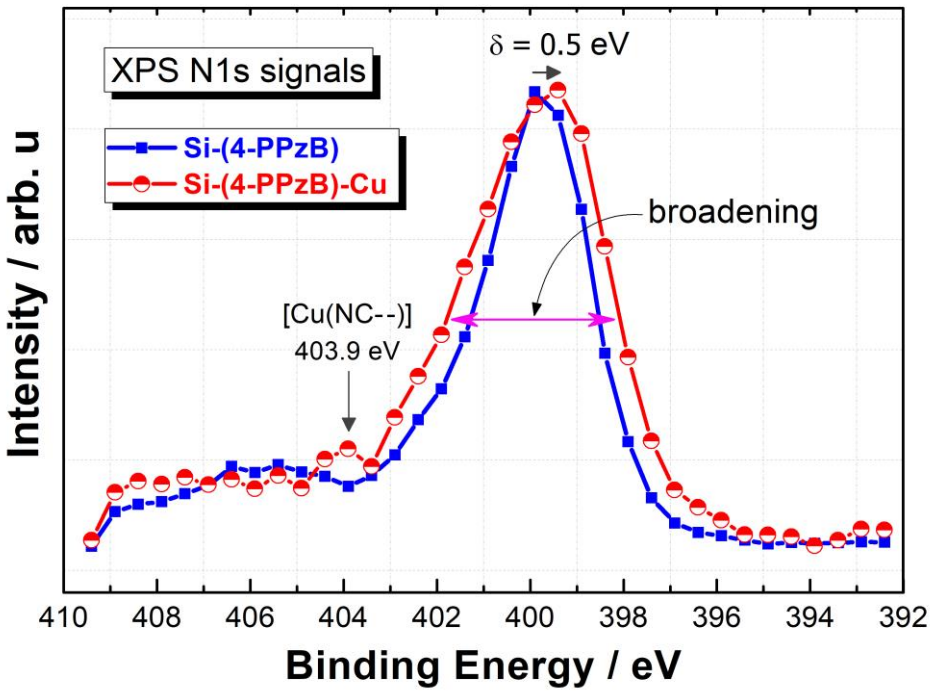

Figure 54: XPS N1s signals from the Si-(4-PPzB) (blue) and Si-(4-PPzB)-Cu (red) surfaces.

Figure 54 shows a comparison of the N1s signals obtained from the Si-(4-PPzB) and Si-(4-PPzB)-Cu surfaces under similar measurement conditions. The N1s peak from the Si-(4-PPzB) surface is narrow whereas the N1s signal from the Si-(4-PPzB)-Cu surface broader. Moreover, the emergent peak at ~ 403.9 eV in the N1s signal from the Si-(4-PPz)-Cu surface characterizes the formation of Cu-N bonds in chelate complex environments.[83] The broadening can be attributed to the increase in disorder due to the formation of multiple Cu-N coordinate bonds or organometallic heterocyclic chelate ring framework on the Si-(4-PPzB)-Cu surface. The N1s signal from the Si-(4-PPzB)-Cu surface is shifted to a lower binding energy by approximately 0.5 eV relative the N1s signal from the Si-(4-PPzB) surface. This shift denotes the alteration of the chemical state on N atoms upon the formation the Cu-N

coordinate bonds, which occurs via the delocalization of electron density from the valence shells of N atoms into the Cu valence orbitals.

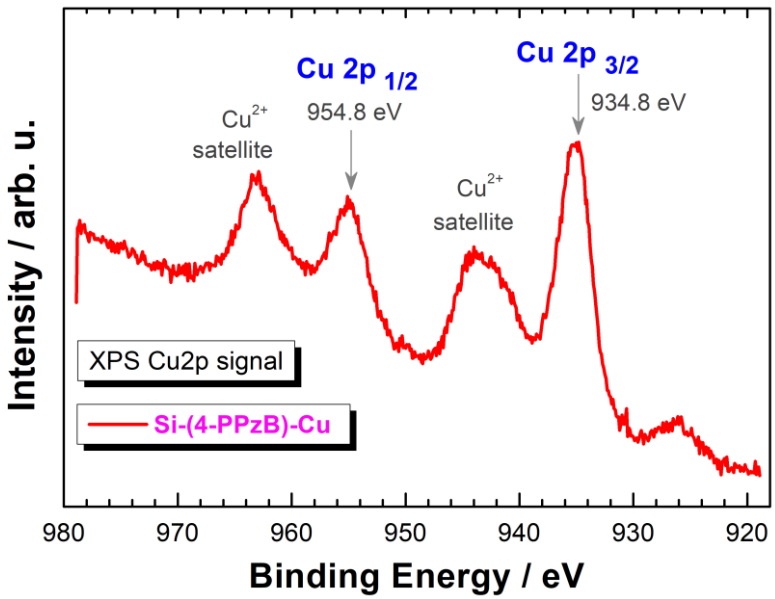

Figure 55: XPS Cu 2p signal obtained from the Si-(4-PPzB)-Cu surface.

Figure 55 shows the Cu2p doublet signal derived from the Si-(4-PPzB)-Cu surface. The $Cu2p_{3/2}$ signal appears at about 934.8 eV, and the $Cu2p_{1/2}$ signal appears at about 954.8 eV with a peak separation of about 20 eV. It also reveals the oxidation state of Cu on the surface as (+2), based on the observed characteristic satellite peaks. Furthermore, the Cu $2p_{3/2}$ line designation at 934.8 eV from the NIST database indicate a Cu-N environment in which the N atoms are present within coordination sphere of the resulting complex.[118] The Cu^{2+} satellite peaks in this case appears somewhat sharper compared those obtained from the Si-(4-CMTB)-Cu surface shown in section 3.2.6 (Figure 34a). It can be noted that the satellite peak at about 963 eV shows similar intensity to the $Cu2p_{1/2}$ peak in the case of Si-(4-PPzB)-Cu surface (Figure 55), which is not the case in Si-(4-CMTB)-Cu surface (Figure 34a).

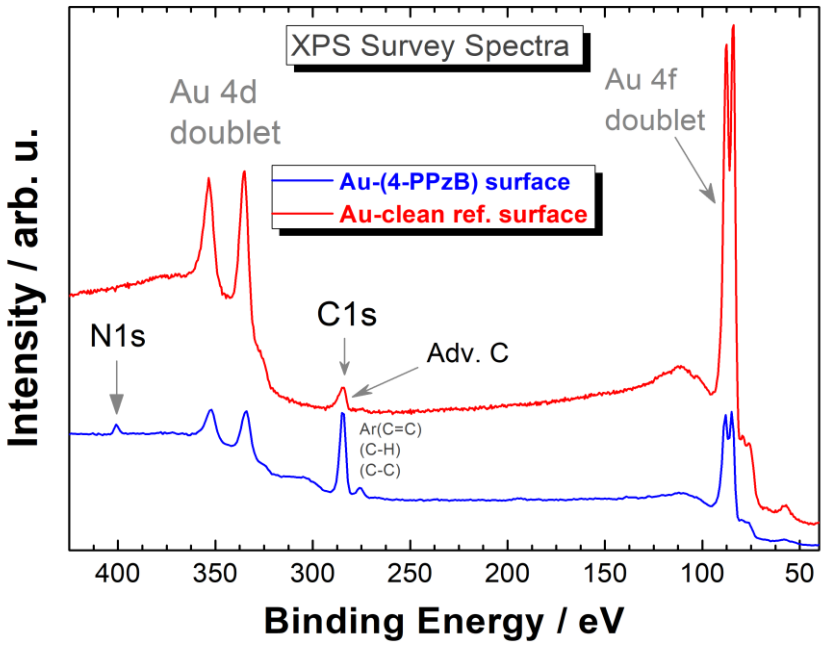

Figure 56: XPS survey for the clean Au surface (red) and Au-(4-PPzB) (blue).

Figure 56 shows a section of the XPS survey spectra obtained from the Au-(4-PPzB) surface and the clean non-functionalized Au reference surface. The doublet signals of Au4f and Au4d are reduced in intensities on the Au-(4-PPzB) surface in comparison of the corresponding signals in spectrum of the clean Au surface. This provides evidence of thin layer formation containing the grafted overlayer of 4-PPzB units. The N1s peak (~ 400 eV) present on the Au-(4-PPzB) surface confirms the presence of PPz groups on the surface. In addition, the C1s signal on the Au-(4-PPzB) has a more intense peak than that of the adventitious C1s peak on the clean Au reference surface. This is due to the extra carbon contributions from the grafted 4-PPzB organic groups.

Figure 57 shows a more detailed analysis of the XPS Au 4f peaks for the estimation of the thickness of the electrografted layers on Au-(4-PPzB) surface. The attenuation of XPS signal intensity here confirms the presence of a coating layer of grafted 4-PPzB units on the modified Au surface.

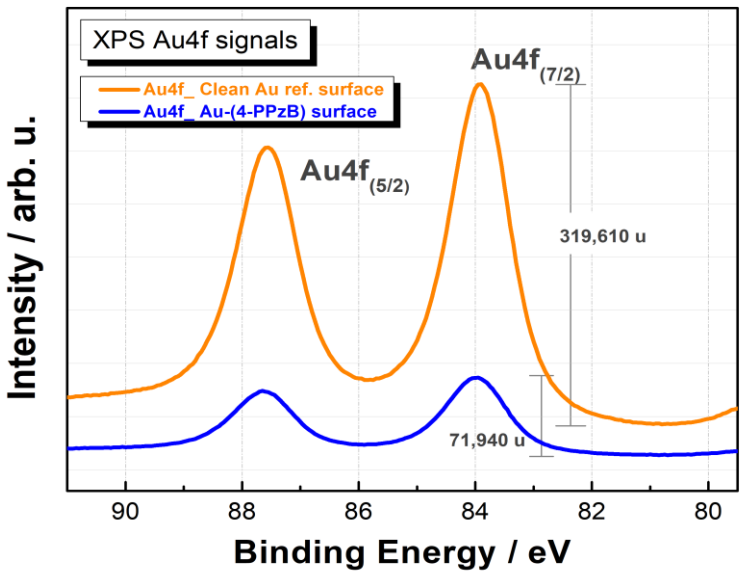

Figure 57: XPS Au 4f signals obtained from the clean Au (orange) and Au-(4-PPzB) (blue) surfaces.

Table 3: Summary of the overlayer thickness estimates from 4-PPzB grafting.

Si-(4-PPzB)	Au-(4-PPzB)	Si-(4-PPzB)-Cu
1.88 nm	2.98 nm	2.06 nm

The calculated thickness based on the Beer-Lambert X-ray photoemission decay equation was found to be about 2.98 nm as summarized in Table 3. Based on a comparison of the experimental values in Tables 3 and 2 (section 3.2.6), it can be noted that the electrografting of 4-CMTB and 4-PPzB on Au substrates tend to produce thicker overlayers (3.40 and 2.98 nm respectively) compared to the electrografting on Si(111) surface (3.88 and 1.88 nm respectively). Although both the Si-(4-CMTB) and Si-(4-PPzB) surfaces bind Cu, the former chelating surface seems a better Cu trap based on the XPS overlayer thickness measurements: Si-(4-CMTB)-Cu (4.50 nm) and Si-(4-PPzB)-Cu (2.06 nm) (Tables 2 and 3).

4.0 SUMMARY AND FUTURE PROSPECTS

This work was primarily concerned with the design and investigation of surface functionalization strategies that exploit aryl diazonium electrografting route as a means of fabricating chelate modified surfaces, which can target Cu and Pb ions. In this surface modification approach, the aryl groups behave as the direct organic substrate-linker, while the pendant chelating groups or ligands function as “molecular machines” - responsible for the adsorption and subsequent HMI binding in solution.

The carboxymethylthio- (CMT), and piperazinyl- (PPz) chelating groups were successfully grafted onto the Si(111) and Au surfaces via the direct cathodic electroreduction of their corresponding aryl diazonium salt derivatives: [4-CMTBD]$^{+}BF_4^{-}$, and [4-PPzBD]$^{+}BF_4^{-}$. The presence of the electrografted units on the functionalized Si(111)-H and Au surfaces was confirmed by IRSE, Raman and XPS spectroscopic techniques. The kinetic analysis of the rate of decay in currents accompanying the electroreduction of 4-CMTBD and 4-PPzBD on both the Si-(111)-H and the Au surfaces, as derived from the respective experimental chronoamperometric data, showed a correlation with the integrated second-order rate equation within the early stages of the electrografting process. Consequently, the differential rate laws for their electrografting kinetics were proposed. The electrochemical quartz crystal microbalance (EQCM) electrografting measurements on the Au surface was used to study the mass deposition measurements, which revealed the Faradaic efficiencies of about 19.9 % (in the case of 4-CMTB) and about 17.8% (in the case of 4-PPzB).

The attachment of the electrografted 4-CMTB and 4-PPzB units on the Si(111) and Au surfaces was characterized by the presence of their specific vibrational signature bands on the modified surfaces and the disappearance of the diazonium related absorption band after the electroreduction reaction. In addition, the absorption bands related to the substrate-linker (aryl group) were observed to shift towards higher wavenumbers by ~ 20 cm^{-1} (in the case of 4-CMTB grafting) and ~ 30 cm^{-1} (in the case on 4-PPzB grafting). This shifting of absorption bands is attributed to the vanishing of the inductive effect contributions from the N_2^+ groups present in the erstwhile aryl diazonium cations before the electrografting reactions. The XPS Si2p signal attenuation measurements revealed the formation of grafted thin layers of 4-CMTB (3.08 nm) and 4-PPzB (1.88 nm) on the Si(111) surface. The grafting of the PPz chelate seems to be hindered by steric factors due to its slightly larger size hence the realization of relatively thinner layers as opposed to the grafting of CMT chelate.

The Raman and XPS spectroscopic investigations the formation of organometallic chelate complexes on the CMT and PPz modified Si(111) surfaces. The observed Cu-O, Cu-S, Pb-S and Pb-O related Raman bands demonstrated the ability of the Si-(4-CMTB) surface to trap and covalently bind Cu and Pb ions. The binding of Cu by PPz groups on the Si-(4-PPzB) surface was characterized by a red shift within the C-N region of about 50 cm^{-1} while the binding of Cu by the CMT ligand on the Si-(4-CMTB) showed a red shift of about 10 cm^{-1} within the C-O region. The broadening of the XPS N1s signal also characterized the formation of Cu-N bond formation. In addition, the binding of Cu on the chelate-modified surface revealed an emergent distinctive satellite peak at ~ 102 eV within the XPS Si2p signal, which was a unique

feature that was not observed on the Si2p signals of the Si-H, Si-(4-CMTB), Si-(4-PPzB) and the predominantly oxidised Si surfaces.

The fabricated chelate-modified surfaces developed, tested and characterized in this work not only extends the knowledge in the field of organic functionalization of Si(111)-H and Au surfaces, but also opens up the a myriad possibilities towards developing interesting applications that involve the trace-level trapping of Cu and Pb. They exploit fairly selective metal – ligand interactions such as adsorption and coordination and therefore they could complement existing advances in HMI recognition or bio-sensing applications. These chelate-modified surfaces may further actuate efforts in the fabrication of disposable analytical micro-chip assay kits for selected HMI's, which could potentially be used in industrial effluent contamination monitoring for environmental protection. They could also be used in the forensic diagnostic testing of the selected HMI's in biological fluids such as urine or blood samples. The chelating surfaces may also form a basis for the future development of new adjunct bio-medical HMI remediation strategies for the pharmacological testing of HMI toxicity and rapid non-intravenous chelation strategies in cases of acute Pb or Cu toxicity diagnosis. Finally, apart from being exploited for selected heavy metal (HM) remediation applications, they may also be employed towards developing field sampling analytical kits for HMI prospecting or for HMI recovery efforts.

References

(1) Schwarzenbach, G. Der Chelateffekt. *Helv. Chim. Acta* **1952**, *35* (7), 2344–2359.

(2) Martell, A. E.; Hancock, R. D.; Motekaitis, R. J. Factors Affecting Stabilities of Chelate, Macrocyclic and Macrobicyclic Complexes in Solution. *Coord. Chem. Rev.* **1994**, *133* (C), 39–65.

(3) House, J. E. Factors Affecting Stability of Complexes. In *Inorganic Chemistry*; Academic Press (Elsevier): San Diego, USA, 2008; pp 685–690.

(4) Housecroft, C. E.; Sharpe, A. G. Stability Constants of Coordination Complexes. In *Inorganic Chemistry*; Pearson Education Limited: England, 2005; pp 185–186.

(5) Neilands, J. B. Siderophores: Structure and Function of Microbial Iron Transport Compounds. *J. Biol. Chem.* **1995**, *270* (45), 26723–26726.

(6) Lawrance, G. A. *Introduction to Coordination Chemistry*; John Wiley & Sons, Ltd: Chichester, UK, 2010.

(7) Kharisov, B. I.; Kharissova, O. V.; Méndez, U. O. Nanomaterials on the Basis of Chelating Agents, Metal Complexes, and Organometallics for Environmental Purposes. In *Nanomaterials for Environmental Protection*; John Wiley & Sons, Inc: Hoboken, NJ, 2014; pp 109–124.

(8) Evangelou, M. W. H.; Ebel, M.; Schaeffer, A. Chelate Assisted Phytoextraction of Heavy Metals from Soil. Effect, Mechanism, Toxicity, and Fate of Chelating Agents. **2007**.

(9) Satpati, S. K.; Pal, S.; Goswami, D.; Tewari, P. K.; Roy, S. B. Extraction of Uranium from Nuclear Industrial Effluent Using Polyacrylhydroxamic Acid Sorbent. *Int. J. Environ. Sci. Technol.* **2015**, *12* (1), 255–262.

(10) Zhou, L.; Bosscher, M.; Zhang, C.; Ozçubukçu, S.; Zhang, L.; Zhang, W.; Li, C. J.; Liu, J.; Jensen, M. P.; Lai, L.; He, C. A Protein Engineered to Bind Uranyl Selectively and with Femtomolar Affinity. *Nat. Chem.* **2014**, *6* (January), 236–241.

(11) Hancock, R. D.; Melton, D. L.; Harrington, J. M.; McDonald, F. C.; Gephart, R. T.; Boone, L. L.; Jones, S. B.; Dean, N. E.; Whitehead, J. R.; Cockrell, G. M. Metal Ion Recognition in Aqueous Solution by Highly Preorganized Non-Macrocyclic Ligands. *Coord. Chem. Rev.* **2007**, *251* (13–14 SPEC. ISS.), 1678–1689.

(12) Geng, B.; Jin, Z.; Li, T.; Qi, X. Preparation of Chitosan-Stabilized Fe(0) Nanoparticles for Removal of Hexavalent Chromium in Water. *Sci. Total Environ.* **2009**, *407*, 4994–5000.

(13) Abu-Daabes, M. A.; Pinto, N. G. Synthesis and Characterization of a Nano-Structured Sorbent for the Direct Removal of Mercury Vapor from Flue Gases by Chelation. *Chem. Eng. Sci.* **2005**, *60* (7), 1901–1910.

(14) Murthy, Z. V. P.; Choudhary, A. Separation of Cerium from Feed Solution by Nanofiltration. *Desalination* **2011**, *279* (1–3), 428–432.

(15) Szurdoki, F; Kido, H; Hammock, D. Development of Rapid Mercury Assays. Synthesis of Sulfur- and Mercury- Containing Conjugates. *Bioconjugate Chem.* **1995**, *6* (2), 145–149.

(16) Sugunan, A.; Thanachayanont, C.; Dutta, J.; Hilborn, J. G. Heavy-Metal Ion Sensors Using Chitosan-Capped Gold Nanoparticles. In *Science and Technology of Advanced Materials*; 2005; Vol. 6, pp 335–340.

(17) Koehler, F. M.; Rossier, M.; Waelle, M.; Athanassiou, E. K.; Limbach, L. K.; Grass, R. N.; Günther, D.; Stark, W. J. Magnetic EDTA: Coupling Heavy Metal Chelators to Metal Nanomagnets for Rapid Removal of Cadmium, Lead and Copper from Contaminated Water. *Chem. Commun.* **2009**, 4862–4864.

(18) Järup, L. Hazards of Heavy Metal Contamination. *British Medical Bulletin*. December 1, 2003, pp 167–182.

(19) Tchounwou, P. B.; Yedjou, C. G.; Patlolla, A. K.; Sutton, D. J. Heavy Metals Toxicity and the Environment. *Mol. Clin. Environ. Toxicol.* **2012**, *101*, 133–164.

(20) European Environmental Agency. Contaminants affecting soil and groundwater in Europe — European Environment Agency https://www.eea.europa.eu/data-and-maps/daviz/overview-of-contaminants-affecting-soil#tab-chart_1 (accessed Jan 17, 2018).

(21) Mishra, A.; Shukla, S. K. Heavy Metal Toxicity: A Blind Evil. *J. Forensic Res.* **2014**, *5* (2).

(22) Jaishankar, M.; Tseten, T.; Anbalagan, N.; Mathew, B. B.; Beeregowda, K. N. Toxicity, Mechanism and Health Effects of Some Heavy Metals. *Interdiscip. Toxicol.* **2014**, *7* (2), 60–72.

(23) Goyer, R. A.; Clarkson, T. W. Toxic Effects of Metals. In *Casarett and Doull's Toxicology: The Basic Science of Poisons*.; Klaasen, C. D., Ed.; McGraw-Hill: New York, 2001; pp 811–867.

(24) Lambert, M.; Leven, B.; Green, R. New Methods of Cleaning Up Heavy Metal in Soils and Water: Innovative solutions to an environmental problem https://cfpub.epa.gov/ncer_abstracts/index.cfm/fuseaction/display.files/fileID/14295 (accessed May 21, 2018).

(25) Nriagu, J. O. A History of Global Metal Pollution. *Science.* **1996**, *272*, 223–224.

(26) Pizarro, F.; Olivares, M.; Gidi, V.; Araya, M. The Gastrointestinal Tract and Acute Effects of Copper in Drinking Water and Beverages. *Rev. Environ. Health* **1999**, *14* (4), 231–238.

(27) ASTDR. Toxicological Profile for Copper. *U.S Public Heal. Serv. Agency Toxic Subst. Dis. Regist.* **2004**, September, 121–189.

(28) Bulcke, F.; Dringen, R.; Scheiber, I. F. Neurotoxicity of Copper. In *Advances in Neurobiology*;

Aschner, Michael ; Costa, L. G., Ed.; Springer, 2017; Vol. 18, pp 313–343.

(29) National Research Council (US) Committe on Copper in Drinking Water. Health Effects of Excess Copper. In *Copper in Drinking Water*; National Academies Press: Washington, D.C., 2000; pp 78–113.

(30) World Health Organization (WHO). International lead poisoning prevention week of action http://www.who.int/phe/news/lead-poisoning-week/en/ (accessed Jan 18, 2018).

(31) U.S. Department of Health and Human Services.; Public Health Service.; Agency for Toxic Substances and Disease Registry. Toxicological Profile For Lead. https://www.atsdr.cdc.gov/toxprofiles/tp13.pdf (accessed Jan 18, 2018).

(32) Canfield, R. L.; Henderson, C. R.; Cory-Slechta, D. A.; Cox, C.; Jusko, T.; Lanphear, P. Intellectual Impairment in Children with Blood Lead Concentrations below 10 Microgram per Deciliter. **2003**, *348* (16), 1517–1526.

(33) Taylor, M.; Winder, C.; Lanphear, B. Eliminating Childhood Lead Toxicity in Australia: A Little Is Still Too Much. *Med. J. Aust.* **2012**, *197* (9), 493.

(34) Low Level Lead Exposure Harms Children: A Renewed Call for Primary Prevention. **2012**.

(35) Pinson, J.; Podvorica, F. Attachment of Organic Layers to Conductive or Semiconductive Surfaces by Reduction of Diazonium Salts. *Chem. Soc. Rev.* **2005**, *34* (5), 429–439.

(36) Pinson, J. Attachment of Organic Layers to Materials Surfaces by Reduction of Diazonium Salts, in Aryl Diazonium Salts: New Coupling Agents in Polymer and Surface Science. In *Aryl Diazonium Salts: New Coupling Agents in Polymer and Surface Science*; Chehimi, M. M., Ed.; WILEY-VCH Verlag GmbH: Paris, 2012; pp 1–27.

(37) Chow, E.; Gooding, J. J. Peptide Modified Electrodes as Electrochemical Metal Ion Sensors. *Electroanalysis* **2006**, *18* (15), 1437–1448.

(38) Jasmin, J. P.; Cannizzo, C.; Dumas, E.; Chaussé, A. Fabrication and Characterization of All-Covalent Nanocomposite Functionalized Screen-Printed Voltammetric Sensors. *Electrochim. Acta* **2014**, *133*, 467–474.

(39) Lo, M.; Diaw, A. K. D.; Gningue-Sall, D.; Aaron, J. J.; Oturan, M. A.; Chehimi, M. M. The Role of Diazonium Interface Chemistry in the Design of High Performance Polypyrrole-Coated Flexible ITO Sensing Electrodes. *Electrochem. commun.* **2017**, *77* (2016), 14–18.

(40) Mahouche Chergui, S.; Abbas, N.; Matrab, T.; Turmine, M.; Bon Nguyen, E.; Losno, R.; Pinson, J.; Chehimi, M. M. Uptake of Copper Ions by Carbon Fiber/Polymer Hybrids Prepared by Tandem Diazonium Salt Chemistry and In Situ Atom Transfer Radical Polymerization. *Carbon N. Y.* **2010**, *48* (7), 2106–2111.

(41) Baranton, S.; Bélanger, D. In Situ Generation of Diazonium Cations in Organic Electrolyte for

Electrochemical Modification of Electrode Surface. *Electrochim. Acta* **2008**, *53* (23), 6961–6967.

(42) Laurentius, L.; Stoyanov, S. R.; Gusarov, S.; Kovalenko, A.; Du, R.; Lopinski, G. P.; McDermott, M. T. Diazonium-Derived Aryl Films on Gold Nanoparticles: Evidence for a Carbon-Gold Covalent Bond. *ACS Nano* **2011**, *5* (5), 4219–4227.

(43) Vogel, A. I.; Tatchell, A. R.; Furnis, B. S.; Hannaford, A. J.; Smith, P. W. G. *Vogel's Textbook of Practical Organic Chemistry*, 5th ed.; Pearson Education Limited: England, 1989.

(44) Kong, J.; Frankilin, N.R.; Zhou, C.; Chapline, M.G.; Peng, S.; Cho, K.; Dai, H. Nanotube Molecular Wires as Chemical Sensors. *Science.* **2000**, *287* (5453), 622–625.

(45) Verpoorte, E. Microfluidic Chips for Clinical and Forensic Analysis. *Electrophoresis* **2002**, *23* (5), 677–712.

(46) Laurell, T.; Drott, J.; Rosengren, L. Silicon Wafer Integrated Enzyme Reactors. *Biosens. Bioelectron.* **1995**, *10* (3–4), 289–299.

(47) Yakimova, R.; Petoral, R. M.; Yazdi, G. R.; Vahlberg, C.; Lloyd Spetz, A.; Uvdal, K. Surface Functionalization and Biomedical Applications Based on SiC. *J. Phys. D. Appl. Phys.* **2007**, *40* (20), 6435–6442.

(48) Chen, K. I.; Li, B. R.; Chen, Y. T. Silicon Nanowire Field-Effect Transistor-Based Biosensors for Biomedical Diagnosis and Cellular Recording Investigation. *Nano Today* **2011**, *6* (2), 131–154.

(49) Cui, Y.; Wei, Q.; Park, H.; Lieber, C. M. Nanowire Nanosensors for Highly Sensitive and Selective Detection of Biological and Chemical Species. *Science.* **2001**, *293* (5533), 1289–1292.

(50) Filler, M. A.; Bent, S. F. The Surface as Molecular Reagent: Organic Chemistry at the Semiconductor Interface. *Progress in Surface Science*. Pergamon September 1, 2003, pp 1–56.

(51) Blackburn, G. F. Fundamentals and Applications. In *Biosensors*; Turner, A.F.P.; Karube, I.; Wilson, G. S., Ed.; Oxford Univ. Press, Oxford, 1987; pp 481–530.

(52) Dugas, V; Elaissari, A; Chevalier, Y. Surface Sensitization Techniques and Recognition Receptors Immobilization on Biosensors and Microarrays. In *Recognition Receptors in Biosensors*; Zourob, M., Ed.; Springer New York: New York, NY, 2010; pp 47–132.

(53) Bent, S. F. Organic Functionalization of Group IV Semiconductor Surfaces: Principles, Examples, Applications, and Prospects. *Surf. Sci.* **2002**, *500* (1–3), 879–903.

(54) Yáñez-Sedeño, P.; Agüí, L.; Villalonga, R.; Pingarrón, J. M. Biosensors in Forensic Analysis. A Review. *Anal. Chim. Acta* **2014**, *823*, 1–19.

(55) Allongue, P.; Henry de Villeneuve, C.; Cherouvrier, G.; Cortès, R.; Bernard, M.-C. Phenyl Layers on H–Si(111) by Electrochemical Reduction of Diazonium Salts: Monolayer versus Multilayer Formation. *J. Electroanal. Chem.* **2003**, *550–551*, 161–174.

(56) Buriak, J. M. Organometallic Chemistry on Silicon and Germanium Surfaces. *Chem. Rev.* **2002**, *102* (5), 1271–1308.

(57) Stewart, M. P.; Maya, F.; Kosynkin, D. V; Dirk, S. M.; Stapleton, J. J.; McGuiness, C. L.; Allara, D. L.; Tour, J. M. Direct Covalent Grafting of Conjugated Molecules onto Si, GaAs, and Pd Surfaces from Aryidiazonium Salts. *J. Am. Chem. Soc.* **2004**, *126* (1), 370–378.

(58) Bélanger, D.; Pinson, J. Electrografting: A Powerful Method for Surface Modification. *Chem. Soc. Rev.* **2011**, *40* (7), 3995–4048.

(59) Boukherroub, R. Chemical Reactivity of Hydrogen-Terminated Crystalline Silicon Surfaces. *Curr. Opin. Solid State Mater. Sci.* **2005**, *9* (1–2), 66–72.

(60) Bent, S. F. Organic Functionalization of Group IV Semiconductor Surfaces: Principles, Examples, Applications, and Prospects. *Surf. Sci.* **2002**, *500* (1–3), 879–903.

(61) Ubara, H.; Imura, T.; Hiraki, A. Formation of Si-H Bonds on the Surface of Microcrystalline Silicon Covered with SiOx by HF Treatment. *Solid State Commun.* **1984**, *50* (7), 673–675.

(62) Higashi, G. S.; Chabal, Y. J.; Trucks, G. W.; Raghavachari, K. Ideal Hydrogen Termination of the Si (111) Surface. *Appl. Phys. Lett.* **1990**, *56* (7), 656–658.

(63) Zazzera, L.; Evans, J. F. In Situ Internal Reflection Infrared Study of Aqueous Hydrofluoric Acid and Ultraviolet/Ozone Treated Silicon (100) Surfaces. *J. Vac. Sci. Technol. A Vacuum, Surfaces, Film.* **1993**, *11* (4), 934.

(64) Michalak, D. J.; Amy, S. R.; Aureau, D.; Dai, M.; Estève, A.; Chabal, Y. J. Nanopatterning Si(111) Surfaces as a Selective Surface-Chemistry Route. *Nat. Mater.* **2010**, *9* (3), 266–271.

(65) Elgrishi, N.; Rountree, K. J.; McCarthy, B. D.; Rountree, E. S.; Eisenhart, T. T.; Dempsey, J. L. A Practical Beginner's Guide to Cyclic Voltammetry. *J. Chem. Educ.* **2018**, *95* (2), 197–206.

(66) Atobe, M. Fundamental Principles of Organic Electrochemistry: Fundamental Aspects of Electrochemistry Dealing with Organic Molecules. In *Fundamentals and Applications of Organic Electrochemistry*; Fuchigami, Toshio Atobe, M. I. S., Ed.; John Wiley & Sons Ltd: United Kingdom, 2015; pp 1–10.

(67) Bard, Allen J Faulkner, L. R. *Electrochemical Methods Fundamentals and Applications*, 2nd ed.; Bard, Allen J Faulkner, L. R., Ed.; John Wiley & Sons Ltd: New York, NY, 2001.

(68) Compton, R. G.; Sanders, G. H. W. Electrode Potentials. **1996**, 21.

(69) Stoeckel, Wolfgang; Schumacher, R. In Situ Microweighing at the Junction Metal/Electrolyte.

Phys. Chem. **1987**, *91*, 345–349.

(70) Sauerbrey, G. Verwendung von Schwingquarzen Zur Wügung Dnner Schichten Und Zur Mikrowügung. *Zeitschrift für Phys.* **1959**, *155* (2), 206–222.

(71) Bard, Allen J Faulkner, L. R. Electrochemical Methods Fundamentals and Applications; Bard, Allen J Faulkner, L. R., Ed.; John Wiley & Sons, Inc: New York, NY, 2001; p 725–728; Chapter 17.

(72) Laforgue, A.; Addou, T.; Bélanger, D. Characterization of the Deposition of Organic Molecules at the Surface of Gold by the Electrochemical Reduction of Aryldiazonium Cations. *Langmuir* **2005**, *21* (15), 6855–6865.

(73) Muratsugu, M.; Ohta, F.; Miya, Y.; Hosokawa, T.; Kurosawa, S.; Kamo, N.; Ikeda, H. Quartz Crystal Microbalance for the Detection of Microgram Quantities of Human Serum Albumin: Relationship between the Frequency Change and the Mass of Protein Adsorbed. *Anal. Chem.* **1993**, *65* (20), 2933–2937.

(74) Shimazu, K.; Yagi, I.; Sato, Y.; Uosaki, K. In Situ and Dynamic Monitoring of the Self-Assembling and Redox Processes of a Ferrocenylundecanethiol Monolayer by Electrochemical Quartz Crystal Microbalance. *Langmuir* **1992**, *8* (5), 1385–1387.

(75) Zhang, X.; Rösicke, F.; Syritski, V.; Sun, G.; Reut, J.; Hinrichs, K.; Janietz, S.; Rappich, J. Influence of the Para-Substitutent of Benzene Diazonium Salts and the Solvent on the Film Growth during Electrochemical Reduction. *Zeitschrift fur Phys. Chemie* **2014**, *228* (4–5), 557–573.

(76) Hinrichs, K.; Gensch, M.; Esser, N. Analysis of Organic Films and Interfacial Layers by Infrared Spectroscopic Ellipsometry. *Appl. Spectrosc.* **2005**, *59* (11), 272A--282A.

(77) Fujiwara, H. *Spectroscopic Ellipsometry: Principles and Applications*; 2007.

(78) Rappich, J.; Hinrichs, K. In Situ Study of Nitrobenzene Grafting on Si(111)-H Surfaces by Infrared Spectroscopic Ellipsometry. *Electrochem. commun.* **2009**, *11* (12), 2316–2319.

(79) Watts, J. F.; Wolstenholme, J. Electron Spectroscopy: Some Basic Concepts. In *An Introduction to Surface Analysis by XPS and AES*; John Wiley & Sons, Ltd: Chichester, UK, 2003.

(80) Jacobs, K. Photoelectron spectrometer, ESCALAB Mk II by Vacuum Generators https://jacobs.physik.uni-saarland.de/home/index.php?page=forschung/UHV-Lab-1 (accessed Jul 22, 2018).

(81) Smart, R.; Mcintyre, S.; Bello, I. X - ray Photoelectron Spectroscopy. mmrc.caltech.edu/SS_XPS/ XPS_PPT/XPS_Slides.pdf.

(82) Seah, M. P.; Dench, W. A. Quantitative Electron Spectroscopy of Surfaces : *Surf. Interface*

Anal. **1979**, *1* (1), 2–11.

(83) A. V. Naumkin; Kraut-Vass, A.; Gaarenstroom, S. W.; Powell, C. J. NIST X-ray Photoelectron Spectroscopy Database, Version 4.1 https://srdata.nist.gov/xps/ (accessed Jun 15, 2018).

(84) Larkin, P. J. *IR and Raman Spectroscopy - Principles and Spectral Interpretation*, 1st ed.; Larkin, P. J., Ed.; Elsevier: Netherlands, 2011.

(85) Suffren, Y.; Rollet, F.-G.; Reber, C. Raman Spectroscopy of Transition Metal Complexes: Molecular Vibrational Frequencies, Phase Transitions, Isomers, and Electronic Structures. *Comments Inorg. Chem.* **2011**, *32* (5–6), 246–276.

(86) Tian, R.; Seitz, O.; Li, M.; Hu, W.; Chabal, Y. J.; Gao, J. Infrared Characterization of Interfacial Si-O Bond Formation on Silanized Flat SiO2/Si Surfaces. *Langmuir* **2010**, *26* (7), 4563–4566.

(87) Karakassides, M. A, Gournis, D, Petridis, D. An Infrared Reflectance Study of Si-O Vibrations in Thermally Treated Alkali-Saturated Montmorillonites. *Clay Miner.* **1999**, *34*, 429–438.

(88) Piranha Solutions - Safety Library | Division of Research Safety - Illinois https://www.drs.illinois.edu/SafetyLibrary/PiranhaSolutions (accessed Jul 12, 2018).

(89) Miller, A. L. Dimercaptosuccinic Acid (DMSA), a Non-Toxic, Water-Soluble Treatment for Heavy Metal Toxicity. *Altern. Med. Rev.* **1998**, *3* (3), 199–207.

(90) de Villeneuve, C. H.; Pinson, J.; Bernard, M. C.; Allongue, P. Electrochemical Formation of Close-Packed Phenyl Layers on Si(111). *J. Phys. Chem. B* **1997**, *101* (14), 2415–2420.

(91) Angelova, P.; Solel, E.; Parvari, G.; Turchanin, A.; Botoshansky, M.; Gölzhäuser, A.; Keinan, E. Chemisorbed Monolayers of Corannulene Penta-Thioethers on Gold. *Langmuir* **2013**, *29*, 2217–2223.

(92) Feineis, S.; Lutz, J.; Heffele, L.; Endl, E.; Albrecht, K.; Groll, J. Thioether – Polyglycidol as Multivalent and Multifunctional Coating System for Gold Nanoparticles. *Adv. Mater.* **2018**, *30* (8), 1–6.

(93) Mettela, G.; Kulkarni, G. U. Facet Selective Etching of Au Microcrystallites. *Nano Res.* **2015**, *8* (9), 2925–2934.

(94) Chemistry Department Purdue Univ. Rate Laws from Graphs of Concentration Versus Time (Integrated Rate Laws) https://www.chem.purdue.edu/gchelp/howtosolveit/Kinetics/IntegratedRateLaws.html (accessed May 10, 2018).

(95) Wright, M. R. The Kinetic Analysis of Experimental Data. In *An Introduction to Chemical Kinetics*; Wright, M. R., Ed.; John Wiley & Sons Ltd, 2004; pp 43–84.

(96) Oger, N.; Grognec, E. Le; d'Halluin, M.; Felpin, F.-X. Using Aryl Diazonium Salts in Palladium-

Catalyzed Reactions under Safer Conditions. *Org. Process Res. Dev.* **2014**, *18*, 1786–1801.

(97) Vallance, C. Rate Laws: Relating the Reaction Rates to Reactant Concentrations. In *An Introduction to Chemical Kinetics*; Vallance, C., Ed.; IOP Publishing, 2017; pp 21–26.

(98) Papanastasiou, G.; Kokkinidis, G.; Papadopoulos, N. Determination of Kinetic Parameters from Chronoamperometric Data. *Electroanal. Chem.* **1993**, *352*, 153–165.

(99) Belding, S. R.; Rogers, E. I.; Compton, R. G. Potential Step Chronoamperometry at Microdisc Electrodes : Effect of Finite Electrode Kinetics. *J. Phys. Chem.* **2009**, *113*, 4202–4207.

(100) Ryan, M. C.; Wei, J.-F.; Feinberg, B. A.; Lau, Y.-K. The Chronoamperometric Determination of Homogeneous Small Molecule-Redox Protein Reaction Rates. *Anal. Biochem.* **1979**, *96*, 326–333.

(101) Jarzęcki, A. A. Quantum-Mechanical Study of Lead Coordination in Sulfur-Rich Proteins: Mode and Structure Recognition in UV Resonance Raman Spectra. *J. Phys. Chem. A* **2012**, *116* (1), 571–581.

(102) Siiman, O.; Young, N. M.; Carey, P. R. Resonance Raman Spectra of “Blue” Copper Proteins and the Nature of Their Copper Sites. *J. Am. Chem. Soc.* **1976**, *98* (3), 744–748.

(103) Thamann, T. J.; Frank, P.; Willis, L. J.; Loehr, T. M. Normal Coordinate Analysis of the Copper Center of Azurin and the Assignment of Its Resonance Raman Spectrum. *Proc. Natl. Acad. Sci.* **1982**, *79* (October), 6396–6400.

(104) Andrew, C. R.; Yeom, H.; Valentine, J. S.; Karlsson, B. G.; van Pouderoyen, G.; Canters, G. W.; Loehr, T. M.; Sanders-Loehr, J.; Bonander, N. Raman Spectroscopy as an Indicator of Cu-S Bond Length in Type 1 and Type 2 Copper Cysteinate Proteins. *J. Am. Chem. Soc.* **1994**, *116* (25), 11489–11498.

(105) Ferraro, J. R.; Walker, W. R. Infrared Spectra of Hydroxy-Bridged Copper(II) Compounds. *Inorg. Chem.* **1965**, *4* (10), 1382–1386.

(106) Hadjiev, V. G Cardona, M Thomsen, C Kircher, J. Raman Scattering Probe of Oxygen Ordering During Room-Temperature Annealing of YBa2Cu3O7-δ. *Phys. Rev. B* **1993**, *47* (14), 9148–9150.

(107) Morozov, V. Vibrational Spectra of Glasses of the PbO-GeO2 System. *J. Appl. Spectrosc.* **1968**, *8* (5), 501–503.

(108) Ahsan, M. R.; Uddin, M. A.; Mortuza, M. G. Infrared Study of the Effect of P2O5 in the Structure of Lead Silicate Glasses. *Indian J. pure Appl. Phys.* **2005**, *43* (February), 89–99.

(109) Harris, C. M.; Livingstone, S. E. Bidentate Chelates. In *Chelating Agents and Metal Chelates*; Elsevier, 1964; pp 95–141.

(110) Sisombath, N. S.; Jalilehvand, F.; Schell, A. C.; Wu, Q. Lead(II) Binding to the Chelating Agent D-Penicillamine in Aqueous Solution. *Inorg. Chem.* **2014**, *53*, 12459–12468.

(111) Surface Science Western Lab. X-ray Photoelectron Spectroscopy (XPS) Reference Pages: Cu(0):Cu(II) or Cu(I):Cu(II) Calculations http://www.xpsfitting.com/2012/01/cu0cuii-or-cuicuii-calculations.html (accessed Apr 30, 2018).

(112) Fujiwara, M.; Matsushita, T.; Ikeda, S. X-Ray Photoelectron Spectroscopy of Copper(II) Complexes with Donor Sets of O4, N2O4, N2O2, N4, N2S2, and S4. *Anal. Sci.* **1993**, *9* (2), 289–291.

(113) Kavitha, C.; Babu, M. S.; Saraswathi, K. Spectrophotometric Determination of Copper as Copper Piperazine. *Int. Lett. Chem. Phys. Astron.* **2013**, *8* (3), 205–209.

(114) eBiochemicals. Piperazine IR 110-85-0 1,4-Diazacyclohexane; piperazine eBiochemicals http://www.ebiochemicals.com/Wiki/QcEB000031170_IR_4.html (accessed May 7, 2018).

(115) Costisor, O; Tudose, R; Pantenburg, I; Meyer, G. A New Copper(II) Complex with the N,N'-Bis(Antipyryl-4-Methyl)-Piperazine (BAMP) Ligand: $[Cu(BAMP)](ClO_4)_2$. *Zeitschrift fiir Naturforsch.* **2002**, *57* (b), 1454–1460.

(116) Silverstein, R. M. Webster, F. X. Kiemle, D. J. Infrared Spectrometry; C-N Stretching Vibrations. In *Spectrometric Identifcation of Organic Compounds*; Debbie, E. Yee, J. Kennedy, P. Wolfman-Robichaud, S. Wygal, A. Lesure, M. Rigby, S., Ed.; John Wiley & Sons, Inc: New York, NY, 2005; p 102.

(117) Loskill, P.; Hähl, H.; Faidt, T.; Grandthyll, S.; Müller, F.; Jacobs, K. Is Adhesion Superficial? Silicon Wafers as a Model System to Study van Der Waals Interactions. *Adv. Colloid Interface Sci.* **2012**, *179–182*, 107–113.

(118) National Institute of Standards and Technology (NIST). NIST XPS Database Detail Page: Element Cu: 2p3/2 Line Designation https://srdata.nist.gov/xps/XPSDetailPage.aspx?AllDataNo=27179 (accessed Jun 3, 2018).

Publications and Conferences

[1] Paper: Adongo, J.O.*; Neubert, T.J.; Sun, G.; Janietz, S.; Lauermann, I.; Rademann, K.; Rappich, J. “Fabrication and Characterization of Surfaces Modified with Carboxymethylthio Ligands for Chelate-Assisted Trapping of Copper” *ACS Applied Materials & Interfaces 9(28): pp. 24273–24281. June 2017*.

[2] Poster Presentation: Adongo, J.O.*; Neubert, T.J.; Sun, G.; Janietz, S.; Lauermann, I.; Rademann, K.; Rappich, J. Fabrication and Characterization of Surfaces Modified with Carboxymethylthio Ligands for Chelate-Assisted Trapping of Copper. At the *BASF Science Breakfast Meeting: Presentation Workshop for “Circular Economy”; 67th. Lindau Nobel Laureate Meeting, Lindau, Germany: 28th – 30th. June 2017.*

[3] Poster Presentation: Adongo, J.O.*; Neubert, T.J.; Sun, G.; Janietz, S.; Lauermann, I.; Rademann, K.; Rappich, J. “Towards a Renewable Modified Surface for Rapid Sensing and Chelation of Heavy Metal Pollutants”. *International Conference on the Formation of Semiconductor Interfaces. Hannover, Germany: 2nd – 7th July 2017.*

[4] Oral Presentation: Adongo, J.O.*; Neubert, T.J.; Sun, G.; Janietz, S.; Lauermann, I.; Rademann, K.; Rappich, J. “Fabrication and Characterization of Surfaces Modified with Carboxymethylthio Ligands for Chelate-Assisted Trapping of Copper”. *14th International Conference and Exhibition on Materials Science and Engineering; Las Vegas, USA, 13th – 15th Nov. 2017.*

Acknowledgements

I wish to profoundly thank Prof. Dr. Klaus Rademann of Humboldt Universität zu Berlin (Institut für Chemie) for accepting to supervise and review my doctoral work. My sincere gratitude, deep admiration and respect also go to Dr. Jörg Rappich, a strong mentor and a constructive critic, who introduced me into the exciting world of organic functionalization of silicon and gold surfaces via electrochemical methods in his laboratory (Institut für Silizium-Photovoltaik – HZB) - Germany. My sincere gratitude also goes to Prof. Dr. Nickel Norbert for allowing me to use the Raman laboratory (Institut für Silizium-Photovoltaik – HZB) - Germany. I also wish to thank PD. Dr. Sylvia Janietz of Fraunhofer-Institut für Angewandte Polymerforschung (IAP), Potsdam-Golm Germany, for preparing the diazonium salt compounds that were investigated in this work. I am sincerely grateful to PD Dr. Karsten Hinrichs, Prof. Dr. Nicola Pinna and Prof. Dr. Kannan Balasubramanian for accepting to review my work. I also thank Dr. Guoguang Sun for his valuable support in terms of facilitating IRSE analytical measurements at Leibnitz-Institut für Analytische Wissenschaften-ISAS-e.V. Berlin Germany. I also dearly thank Dr. Iver Lauermann of PVcomB - HZB, Berlin Germany, for help with the XPS measurements and analysis in this work. I also wish to acknowledge support from the members of the HZB fraternity and the surface science / electrochemistry research group at the Institut für Silizium-Photovoltaik (HZB). I wish to also thank Dr. Felix Rösicke and Tilmann J. Neubert for their guidance and support in certain aspects of my work.

I wish to acknowledge the Deutscher Akademischer Austauchdienst (DAAD) - Germany in collaboration with the National Research Fund (NRF) - Kenya, under the joint Kenyan-German postgraduate scholarship program for the financial grant in terms of stipend allowances during the duration of my studies here in Germany.

Finally, I wish convey my utmost gratitude to my dear wife Cynthia for her constant encouragement and immense support throughout my doctoral studies here in Berlin Germany.

Declaration of Independent Work

I declare that I have completed the thesis independently using only the aids and tools specified. I have not applied for a doctor's degree in the doctoral subject elsewhere and do not hold a corresponding doctor's degree. I have taken due note of the Faculty of Mathematics and Natural Sciences PhD Regulations, published in the Official Gazette of Humboldt-Universität zu Berlin no. 126/2014 on 18/11/2014.

_____	_____	_____
Date	Place	Signature